A Superconducting RF Deflecting Cavity for the ARIEL e-Linac Separator

by

Douglas W. Storey
Bachelor of Science, University of Winnipeg, 2007
Bachelor of Aerospace Engineering and Mechanics, University of Minnesota, 2009
Master of Science, University of Victoria, 2011

A Dissertation Submitted in Partial Fulfillment of the
Requirements for the Degree of

DOCTOR OF PHILOSOPHY

in the Department of Physics and Astronomy

A Superconducting RF Deflecting Cavity for the ARIEL e-Linac Separator

by

Douglas W. Storey
Bachelor of Science, University of Winnipeg, 2007
Bachelor of Aerospace Engineering and Mechanics, University of Minnesota, 2009
Master of Science, University of Victoria, 2011

Supervisory Committee

---

Dr. D. Karlen, Co-Supervisor
(University of Victoria)

---

Dr. L. Merminga, Co-Supervisor
(University of Victoria)

---

Dr. R. E. Laxdal, Committee Member
(University of Victoria)

---

Dr. J. Bornemann, Outside Member
(University of Victoria)

## ABSTRACT

The ARIEL electron linac is a 0.3 MW accelerator that will drive the production of rare isotopes in TRIUMF's new ARIEL facility. A planned upgrade will allow a second beam to be accelerated in the linac simultaneously, driving a Free Electron Laser while operating as an energy recovery linac. To not disrupt beam delivery to the ARIEL facility, an RF beam separator is required to separate the interleaved beams after they exit the accelerating cavities. A 650 MHz superconducting RF deflecting mode cavity has been designed, built, and tested for providing the required 0.3 MV transverse deflecting voltage to separate the interleaved beams. The cavity operates in a TE-like mode, and has been optimized through the use of simulation tools for high shunt impedance with minimal longitudinal footprint.

The design process and details about the resulting electromagnetic and mechanical design are presented, covering the cavity's RF performance, coupling to the operating and higher order modes, multipacting susceptibility, and the physical design. The low power dissipation on the cavity walls at the required deflecting field allows for the cavity to be fabricated using non-conventional techniques. These include fabricating from bulk, low purity niobium and the use of TIG welding for joining the cavity parts. A method for TIG welding niobium is developed that achieves minimal degradation in purity of the weld joint while using widely available fabrication equipment. Applying these methods to the fabrication of the separator cavity makes this the first SRF cavity to be built at TRIUMF.

The results of cryogenic RF tests of the separator cavity at temperatures down to 2 K are presented. At the operating temperature of 4.2 K, the cavity achieves a quality factor of $4 \times 10^8$ at the design deflecting voltage of 0.3 MV. A maximum deflecting voltage of 0.82 MV is reached at 4.2 K, with peak surface fields of 26 MV/m and 33 mT. The cavity's performance exceeds the goal deflecting voltage and quality factor required for operation.

# Contents

# List of Tables

# List of Figures

# List of Abbreviations

| | |
|---|---|
| 4RCC | 4-Rod Crab Cavity. 47 |
| AC | Alternating Current. |
| ARIEL | Advanced Rare IsotopE Laboratory. 1, 6 |
| BBU | Beam Break-Up. 37 |
| BCP | Buffered Chemical Polish. 118 |
| BCS | Bardeen, Cooper, and Schrieffer. 22 |
| BNL | Brookhaven National Laboratory. 42 |
| CEBAF | Continuous Electron Beam Accelerator Facility. 45 |
| CERN | European Council for Nuclear Research (French: Conseil Européen pour la Recherche Nucléaire). 28 |
| CW | Continuous Wave. 6 |
| DC | Direct Current. |
| DQW | Double Quarter Wave. 47 |
| DTL | Drift Tube Linac. 5, 15 |
| e-Linac | Electron Linear Accelerator. 1, 6 |
| EBW | Electron Beam Weld. 101 |
| EDM | Electric Discharge Machining. 93 |
| EP | Electropolish. 123 |
| eRHIC | Electron-Ion Collider integrated with RHIC (Relativistic Heavy Ion Collider). 74 |
| ERL | Energy Recovery Linac. 8 |

FEL Free Electron Laser. 9
FEM Finite Element Method. 15

HL-LCH High Luminosity Large Hadron Collider. 46
HOM Higher Order Mode. 13, 36
HPWR High Pressure Water Rinse. 123
HWR Half Wave Resonator. 15

ISAC Isotope Separator and Accelerator. 5
ISOL Isotope Separation On-Line. 5

KEK High Energy Accelerator Research Organization (Japan). 43

LCLS Linac Coherent Light Source. 42
LEP Large ElectronPositron Collider. 74
LLRF Low Level RF. 131
LOM Lower Order Mode. 13

NERSC National Energy Research Scientific Computing Center. 54
NSCL National Superconducting Cyclotron Laboratory. 101
NWA Network Analyser. 95

QWR Quarter Wave Resonator. 6, 15

RF Radio Frequency.
RFD RF Dipole. 47
RFQ Radiofrequency Quadrupole. 5, 15
RIB Rare (or Radioactive) Isotope Beam. 5
RLA Recirculating Linear Accelerator. 8
RMS Root Mean Square. 12
RRR Residual Resistivity Ratio. 25

SEY Secondary Emission Yield. 81
SLAC Previously the Stanford Linear Accelerator Center. 42
SPS Super Proton Synchrotron. 49

| | |
|---|---|
| SRF | Superconducting Radiofrequency. |
| SWR | Standing Wave Ratio. 136 |
| TE | Transverse Electric. 14 |
| TEM | Transverse Electric and Magnetic. 14 |
| TESLA | Tera-electron volt Energy Superconducting Linear Accelerator. 7 |
| TIG | Tungsten Inert Gas Welding. Also, GTAW – Gas Tungsten Arc Welding. 101 |
| TM | Transverse Magnetic. 14 |

.

# List of Symbols

| | |
|---|---|
| $Att$ | Attenuation of an RF cable. 133 |
| $A$ | Fitting parameter for the RF surface resistance within BCS theory. 140 |
| $B_p$ | Peak surface magnetic field. 55 |
| $B$ | Magnetic field. 14 |
| $E_\perp$ | Transverse deflecting field. 17 |
| $E_p$ | Peak surface electric field. 55 |
| $E$ | Electric field. 14 |
| $G$ | Geometry factor. 18 |
| $H_c$ | Critical magnetic field of a Type I superconductor. 21 |
| $H_{c1}$ | Lower critical magnetic field of a Type II superconductor. 22 |
| $H_{c2}$ | Upper critical magnetic field of a Type II superconductor. 22 |
| $H$ | Magnetic field strength. 14 |
| $I_0$ | Beam current. 31 |
| $I_{th}$ | Threshold current for multipass beam breakup. 37 |
| $J_m$ | Bessel function of the first kind in the m-th order. 14 |
| $P_c$ | Power dissipated on walls of an RF cavity. 18, 29, 134 |
| $P_f$ | Forward power. 131 |
| $P_g$ | Generator (or forward) power. 29, 34, 65 |
| $P_r$ | Reflected power. 29, 131 |
| $P_{ext}$ | Power loss through an external source such as the input coupler. 18 |
| $P_{pu}$ | Pick up (or transmitted) power. 131 |
| $Q_0$ | Quality factor of an RF cavity. 18, 136 |
| $Q_{0+pu}$ | Quality factor of the cavity plus pick up. 135 |
| $Q_L$ | Loaded quality factor. 18, 134 |

| | |
|---|---|
| $Q_{ext}$ | External quality factor due to a power loss to an external source such as the input coupler. 18 |
| $Q_{pu}$ | Quality factor of the pick up. 80, 134 |
| $RRR$ | Residual Resistivity Ratio. 25, 27, 105 |
| $R_\perp/Q$ | Transverse geometric shunt impedance. 19, 36 |
| $R_\perp$ | Transverse shunt impedance. 19 |
| $R_s$ | RF surface resistance. 18, 25, 140 |
| $R_{BCS}$ | BCS surface resistance. 23 |
| $R_{acc}/Q$ | Longitudinal geometric shunt impedance. 36 |
| $R_{res}$ | Residual surface resistance. 24, 140 |
| $SWR$ | Standing Wave Ratio. 136 |
| $S_{11}$ | Reflected power ratio from port 1. 133 |
| $S_{21}$ | Power ratio received at port 2 from port 1. 133 |
| $T_b$ | Spacing of bunches making up a particle beam. 31 |
| $T_c$ | Superconducting transition temperature. 21 |
| $T$ | Temperature. |
| $U$ | Energy stored within the electromagnetic fields in an RF cavity. 18 |
| $V_\perp$ | Transverse deflecting cavity voltage. 17, 135 |
| $V_{br}$ | Deflecting voltage induced in an RF cavity by a beam in resonance with the cavity. 31 |
| $V_b$ | Deflecting voltage induced by a beam in a detuned RF cavity. 32, 64 |
| $V_{gr}$ | Deflecting voltage induced in an RF cavity by a generator in resonance with the cavity. 29 |
| $V_g$ | Deflecting voltage induced by a generator in an RF cavity detuned from the drive frequency. 30 |
| $V$ | Cavity voltage. 17 |
| $\Delta\omega$ | 3 dB bandwidth. 19 |
| $\Delta p$ | Change in momentum. |
| $\Delta x$ | Offset of a bunch from the cavity axis. 31 |
| $\Delta$ | Energy gap for a superconductor within BCS theory. 23, 140 |
| $\Gamma$ | Reflection coefficient. 29 |
| $\Upsilon$ | Transverse growth parameter for beam break up. 37 |
| $\beta^*$ | Coupling factor of the combined effect of input coupler and pick up antenna. 135, 136 |

| | |
|---|---|
| $\beta_{pu}$ | Coupling factor of the pick up antenna. 134 |
| $\beta$ | The ratio of the velocity to the speed of light. 15 |
| $\beta$ | Coupling factor. 28 |
| $\delta$ | Skin depth. 20 |
| $\epsilon_0$ | Permittivity of free space, $8.8542 \times 10^{-12}\,\mathrm{F/m}$. |
| $\epsilon_n$ | Normalized emittance of a particle beam. 12, 61 |
| $\epsilon_r$ | Relative permittivity. 129 |
| $\eta$ | Impedance of free space, $376.730\,\Omega$. 14 |
| $\kappa$ | Thermal conductivity. 26 |
| $\lambda_L$ | London penetration depth. 22 |
| $\lambda$ | Wavelength. |
| $\mu_0$ | Permeability of free space, $4\pi \times 10^{-7}\,\mathrm{H/m}$. |
| $\mu_r$ | Relative permeability. 129 |
| $\omega$ | Angular frequency. |
| $\phi$ | Relative phase, with respect to the field within an RF cavity. 17 |
| $\psi$ | Detuning angle of an RF cavity. 30, 67 |
| $\rho$ | Electrical resistivity. |
| $\sigma$ | Electrical conductivity. |
| $\tau$ | Decay constant. 19, 31, 134 |
| $\tilde{V}_c$ | Deflecting voltage induced in an RF cavity, in phasor notation. 32, 64 |
| $\xi$ | Coherence length. 22 |
| $c$ | The speed of light, $299\,792\,458\,\mathrm{m/s}$. |
| $df/dp$ | Pressure sensitivity. 85 |
| $k_B$ | Boltzmann constant, $1.3806 \times 10^{23}\,\mathrm{J/K}$. 140 |
| $k$ | Angular wave number. |
| $q$ | Charge of a particle or bunch. |
| $v$ | Velocity. |

# ACKNOWLEDGEMENTS

I would like to extend my deep gratitude to Dean Karlen, Lia Merminga, and Bob Laxdal for their valuable supervision and guidance as I carried out this research. I have learnt much from each of you and am very grateful for the wisdom and experience you have passed on to me.

I would like to thank the entire SRF team at TRIUMF for sharing their knowledge and experience with me. I have received immense support and guidance from Tobias Junginger, Zhongyuan Yao, Yanyun Ma, and Liu Yang through my time at TRIUMF. I am lucky to have had the opportunity to study with fellow graduate students Philipp Kolb, Ramona Leewe, Edward Thoeng, and Zahra (Melika) Shahriari, as well as everyone else at TRIUMF that has made my time there enjoyable.

I am extremely thankful to Ben Matheson and Norman Muller for transforming my sketches and idealistic models into a real SRF cavity. James Keir, Devon Lang, and Thomas Au have provided support in many ways, from spending many hours suited up to perform BCP to providing advice, tools, and making last minute parts. Your contributions made it all come together. I am also grateful to Bhalwinder Waraich and Vladimir Zvyagintsev for sharing with me their valuable experience.

Bhalwinder also assisted (or perhaps I assisted him) in assembling the cavity for cryogenic testing. Cryogenic support for the RF tests was provided by David Kishi and Howard Liu, and Qiwen Zheng prepared the LLRF system. I am extremely thankful to Zhongyuan Yao for providing me with guidance in preparing for these tests and for staying late hours with me taking the measurements.

I am extremely grateful for all of the effort put in by the TRIUMF machine shop in support of this research and putting up with me showing up on the machine shop floor every day for the last two years. In particular, thank you to Neil Thiem for TIG welding countless niobium samples and taking on the challenge of welding this cavity, and Tim Goodsell for machining and polishing the cavity parts (twice!) and for developing all of the jigs that made the TIG welding possible. Thanks also to Mike Wicken and Bob Welbourn for their quick action in learning how to EBW niobium to titanium.

Thanks to Chris Compton from MSU for taking part in a review of the separator cavity design, and for sharing his knowledge and experience on TIG welding niobium. We also received an oxygen sensor on loan from Chris that really made this part of my thesis possible.

I am grateful for the support received from Bassam Hitti and the rest of the TRIUMF CMMS team for providing the cryostat, liquid helium, and their time to make the RRR measurements possible. The RRR measurement apparatus that was used was originally put together by David Longuevergne and further developed by Anna Grassellino and Syed Haider Abidi.

I would also like to recognize Yu-Chiu Chao and Chris Gong for determining the baseline requirements of the ARIEL separator. Thanks to the visiting students who have assisted me during their time at TRIUMF, in chronological order: Matthew Hill, Francois Renaud, Arthur Chen, and Walter Wasserman. I would also like to thank Jeremiah Holzbauer for including his ANSYS-APDL scripts as an appendix to his Doctorial thesis as this was immensely helpful in developing my own scripts.

My graduate studies were made possible in part by funding received through the NSERC Alexander Graham Bell CGS-Doctoral Program Award as well as by support from the University of Victoria. I am grateful to have had the opportunity to carry out this research at TRIUMF, which I have found to be an institution full of great opportunities for students. And finally, I would like to express my appreciation to the SRF community for selecting my presentation of this work for first prize in the poster competition at the International Conference on RF Superconductivity.

Finally, thank you to everyone else whom I have worked with, studied with, or been instructed by over the years that have helped me to reach this point in my career as a physicist.

# DEDICATION

To my family:

**My parents,** for raising me with a curious mind.

**My grandparents,** for all their support throughout this long endeavour.

**And to Carly,** for being by my side through it all.

# Chapter 1

# Introduction

Radiofrequency (RF) cavities are the foundation for many modern particle accelerators. They provide a means for accelerating particles to higher energy, manipulating transverse momentum, and can contribute to the diagnostics of beam properties. The uses of particle accelerators have expanded from mainly serving the basic sciences to their routine use in medical treatments and diagnostics, and an increasing role in industrial processes. The application of the phenomenon of superconductivity to RF cavities has greatly increased their efficiency, allowing RF cavities to operate continuously at high gradient, leading to accelerators with both high beam energy and current, and decreased operational costs.

TRIUMF operates a number of particle accelerators for studies of particle and nuclear physics, nuclear medicine, and materials science, as well as also performing research on the science of particle acceleration and the development of new particle accelerators. The main area of research at TRIUMF is the production and study of radioactive isotopes in the ISAC facility. These isotopes require particle accelerators for their production due to their rarity and short lifetimes.

The main goal of TRIUMF's new Advanced Rare Isotope Laboratory (ARIEL) is the production of radioactive isotope beams to feed into the existing experimental infrastructure within the ISAC facility. A new high power electron linear accelerator, the e-Linac, is being built to drive the production of radioactive isotopes in ARIEL. The layout of the e-Linac allows for a future upgrade that would enable a second beam to be accelerated simultaneously in the linac. This second beam will use the same accelerating cavities as the beam being used for ARIEL, while operating as an energy recovery linac.

This upgrade will make use of the infrastructure required to drive isotope pro-

duction in ARIEL for a second independent research program based on the beam accelerated by the energy recovery process to drive an advanced light source, such as a Free Electron Laser. The RF acceleration cavities and their supporting services are one of the most expensive components of the e-Linac. Multi-purposing them in this way is a cost effective way to expand TRIUMF's research program to new avenues and increase experimental availability while making more efficient use of existing infrastructure.

To not interfere with the main purpose of the e-Linac, this upgrade requires that the two beams co-propagate through the accelerator cavities without interference and be separated at the end of the main linac into their respective beam lines. An RF separator cavity has been developed to provide the time varying transverse deflecting forces required to separate the interleaved beams. The focus of this dissertation is the development of this superconducting RF separator cavity, along with its fabrication and testing.

Transverse deflecting mode RF cavities have long been used for creating multiple beams from a single input beam, such as for the 4 GeV CEBAF accelerator at the Thomas Jefferson National Accelerator Facility [1]. In more recent years, a worldwide design effort has produced several new types of deflecting mode cavity designs for use as crab cavities in the High Luminosity Large Hadron Collider (HL-LHC) upgrade [2]. The design of the separator cavity for the ARIEL e-Linac was developed from the RF-Dipole cavity geometry that was itself developed for the HL-LHC crab cavities [3] and modified to meet the requirements of the e-Linac.

The resulting 650 MHz superconducting RF deflecting mode cavity operates in a TE-like mode, and is optimized for high shunt impedance with minimal longitudinal footprint. The cavity achieves roughly 50% higher shunt impedance with 50% less length than comparable non-TM mode cavity geometries. The resulting design takes into account the RF performance, input and higher order mode coupling, multipacting, and mechanical design considerations.

Due to this cavity's low power dissipation at the operating temperature of 4.2 K and the design transverse deflecting voltage of 0.3 MV, low cost manufacturing techniques have been developed for the fabrication of the cavity. These include machining the cavity from bulk, low purity niobium, and the development of a procedure for using TIG welding to join the cavity parts. The cavity has been built in house us-

ing these non-conventional fabrication methods and is the first superconducting RF cavity to be fabricated by TRIUMF.

The completed cavity has been tested at cryogenic temperatures down to 2 K, achieving a quality factor at the design deflecting voltage of $3.8 \times 10^8$ at the operating temperature of 4.2 K. The cavity surpasses the goal quality factor and required deflecting voltage, signalling the successful application of these low cost fabrication techniques to the production of a superconducting cavity.

Potential future accelerator projects such as the International Linear Collider can require the fabrication of thousands of superconducting cavities. With this quantity of work, even small decreases in the cost of fabricating cavities can significantly impact the overall cost of such a project. On the other end of the scale, this work shows the possibility of a lab to design and fabricate superconducting RF cavities to meet the needs of their own project at low cost and without relying on contracting work out to one of the relatively few vendors that fabricate superconducting cavities world wide.

The outline of this dissertation is summarized below. Lists of the notations and definitions of the variables used in this work have been provided, preceding this chapter.

**Chapter 1** contains a statement of the goals of this work and outlines the resulting superconducting RF separator cavity that meets these requirements.

**Chapter 2** provides background information about TRIUMF and its experimental programs, and introduces the need for the RF separator cavity for an upgrade to the ARIEL e-Linac. The requirements of the separator cavity are stated here.

**Chapter 3** gives an overview of the theory of RF cavities, defining the parameters that will be used to quantify the RF performance of the separator cavity. The phenomenon of superconductivity and its application to RF cavities will be described. Finally, considerations regarding power requirements for driving the fundamental mode and damping higher order resonant modes will be introduced.

**Chapter 4** describes the design of the RF separator cavity geometry. After starting with an overview of the state of the art of deflecting mode cavities used in accelerators around the world, the development of the cavity's geometry using simulation tools will be discussed.

**Chapter 5** details the development of the low cost fabrication techniques used to build the cavity. This includes a description of the fabrication processes of both a copper prototype cavity and the final production cavity, and the studies performed to qualify the TIG welding procedure for application to superconducting RF cavities. The preparation of the completed cavity for cryogenic testing is also described.

**Chapter 6** includes the evaluation of the cavity in both room temperature and cryogenic tests, showing the successful performance of the cavity.

**Chapter 7** summarizes the design and performance of the cavity. The next steps required to ready the cavity for use on the beam line are discussed, as well as further studies that could aim to increase its performance.

# Chapter 2

# Background

TRIUMF is Canada's national laboratory for particle and nuclear physics, and operates a number of particle accelerators to meet this goal. A new addition to TRIUMF is the ARIEL e-Linac, which will drive the production of rare isotope beams (RIBs) to expand on TRIUMF's existing research programs in nuclear physics, nuclear astrophysics, materials science, and medical isotopes. This chapter will introduce the e-Linac and its future upgrade plans that require the use of a separator cavity. It will finish with a brief overview of the basic requirements of the RF separator cavity.

## 2.1 The ISAC Facility

TRIUMF's existing isotope research program is based out of the ISAC I and II facilities, which generate RIBs using the Isotope Separation On-Line (ISOL) technique [4]. The production of the radioactive isotopes is driven by a 100 µA proton beam that is accelerated by TRIUMF's 500 MeV main cyclotron. This 50 kW beam is directed onto one of two target stations, where collisions with atoms within the target induce spallation, fragmentation, and fission reactions, producing lighter, and often radioactive isotopes.

As the isotopes diffuse out of the target material and are released, they are ionized, mass separated, and accelerated to form beams of radioactive ions that are delivered to experimental stations in ISAC I and ISAC II. ISAC I contains low and medium energy experiments with RIB energies from 10's of keV, up to 0.15-1.5 MeV/nucleon after accelerating through a radiofrequency quadrupole (RFQ) and Drift Tube Linac (DTL) [5]. The beam may be further accelerated and delivered to ISAC II, by passing

through a superconducting Linac. The Linac consists of 40 quarter wave resonator (QWR) cavities providing a maximum effective voltage of 40 MV. Beams of rare isotopes can be accelerated to greater than 6.5 MeV/nucleon for isotopes with a mass to charge ratio of 6, or for lighter ions, up to 16 MeV/nucleon [6].

A number of experimental stations are housed within the ISAC facilities for studying nuclear structure and properties, nuclear astrophysics, and material properties [7]. Within the present infrastructure, a single RIB species may be produced and delivered to one experiment at a time, making ISAC a single user facility. ISAC currently provides some of the most intense beams of several isotope species in the world, and there is strong demand for experimental time.

## 2.2 ARIEL

The ARIEL project will ultimately add two new drive beams and target stations within a new facility to produce RIBs that will be injected into the ISAC beamlines. One of the drive beams will be a second 50 kW proton beam extracted from the 500 MeV cyclotron, while the second will be an electron beam used to drive the production of isotopes through the process of photofission [8]. Not only will this triple the number of beams driving the ISAC experimental program, tripling the RIB delivered to users, but photofission will also allow for greater production of neutron rich isotopes and beams with fewer isobaric contamination.

The electron drive beam will be supplied by a new high power continuous wave (CW) electron Linac, from here on referred to as the e-Linac, that is being constructed at TRIUMF [9]. The e-Linac uses 1.3 GHz superconducting RF technology to accelerate a 10 mA electron beam at 100% duty factor to a nominal energy of 30 MeV, expandable up to 50 MeV. These parameters were chosen to optimize the photofission rate within the targets where a continuous beam is required to avoid thermal cycling within the target. The photofission rate saturates at an incoming electron beam energy of ∼60 MeV, favouring a high beam current over increasing the beam energy.

Figure 2.1 shows a schematic of the e-Linac layout. Electrons are produced by a thermionic electron gun that emits 300 keV electrons bunched at 650 MHz. This is followed by an injector cryomodule containing a single 9-cell, 1.3 GHz cavity that can accelerate up to 10 MeV, and up to two accelerator cryomodules, each containing two 9-cell cavities for a total nominal beam energy of up to 50 MeV. A 60 m long

high energy beam transport will then deliver the beam to the ARIEL target stations. Initially, only the injector and a single accelerator cryomodule will be installed, containing a total of three cavities and providing a nominal beam energy of 30 MeV. Space in the beam line has been reserved to allow for the addition of the second accelerator cryomodule to be installed as a future upgrade.

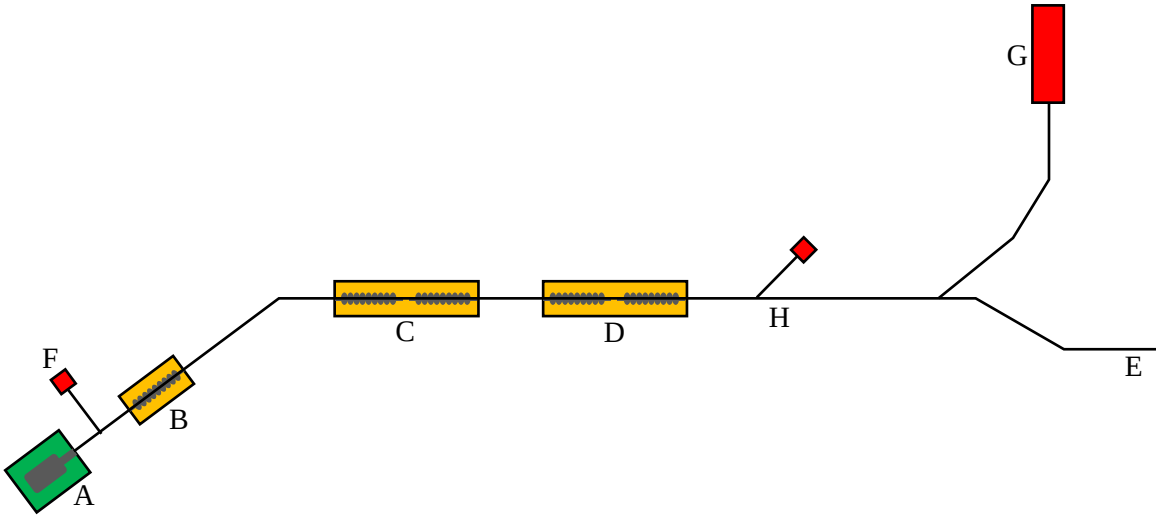


Figure 2.1: A schematic of the e-Linac showing the main components: A - the electron gun, B - the injector cryomodule, and C and D - the accelerator cryomodules. The beam line at E continues to the ARIEL target stations, while G is a high power beam dump that will be used for high power commissioning. The short beam line at F is used either as a diagnostic leg or as a test stand for prototyping converter materials.

The accelerating cavities are 1.3 GHz superconducting cavities, based on the TESLA cavity design [10]. They have been modified from the original TESLA design in the shape of the end groups, higher order mode damping method, and the addition of a second input power coupler [11]. These changes were made to allow the cavities to be operated in CW mode with high average current. The cavities operate at 2 K, with a cold plant supplying 4 K liquid helium to the cryomodules, where it is converted to 2 K on board.

Commissioning of the e-linac is ongoing, with the injector and first accelerator cryomodule, as well as the majority of the beam lines in place. The maximum beam energy achieved to date is 23 MeV with two of the three accelerating cavities installed [12]. Since that time, the first accelerator cryomodule has been completed with its second accelerator cavity installed, providing the capacity to accelerate past 30 MeV.

## 2.3 Recirculation Arc

The e-Linac may be upgraded through the addition of a recirculation arc that would connect the end of the main linac, after the final accelerating cavity, to the entrance to the first accelerator module, as shown in Figure 2.2. The return path would allow electrons to make a second pass through the accelerator cryomodules.

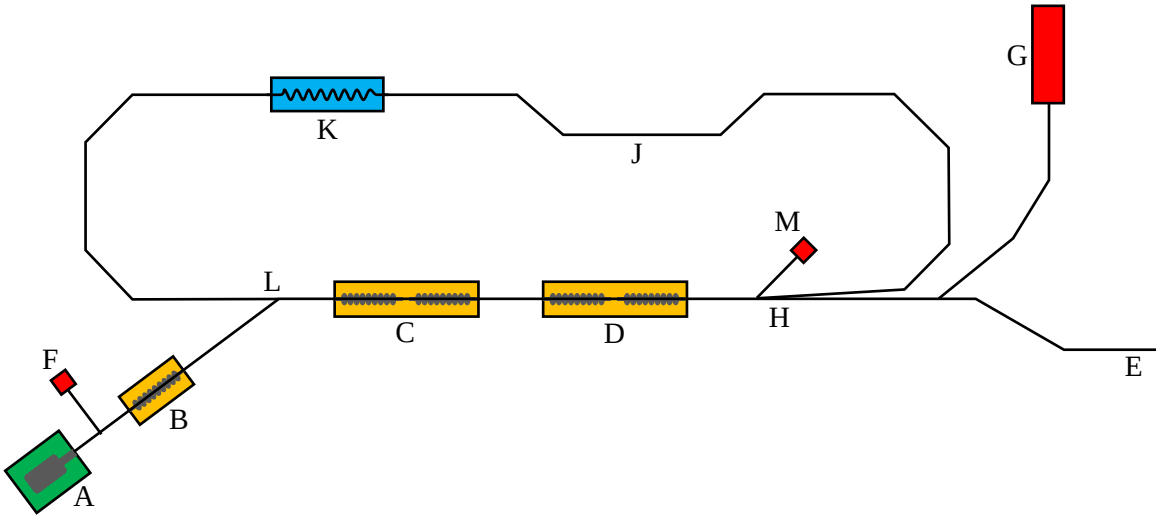


Figure 2.2: The schematic of the e-Linac with recirculation arc. The additional labels from Figure 2.1 indicate the H - separation complex, J - magnetic chicane, K - an FEL, and L - the merging section. The beam dump for the recirculated beam is at M.

The length of the return path may be tuned to vary the RF phase that the returning bunches would make their second pass through the RF cavities. In Recirculating Linear Accelerator (RLA) mode, the electrons would return to make the second pass in the accelerating phase, receiving another boost to their energy. Operating in this mode would allow for the beam to be accelerated to 50 MeV or beyond without installing the second accelerator cryomodule. Alternatively, if the return phase is 180° out of phase with the accelerating RF, the second pass electrons are decelerated by the cavities. By conservation of energy, the decelerated bunches deposit their energy back into the RF fields within the cavity. This mode is referred to as the Energy Recovery Linac (ERL) mode.

Operated as an ERL, the net power transferred to the beam by the accelerator cavities is near zero. Energy gained by the beam on the first pass through the accelerator cavities is returned on the second pass with very high efficiency. Therefore,

after the decelerating pass, the beam energy would be returned to the injection energy of 5-10 MeV, having temporarily been accelerated to higher energy while in the recirculation loop. It is possible then to use the accelerated beam for non-destructive purposes in the loop, such as an infrared or THz Free Electron Laser (FEL) or X-Ray Compton Source, before it is decelerated.

Since the production of RIBs for ARIEL is the primary objective of the e-Linac, operation in the ERL mode must not interfere with delivery of beam to ARIEL. The ARIEL beam has a bunch repetition rate of 650 MHz and therefore occupies every second bucket of the 1.3 GHz accelerating RF. The empty RF buckets allows for a second beam to be interleaved with the beam bound for ARIEL through the main linac. The two beams would require separation at the end of the main linac, with the ARIEL beam continuing on to the ARIEL target stations, and the ERL beam directed around the recirculation arc, through an FEL or other experimental device, and finally being decelerating and dumped at low energy.

Due to the high frequency of the bunch repetition rate, the separation of the two interleaved beams requires RF techniques to impart opposing transverse momentum to adjacent bunches. The concept of this separation has been studied in [13], based on the beam requirements, available floor space for the installation, beam properties, and available hardware. A limited available distance to achieve sufficient separation of the bunches to clear a septum magnet drives the separation scheme, as well as its flexibility to be used in all possible modes, i.e. when the beam is delivered to ARIEL only, delivered to ARIEL and the ERL, or in an RLA mode.

The layout of the RF separation scheme is shown in Figure 2.3. In ERL mode, separation of the ARIEL and ERL bunches will be initiated by an RF separator cavity that will impart an opposing kick of $\pm 4.4$ mrad to adjacent bunches. The beam will then pass through a dipole magnet placed immediately downstream of the RF cavity before drifting for about 1 m. When the bunches reach a defocussing quadrupole magnet, they will already be horizontally separated by roughly 15 mm. Due to the defocussing fields in the quadrupole, the bunches would receive a further 10 mrad of angular divergence, and would be separated by over 3 cm by the time they reach the septum magnet. This is enough separation for the septum to capture the distinct beams and steer them along their separate transport beam lines. In this scheme, the total separation of the three beams is achieved within about 3 m.

The separation needs to be initiated by an RF source since the ARIEL and ERL beams are the same energy and are temporally separated by less than 1 ns. For

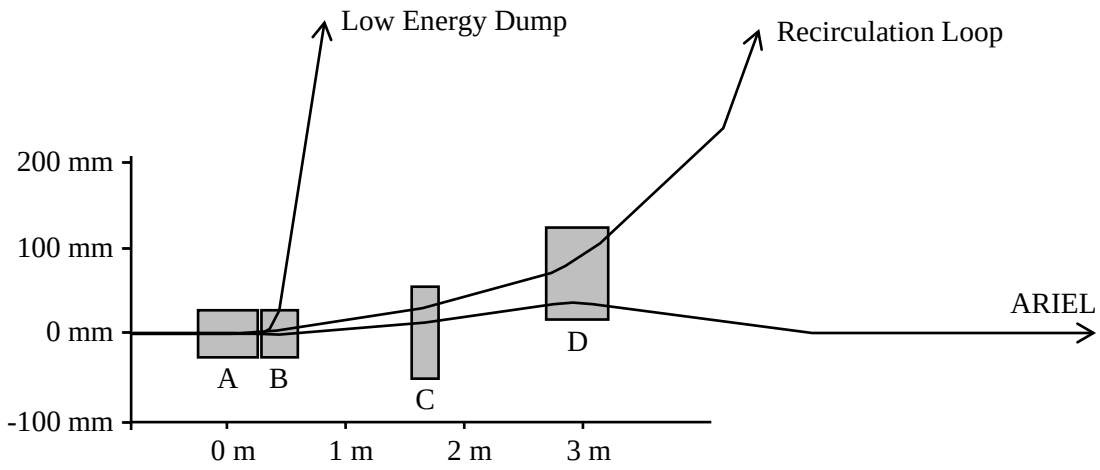


Figure 2.3: Layout of the main components that make up the separator complex, A - the RF separator, B - dipole magnet, C - quadrupole magnet, and D - the septum. The beams are directed onto one of three pathways – to the ARIEL target stations, the recirculation arc, or to the low energy beam dump. The horizontal position of the beam is shown on the vertical axis. The components are not shown to scale.

the separator cavity to impart opposing momentum to adjacent bunches spaced at 1.3 GHz, the fields should oscillate at half of this frequency, 650 MHz, such that the bunches pass through the cavity at $+90°$ and $-90°$ phase.

The dipole magnet is included in the layout for several reasons. In ERL mode, the decelerated beam would pass through the RF separator cavity a second time, but in the zero crossing phase and would not receive any net transverse momentum. When passing through the dipole magnet, the decelerated beam would experience a much smaller turning radius than the first pass beams due to its lower forward momentum, and would be steered onto a separate beam line that would deliver the beam to the beam dump. In RLA mode, the RF cavity would not be used, and the separation of the beams would be achieved by the static separation due to the different energies of the first and second pass beams. In this case, the strength of the dipole, quadrupole, and septum may be tuned such that the beams would follow the same trajectory through the separation complex as in the ERL mode.

The pathways of the three beams existing simultaneously in the e-Linac when operated in ERL mode are shown in Figure 2.4. The beams bound for ARIEL and the ERL share the injector, although will require an upgraded or independent electron source to provide the required bunch structure. After the ERL beam is separated and

returned via the recirculation arc, three beams will co-propagate through the accelerator cavities: the ARIEL beam and first pass ERL beam in adjacent acceleration buckets, and the second pass ERL beam in the decelerating phase. The separator complex is located at the end of the main linac, providing complete separation of the three beams within a distance of about 3 m.

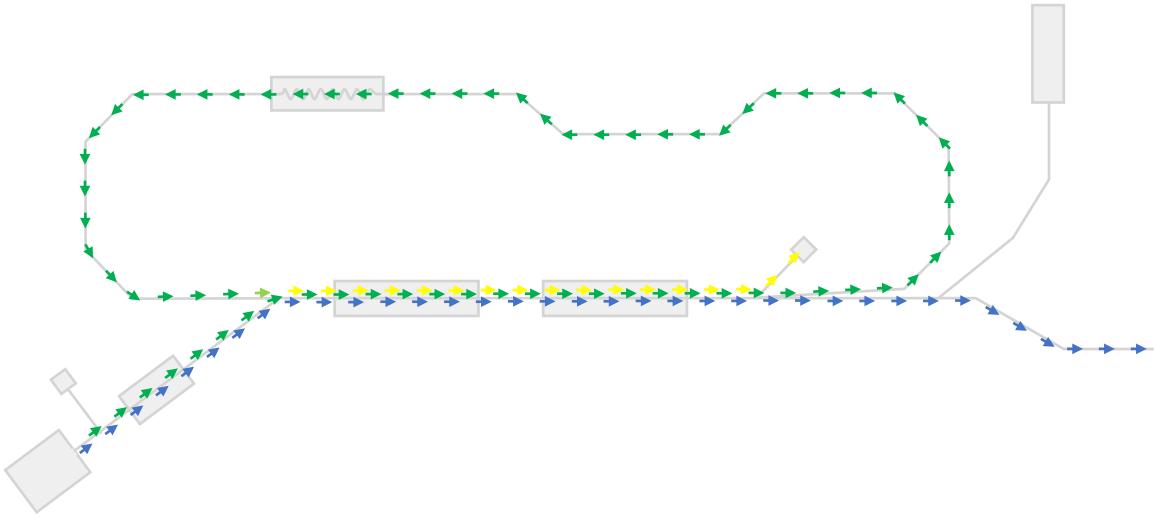

Figure 2.4: The path of the three simultaneous beams passing through the eLinac in ERL mode. The beam bound for ARIEL is shown in blue, the ERL beam in green, and the decelerated ERL beam in yellow on its second pass through the linac.

## 2.4 Requirements of the RF Separator Cavity

A 650 MHz RF separator cavity is required to initiate the separation of the interleaved ERL and ARIEL beams. Imparting a time varying horizontal deflection to the beam allows it to be split three ways due to the phase of the arrival of the bunches, as shown in Figure 2.5. The beams bound for ARIEL and the recirculation loop arrive in the cavity 180° out of phase with each other and receive maximal deflection in opposing directions. The decelerated bunch arrives in the zero crossing phase, receiving no net deflection.

An angular deflection of ±4.4 mrad is required to provide sufficient separation of the ARIEL and ERL beams for the separation scheme described in [13]. At a nominal energy of 50 MeV, this corresponds to an imparted transverse momentum of 0.225 MeV/c. The nominal required voltage has been set as slightly higher, at 0.3 MV

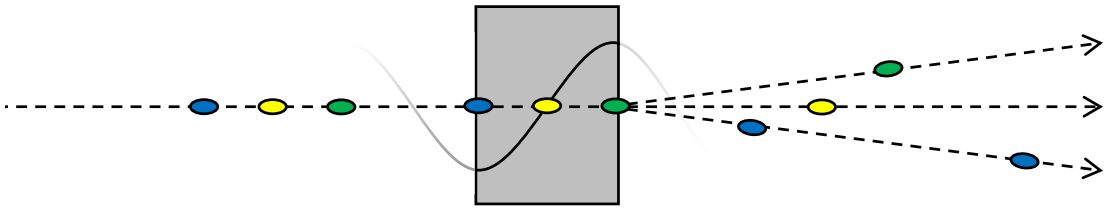

Figure 2.5: Three way beam separation by the RF separator cavity. The incoming beams see different RF phases in the RF separator cavity, and therefore receive a time dependant transverse force. The blue bunches represent the ARIEL beam, the green bunches the first pass ERL beam, and the yellow bunches the 2nd pass ERL bunches which do not receive a net force from the RF separator.

to account for increased acceleration possible at the maximum installed cryogenic capacity. A further increased goal of 0.6 MV is considered to allow for flexibility of the design of the separation scheme.

The ARIEL beam will operate in CW mode with bunches of charge 16 pC spaced by 650 MHz. For FEL operation, a high brightness mode is required with bunch charges of $\sim 100$ pC at a lower repetition rate. The maximum total current of both beams will be up to 20 mA.

The design parameters of the incoming RIB beam are a normalized RMS emittance of 5 mm-mrad in both $x$ and $y$ and the transverse RMS beam widths on entering the RF separator cavity of approximately 0.7 mm by 0.4 mm respectively, as determined from the e-Linac optics [14]. The energy spread of the first pass beams will be around 0.5%. After deceleration in the main linac, the beam will have an energy of 5 to 10 MeV – equal to the injection energy, and with a significant energy spread of about 5% and a bunch length of up to 6.5 mm RMS.

Successful operation of an FEL requires a beam with low emittance, and therefore minimal emittance dilution of the ERL beam as it passes through the RF separator. The Jefferson Lab FEL, an infrared FEL with similar design parameters, successfully operates with a transverse emittance (RMS) of approximately 9 mm-mrad [15, 16]. An upper limit for the emittance growth through the RF separator has therefore been set as approximately 25% to ensure it does not interfere with lasing of the FEL.

# Chapter 3

# RF Cavity Basics

RF cavities are structures that support resonant electromagnetic modes that can generate relatively strong oscillating electric and magnetic fields. These fields can be used to apply forces to charged particles to control their motion within particle accelerators. Depending on the orientation and phase of the fields experienced by a particle bunch, this can accelerate the particles to increase or decrease their energy, or apply transverse forces that deflect their trajectory.

This chapter will introduce some basic types of RF cavities and resonant modes, the parameters that describe their RF performance, and some basics of normal conducting and superconducting RF (SRF). The MKS system of units will be used throughout this work.

## 3.1 Resonant Modes

A cavity will support a discrete set of eigenmodes, each with characteristic frequencies and electromagnetic field patterns. The geometry of the cavity determines the frequency and field distribution of these modes. In addition to the desired operating mode, an infinite number of other resonant modes exist for any cavity geometry. This can include modes with frequencies below the desired operating mode frequency, called lower order modes (LOMs), or more commonly, at higher frequencies – higher order modes (HOMs).

The mode solutions may be determined by solving Maxwell's equations inside the cavity space with the boundary conditions defined by the geometry of the cavity walls and ports. For a conducting cavity wall, these boundary condition state that

the electric field vector must be perpendicular to the surface, while the magnetic field be parallel.

This can be envisioned by a simple geometry that may be solved analytically. The pillbox cavity is comprised of a simple cylindrical shape. For this geometry, the solution to Maxwell's equations provide a general solution for all resonant modes. These modes can be classified as either TE modes with no longitudinal electric field, or TM with no longitudinal magnetic fields. Although not present in the pillbox geometry, TEM modes that have both electric and magnetic field components in the transverse plane may be supported by other cavity geometries. The modes can be further classified by the indices $m$, $n$, and $p$, which indicate the number of nodes in the field pattern in each axis.

The lowest frequency TM mode in the pillbox cavity is the $\mathrm{TM}_{mnp}$ mode labelled $\mathrm{TM}_{010}$, meaning the electric field has zero nodes in the azimuthal direction, one node in the radial, and zero in the longitudinal directions. From the solution to Maxwell's equations, the electric, $E$, and magnetic, $H = B/\mu_0$, fields in this mode are

$$E_z(r,t) = E_0 J_0(k_1 r)\cos(\omega_1 t), \tag{3.1}$$

$$H_\phi(r,t) = -\frac{E_0}{\eta} J_1(k_1 r)\sin(\omega_1 t), \tag{3.2}$$

where $E_0$ is the amplitude of the electric field, $J_m$ are $m$-th order Bessel functions, $\eta$ is the impedance of free space, and $\omega_1 = ck_1$ is the angular frequency of the mode.

The fields oscillate with the electric and magnetic fields 90° out of phase with each other. The phase is generally defined such that at 0°, there is maximal electric field present in the cavity while the magnetic field is zero. At this point, charge has built up on the end caps of the pillbox cavity that drive this electric field. As the phase progresses, currents flow on the conducting surface of the cavity, decreasing this charge build-up causing the electric field to decrease while increasing the magnetic field up to its maximum value at 90°. In this way, the electric and magnetic fields oscillate at the frequency of the mode, transferring the stored energy within the cavity between the electric and magnetic fields.

For all but the simplest of cavity geometries, an analytical solution to Maxwell's equations cannot be determined. In these cases, computer codes that employ numerical methods to determine the mode frequencies and fields are used, such as HFSS [17], ACE3P [18], or ANSYS [19]. Many other codes exist, but these three are the ones primarily used in this work. In these codes, the cavity shape is defined which

sets the boundary conditions imposed by the conducting surfaces. Open ports may be defined, as well as material properties such as conductivity and dielectric properties. In some cases, planes of symmetry may be used to reduce the size of the model without losing accuracy.

In the Finite Element Method (FEM) of determining the electromagnetic field solution, the cavity volume is discretized into a large number of smaller volumes, called elements, that collectively make up the finite element mesh. The vertices of these elements, called nodes, are shared by their neighbouring elements and couple the equations across the entire mesh together. This transforms Maxwell's equations into a matrix equation that can be numerically solved, providing the field values $E$ and $H$ at the nodes, and the mode frequency. These codes will be discussed in more detail in Section 4.3.

## 3.2 Types of RF Cavities

RF cavities are employed in a wide range of applications in particle accelerators, requiring a diverse set of cavities to fill these many roles. These include variations in the shape as well as the materials the cavities are made from.

Accelerating cavities are used in most cases to accelerate the beam to higher energy, but can also decelerate the beam. These are often $TM_{010}$ mode cavities, coaxial type resonators such as half wave (HWR) or quarter wave resonators (QWR), or more complex cavity shapes such as radio-frequency quadrupoles (RFQ) or drift tube linacs (DTL). Each cavity has their own advantages and disadvantages for beams of different bunch repetition rate, particle velocity, and beam loading. As an example, the ISAC accelerator uses a range of cavity shapes as the ion beam accelerates, each optimized for a range of particle velocities, or $\beta$, [20]. As it is released from the source, the beam first passes through an RFQ, then through a set of DTLs, and finally through the superconducting linac with 40 QWR cavities.

Cavities operating in a mode with transverse electric and/or magnetic fields can be used to impart transverse momentum to the beam. Depending on the RF phase in the cavity when a bunch passes through, this can lead to the deflection of an entire bunch, or differential momentum applied to the head versus the tail of a bunch causing it to rotate for crabbing or diagnostic purposes – translating longitudinal position to a transverse deflection.

There are also passive RF cavities, which couple to the beam passing through

them to drive the fields within. Examples of such cavities are either for the purpose of beam diagnostics, where the power coupled into the cavity can provide information on the beam position [21], or for boosting luminosity by decreasing bunch length [22].

Cavities can be fabricated from either normal conducting or superconducting materials. Normal conducting cavities are often made from copper, usually operating at room temperature and are water cooled. Copper has relatively high electrical and thermal conductivities, which is important for the removal of the heat dissipated on the inner cavity surfaces. The typical material used for the fabrication of superconducting cavities is ultra-pure niobium. This material becomes superconducting below a temperature of 9.25 K. Other superconducting materials such as lead have been used in the past [23], and new possibilities for cavity materials include higher temperature superconductors, such as $Nb_3Sn$ [24] or $MgB_2$ [25], or multilayered surfaces [26]. In the meantime, new processing techniques such as nitrogen doping [27] are steadily pushing the limits of bulk niobium.

Niobium and other superconductors have surface resistances that are on the order of $10^6$ times lower than normal conductors, leading to much reduced RF power dissipation on the cavity walls. However, since superconducting cavities currently need to be cooled to cryogenic temperatures, this heat must also be removed at low temperature with relatively poor thermodynamic efficiency. Taking both RF resistance and cooling efficiency into account, the use of superconducting material can reduce the overall power required to operate RF cavities in some cases by orders of magnitude. Under certain conditions, the use of superconducting cavities becomes a requirement, such as when operating at high field and CW. A more detailed treatment of the mechanisms responsible for losses in SRF cavities follows in Section 3.4.2.

## 3.3 RF Performance Parameters

RF cavities are designed to optimize the behaviour of the operating mode while diminishing the effects of parasitic LOMs and HOMs. To characterize the cavity behaviour, a number of parameters have been defined that describe the performance of RF cavities. These will be introduced in the following sections.

### Cavity Voltage

RF cavities can impart a net force on particles as they pass though the electric and magnetic fields present inside the cavity. The momentum change of a particle with charge $q$ can be determined by integrating the Lorentz force along the path of the particle. For a particle travelling along the cavity axis of a resonant cavity oscillating at a frequency $\omega$ at phase $\phi$, the longitudinal and transverse components of this momentum change are

$$\Delta p_z = \int_{-\infty}^{+\infty} qE_z(z)\cos(\omega t + \phi)dt, \tag{3.3}$$

$$\Delta \vec{p}_\perp = \int_{-\infty}^{+\infty} q\left(\vec{E}_\perp(z)\cos(\omega t + \phi) + \vec{v}\times\vec{B}_\perp(z)\sin(\omega t + \phi)\right)dt, \tag{3.4}$$

defined in the coordinate system with the $z$-axis aligned with the beam axis, $x$ along the horizontal axis, and $y$ in the vertical axis.

The change in momentum can be expressed as a voltage, $V = c\Delta p/q$. This quantity is often called the *cavity voltage* and is the average voltage gained or lost by the particle as it passes through the cavity. At a phase $\phi = 0$, and for a particle travelling at a velocity $v = \beta c$, the integral of the longitudinal electric field through the cavity of length $L$ will give the accelerating voltage,

$$V_{acc} = \int_{-L/2}^{+L/2} E_z(z)\cos(\frac{2\pi f z}{\beta c})dz, \tag{3.5}$$

and in the transverse direction, with the fields imparting a net force in the $x$-direction,

$$V_\perp = \int_{-L/2}^{+L/2}\left(E_x(z)\cos\left(\frac{2\pi f z}{\beta c}\right) - \beta c B_y(z)\sin\left(\frac{2\pi f z}{\beta c}\right)\right)dz. \tag{3.6}$$

In the transverse direction, the momentum gained by a particle can also be determined from the Panofsky-Wenzel theorem [28] using the gradient of the longitudinal electric field

$$\Delta \vec{p}_\perp = -\int_{-\infty}^{+\infty} \frac{iq}{\omega}\vec{\nabla}_\perp E_z dz. \tag{3.7}$$

### Field Gradient

Another way to quantify the strength of the fields in a cavity is the cavity *gradient*, $E$, in units of V/m. This is the average electric field experienced by a particle passing through the cavity. For an accelerating cavity, this is $E_{acc} = V_{acc}/L$. For a deflecting mode cavity, the reference length $L$ may be taken as $n\lambda/2$ where $n$ is the number of cells. So a transverse deflecting field gradient for a single cell deflecting cavity is therefore

$$E_{\perp} = \frac{V_{\perp}}{\lambda/2}. \tag{3.8}$$

### Quality Factor

In supporting the electromagnetic fields within the cavity, surface currents flow on inner cavity surfaces and dissipate power on the cavity walls, $P_c$, due to the resistance the current experiences. The dissipation of power occurs within a thin layer on the surface, with a surface resistance, $R_s$. A useful figure of merit for accelerator cavities is the *quality factor* which relates the energy stored within the cavity, $U$, to the energy dissipated per radian of RF oscillation,

$$Q_0 = \frac{\omega U}{P_c}. \tag{3.9}$$

Since $P_c$ is proportional to the surface resistance, a new parameter called the *geometry factor* can be defined that is independent of the properties of the surface material as

$$G = R_s Q_0 = \frac{\omega U}{(P_c/R_s)}, \tag{3.10}$$

assuming the surface resistant is constant and equal to $R_s$. The geometry factor is a useful design parameter as it depends only on the geometry of the cavity, but is independent of size, material or cavity treatments, nor does it scale with the cavity voltage. This makes it an informative parameter for comparing different cavity designs. A higher value of $G$ (and therefore $Q_0$) indicates lower dissipated power for the same RF surface resistance.

In addition to power losses on the cavity walls, there can be power losses from the cavity to other elements such as power couplers, beam ports, RF pick-ups, HOM dampers, etc. These contribute their own quality factors, referred to as *external*

*quality factors*, defined using the external power loss through each source $P_{ext_i}$.

$$Q_{ext_i} = \frac{\omega U}{P_{ext_i}}. \tag{3.11}$$

Since the total power loss from the cavity is given by the sum of all the sources of power loss, $P_{tot} = P_c + P_{ext_1} + P_{ext_2} + ...$, an overall quality factor can also be defined. This is referred to as the *loaded quality factor*, $Q_L = \omega U / P_{tot}$, which can be expanded to

$$\frac{1}{Q_L} = \frac{1}{Q_0} + \frac{1}{Q_{ext_1}} + \frac{1}{Q_{ext_2}} + ... \tag{3.12}$$

In the time domain, the quality factor defines the decay constant $\tau = Q_L/\omega$ that the energy stored in the RF fields would dissipate when the driving power is turned off. In the frequency domain, the quality factor gives the 3 dB bandwidth of the resonance curve, $\Delta\omega = \omega/Q_L$.

### Shunt Impedance

The shunt impedance describes how efficiently a cavity transfers voltage to the beam in comparison to the power dissipated on the cavity walls. The definition of the transverse shunt impedance that will be used in this thesis, in units of $\Omega$, is

$$R_\perp = \frac{V_\perp^2}{P_c}. \tag{3.13}$$

A higher value of the shunt impedance would imply less power required to impart the desired voltage from the cavity.

Again, to avoid the dependency on $R_s$ brought in through $P_c$, the shunt impedance may be divided by the quality factor, which also scales as $1/R_s$, resulting in a term referred to as the geometric shunt impedance, $R$ *over* $Q$, as it only depends on geometry and not material properties.

$$R_\perp/Q = \frac{V_\perp^2}{\omega U} \tag{3.14}$$

Similar to $G$, $R_\perp/Q$ also does not scale with deflecting voltage.

Maximizing both $R_\perp/Q$ and $G$ independently can lead to conflicting design goals, as the geometry that maximizes one often does not maximize the other. However, minimizing the power loss on the cavity walls can be shown to be equivalent to

maximizing the product of these two quantities, $R_\perp/Q \cdot G$. Manipulating this product yields:

$$R_\perp/Q \cdot G = R_\perp/Q \cdot R_s Q_0 = R_\perp R_s. \tag{3.15}$$

Since $R_s$ is a parameter of the surface material and is independent of geometry, optimizing the geometry for maximal $R_\perp/Q \cdot G$ will maximize $R_\perp$ and minimize the power dissipated on the cavity walls.

## 3.4 Cavity Materials

The power loss on the cavity walls is driven by the magnetic field component of the RF fields. A changing magnetic field on the conducting surface drives electrons within the bulk of the material into motion, causing a surface current to flow. This current results in a power dissipation that is proportional to the surface resistance.

The two commonly used materials for fabricating RF cavities are copper operating at room temperature, or niobium in the superconducting state held at cryogenic temperatures. The surface resistance of these two materials are vastly different, by an order of $\sim 10^6$, however, when cryogenic efficiency is taken into account, removing heat at a temperature of a few K results in an overall efficiency gain of superconducting cavities of only $10^2 - 10^3$ times.

### 3.4.1 Normal Conductivity

An RF field applied to a conducting surface will penetrate a short distance into the surface before dropping to zero. It is this field that drives a surface current that leads to wall losses. Solving Maxwell's equations for the fields within a good conductor in response to an oscillating surface electric field of $E = E_0 e^{i\omega t}$ gives

$$E(x) = E_0 e^{-x/\delta} e^{-ix/\delta}, \tag{3.16}$$

where $x$ is the distance from the surface and $\delta$ is the decay constant referred to as the *skin depth*, a term that quantifies how far into the conductor the RF fields penetrate. This skin depth depends on the conductivity of the material, $\sigma$, and the frequency of the applied field, and is given by

$$\delta = \frac{1}{\sqrt{\pi f \mu_0 \sigma}}. \tag{3.17}$$

The surface resistance is defined as

$$R_s = \frac{1}{\sigma\delta} = \sqrt{\frac{\pi f \mu_0}{\sigma}}. \tag{3.18}$$

As discussed previously, the power dissipated on the surface is proportional to the surface resistance. The time averaged power dissipation on a surface area $dS$ is driven by the magnetic field strength $H$ and is given by

$$dP = \frac{1}{2} R_s H^2 dS. \tag{3.19}$$

For copper at room temperature and at frequency of 100's of MHz, the conductivity is roughly $6 \times 10^7$ S/m, resulting in a skin depth on the order of µm's and an RF surface resistance of mΩ's.

### 3.4.2 Superconductivity

Although niobium is a relativity poor conductor at room temperature, it belongs to a class of materials called superconductors that when cooled below a critical temperature, $T_c$, their DC resistance vanishes allowing lossless transmission of current. The RF surface resistance does not drop to zero, but still decreases dramatically to much below what could be explained by the typical normal conducting physics.

The phenomenon of superconductivity was first discovered in mercury in 1911 [29], after it became possible to make liquid helium. Following this initial discovery, a number of other pure elements such as niobium and lead were also found to exhibit this behaviour, as well as some metallic alloys or complex ceramics that can have relatively high critical temperature, giving this last group the name *high temperature superconductors*. The highest temperature superconductor discovered to date is hydrogen sulfide. Under extreme pressure, 155 GPa, this material exhibits a critical temperature of 203 K (-70°C) [30].

#### The Meissner Effect

The transition to a perfect DC conductor is not the only defining characteristic of superconductivity. Another required attribute has to do with how a superconduc-

tor behaves in a magnetic field. When cooled below $T_c$, superconductors resist the presence of magnetic fields within their bulk. This means that if a superconductor is cooled while within a magnetic field[1], the magnetic flux passing through the material will be expelled, resulting in a flux-free superconducting volume. The expulsion is driven by currents that are induced on the superconductor surface that screen the volume within from the external field. This effect is known as the *Meissner effect*.

A *Type I* superconductor will remain flux free under an applied magnetic field, up to some critical value $H_c$ where it becomes energetically favourable to transition back into a normal conducting state, allowing the magnetic fields to penetrate back into the bulk of the material. Below $H_c$, the superconductor exists in the Meissner state and remains field free, and above $H_c$, the field penetrates in, destroying the superconducting state.

*Type II* superconductors experience a more gradual breakdown from the Meissner state. These superconductors are often alloys but include some pure elemental metals like niobium. Two critical fields exist in this type of superconductor. Below the first, $H_{c1}$, Type II superconductors exist in the Meissner state with all magnetic flux expelled from within. Between $H_{c1}$ and $H_{c2}$, the superconductor enters into a vortex phase, where some magnetic flux is allowed to penetrate into the superconductor, but is contained within small normal conducting cores spread throughout material called vortices. Within a vortex, a small current loop circulates, containing a quantum of flux, $\Phi_0$.

As the applied field increases, more of these quantized vortices exist within the superconductor, increasing the average field within the bulk. Above the upper critical field, $H_{c2}$, the superconductor breaks down completely and fully transitions into the normal conducting state. It is important to note that the critical fields are temperature dependent quantities and have their highest values at $T = 0\,\mathrm{K}$, and decrease to zero as the temperature reaches $T_c$. SRF cavities typically operate at fields below $H_{c1}$ where the losses are the lowest.

The screening currents that flow on the surface or around vortex cores penetrate a small distance into the superconductor, with a length scale called the London penetration depth, $\lambda_L$. The current and magnetic field intensities decrease exponentially inside the material at a rate of $\lambda_L$.

Another important length scale in superconductivity is the coherence length, $\xi$, that is proportional to the mean free path of electrons with the material. The magni-

[1] that is below some critical field value

tude of these two length scales determines which type of superconductor the material will behave as. If $\xi > \sqrt{2}\lambda_L$, the material will be a Type I superconductor, otherwise it will exhibit Type II behaviour.

### BCS Theory

At temperatures below $T_c$, the DC resistance of a superconductor will go to zero while an RF resistance remains, although much decreased from normal conducting levels. This behaviour is described by the BCS theory [31], developed by Bardeen, Cooper, and Schrieffer. BCS theory was the first microscopic description of the phenomenon of superconductivity.

BCS theory explains that when in the superconducting state, some number of conduction electrons pair into so called *Cooper Pairs* that are weakly coupled together by vibrations in the lattice of ions within the material. The long range attractive force between paired electrons can be viewed as the exchange of phonons, where the lattice deformation caused by the passage of one electron attracts a second electron at a distance. This mutual attraction between electrons forming a Cooper pair, causes the pair to take the behaviour of a single particle that acts like a boson. As bosons, Cooper pairs can all take the same ground state energy, forming an energy gap between this ground state energy and the energy state a free, unpaired electron would take.

A DC current flowing through a superconductor is carried by the Cooper pairs. Due to the energy gap, there exists an energy barrier to splitting a Cooper pair and raising it to the unpaired energy level. This means that the Cooper pairs do not scatter and therefore do not contribute to resistive losses. The fraction of the conduction electrons that form Cooper pairs varies with temperature, with no pairs formed at $T = T_c$, while at $T = 0\,\mathrm{K}$ all of the electrons become paired. The Cooper pairs screen any unpaired electrons and as a result, the unpaired electrons stay in place and do not contribute to the resistance. Therefore, a DC current can be carried by a superconductor with zero resistance.

If an RF field is applied, the time varying motion of the Cooper pairs results in the imperfect screening of the unpaired electrons near the surface of the superconductor. The free electrons may then be accelerated, leading to collisions and introduces a mechanism for resistive losses. The result of this is a small surface resistance for superconductors in an RF field.

The resulting RF surface resistance, called the *BCS resistance*, depends on the frequency of the applied RF fields, the temperature of the superconductor, and properties of the superconducting material such as critical temperature, energy gap, and the different length parameters. The surface resistance has been modelled using BCS theory for low fields [32], with good agreement to measured data. A simple analytical formula for the surface resistance is not possible, however computer codes can provide an accurate calculation for a given set of parameters [33]. For temperatures below $T_c/2$, the BCS resistance follows the approximate formula [34]

$$R_{BCS}(f,T) = A\frac{f^2}{T}e^{-\Delta/(k_B T)}, \tag{3.20}$$

where $A$ is a material dependant constant, $\Delta$ is the energy gap, and $k_B$ is the Boltzmann constant.

For the standard parameters of a TESLA style 1.3 GHz accelerator cavity fabricated from high purity niobium and operating at 2 K, the BCS resistance is about 10 n$\Omega$, compared to 100's of n$\Omega$ if operated at 4.2K. For a 650 MHz cavity, the BCS resistance at 4.2 K is 200–300n$\Omega$'s, depending on the purity of the niobium. The temperature dependence of the BCS surface resistance at 650 MHz is plotted in Figure 3.1.

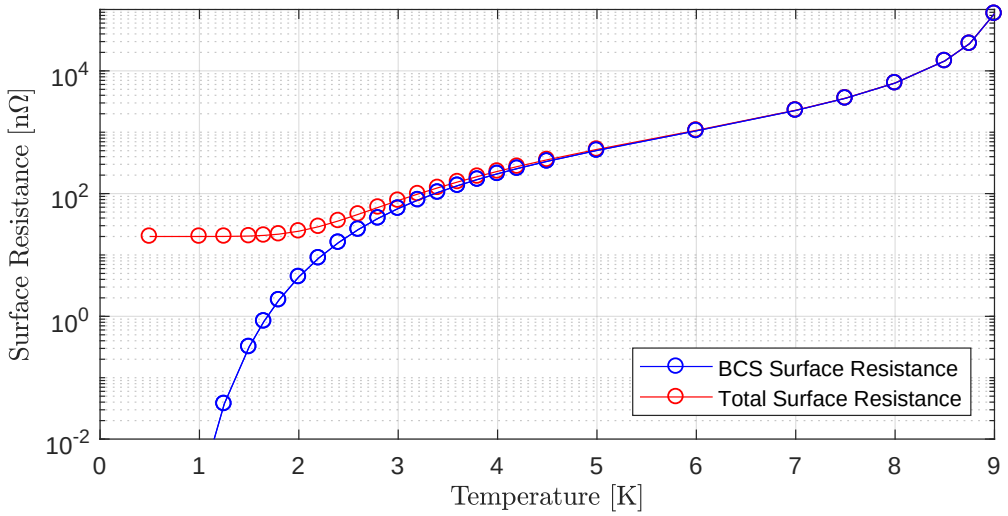


Figure 3.1: The temperature dependence of the BCS resistance at 650 MHz, calculated from [35] using *RRR* 200 niobium. The actual low field resistance that would be measured on a cavity surface would diverge from the BCS calculation at low temperatures, due to a non zero residual resistance, 20 n$\Omega$ in this case.

### Total Surface Resistance

As shown in Figure 3.1, the total surface resistance that would be measured on a cavity decreases with temperature, but approaches a fixed value as the BCS component becomes negligibly small. The remaining component to the surface resistance is referred to as the residual resistance and accounts for all other loss mechanisms, including material defects, insufficient cleaning, and others.

An important contribution to the residual resistance can be caused by trapped magnetic flux due to the incomplete expulsion of magnetic fields during the cool down process. If left unshielded, the earth's magnetic field can result in 10's of nΩ of residual resistance. The sensitivity of a cavity to trapped flux decreases with the mean free path [34]. Another loss mechanism is Q disease, an affliction caused by dissolved hydrogen within the niobium forming a lossy niobium hydride compound on the cavity surface under certain conditions.

As it is generally difficult or impossible to separate the individual contributions to the residual resistance, they are generally combined in a single term, $R_{res}$. The resulting total surface resistance is then

$$R_s = R_{BCS}(T, B) + R_{res}(B). \tag{3.21}$$

Typical residual resistances for well prepared cavities are on the order of several nΩ. As can be seen in Figure 3.1, when the BCS resistance term is low, such as when operating at 2 K, minimizing the residual resistance becomes very important to minimizing cavity losses.

## 3.4.3 Material Impurities

The purity of a superconducting material is an important parameter in determining its behaviour when fabricated into a superconducting cavity. The purity affects both the surface resistance and thermal conductivity. In conductive metals, the free electrons in the material participate in the transfer of both heat and electricity. This explains why the best electrical conductors are often good thermal conductors of heat.

The purity of a conducting material can be described by a term called the *Residual Resistivity Ratio*, or the *RRR*, defined as the ratio of the resistivity, $\rho$, at room temperature to the normal conducting resistivity at the temperature of liquid helium at 1 atmosphere, 4.2 K.

$$RRR = \frac{\rho(300\,\mathrm{K})}{\rho(4.2\,\mathrm{K})} = \frac{\sigma(4.2\,\mathrm{K})}{\sigma(300\,\mathrm{K})} \tag{3.22}$$

Since the transfer of heat and electricity is being carried out by free electrons within the material, as they move through the crystal structure they scatter off of defects and impurities in the crystal lattice that impede their motion. This scattering is the source of thermal and electrical resistance. The more scattering sites that exist, the higher the resistance, therefore a higher purity results in a higher value of $RRR$.

As the RF surface resistance can be attributed to a normal resistance from the unpaired electrons in BCS theory, the $RRR$ will also affect the RF surface resistance, although in a more complex way. The minimum BCS surface resistance is actually found for intermediate values of $RRR$, rather than steadily decreasing with increasing purity as might be expected. This is shown in Figure 3.2. At low values of $RRR$, the mean free path, or the average distance a conduction electron travels before scattering, decreases with increasing $RRR$, resulting in decreasing surface resistance. This is referred to as the *dirty limit*, where the surface resistance is dominated by scattering of electrons off of impurities. In the clean limit, at $RRR$ values above the minimum resistance point, the surface resistance becomes proportional to the normal conducting conductivity, and therefore increases with increasing mean free path.

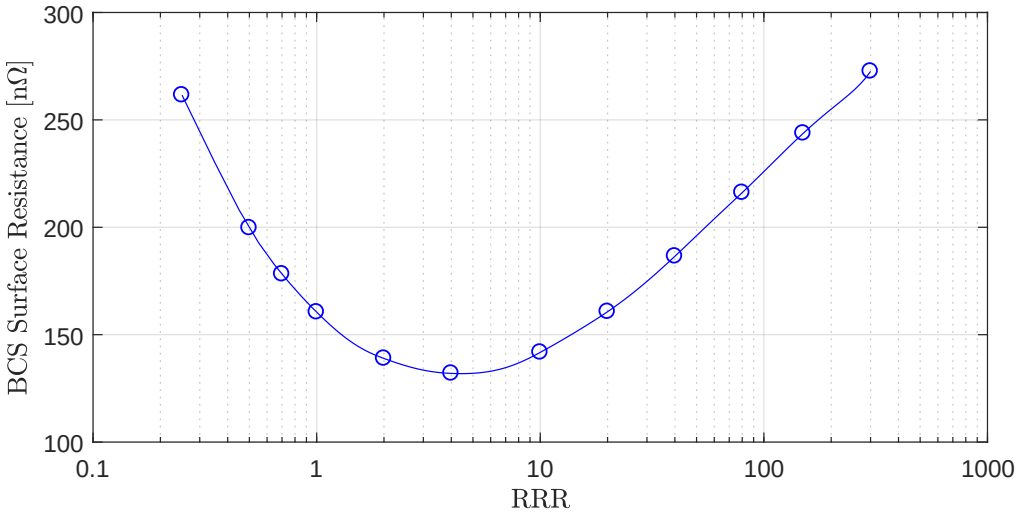


Figure 3.2: The dependence of the BCS resistance at 650 MHz and 4.2 K on the material purity, calculated from [35]. The regime left of the minimal surface resistance is referred to as the dirty limit, whereas to the right is the clean limit.

Another contribution of the material purity for superconducting cavities is the

effect of $RRR$ on the thermal conductivity. In general, the thermal conductivity is proportional to $RRR$ and at 4 K, its value for niobium is approximately [34]

$$\kappa = \frac{RRR}{4}\,\mathrm{W/mK}. \tag{3.23}$$

The thermal conductivity is an important parameter for superconducting cavities as it is required to efficiently remove the RF power that is dissipated on the inner cavity surface to the liquid helium coolant surrounding the cavity. If the $RRR$ of the cavity material is too low, resulting in a poor thermal conductivity, local RF heating can increase the surface temperature, leading to an increase of the surface resistance or can even quench the cavity.

### Contributions to RRR from Impurities

Pure niobium has a theoretical maximum $RRR$ of $\sim$ 35000 [36] which can be attributed to electron-phonon scattering in the regular niobium crystal lattice. Dissolved impurities, defects, and surface or grain boundaries all impact the $RRR$ by introducing scattering sites into the lattice. Substitutional impurities are caused by elements dissolved into the material that replace a niobium atom within the lattice. Elements such as tantalum, tungsten, or other refractory metals often fit into this category. Since they are replacing an atom, their effect on the crystal structure is minimal and has a relatively small effect on electron scattering, resulting in a low sensitivity contribution to the $RRR$.

Other impurities, mainly oxygen, carbon, nitrogen, and hydrogen, cause interstitial impurities where the atom sits between regular lattice sites in the crystal structure. These are much more effective at scattering electrons, and therefore cause a more significant change to the $RRR$ of a material.

The effect of the impurities' contribution to the $RRR$ of niobium was determined in [36] by measuring the resistance of samples doped with known impurity concentrations for the common elemental impurities. These are summarized in Table 3.1 and come into the $RRR$ by summing the contributions in parallel as

$$\frac{1}{RRR} = \frac{1}{RRR_{ideal}} + \sum_{imp.} \frac{1}{RRR_{imp.}} w_{imp.}(\mathrm{ppm}). \tag{3.24}$$

Niobium is available over a range of $RRR$ values, with the cost increasing with increased purity. The main process used to drive out the impurities from niobium

Table 3.1: Contribution to the *RRR* from some common elemental impurities at 1 ppm concentration [36].

| Element | Contribution at 1 ppm weight |
|---|---|
| Tantalum | 1 700 000 |
| Tungsten | 700 000 |
| Oxygen | 5700 |
| Carbon | 4500 |
| Nitrogen | 4400 |
| Hydrogen | 2100 |

is heating it to past its melting point while under vacuum. Niobium is a refractory metal with a very high melting point, so when it is hot enough to become molten, impurities with higher vapour pressures are boiled off and are removed by the vacuum system.

The niobium is melted by aiming electron beams at the end of an *ingot* to melt the niobium, allowing it to drip down and pool below, forming a new cylindrical ingot below as the molten niobium solidifies. The new ingot can be remelted several times, reaching higher purity with each repetition. Once the desired purity is reached, the large cylindrical ingot can then be cut, rolled, or drawn into the desired format. However, care is taken throughout this process and during further fabrication to avoid reintroducing contaminants into the niobium.

High purity niobium, often referred to as *RRR grade*, with $RRR > 260$ [37] is commonly used to provide good cavity performance. A lower grade of niobium, known as *reactor grade*, can have *RRR* values in the range of 30 to 100, usually due to fewer remelting steps being performed. This grade of niobium is sometimes used in cavity production or used for cavity parts that see low fields and RF losses such as beam pipes. Both of these materials are generally within the clean limit, meaning that although RRR grade niobium may have higher thermal conductivity, its BCS surface resistance is actually greater than for reactor grade.

As an alternative to bulk niobium, cavities may be fabricated with a thin layer, on the order of a few µm or less, of niobium sputtered on top of a copper substrate, as is commonly the case for CERN cavities [38] among others. The use of a thin layer of niobium on copper is an attractive approach as it aims for favourable properties in both the SRF surface resistance and thermal conductivity. The thin layer of niobium tends to have a purity with minimal BCS surface resistance, while the copper backing

provides its superior thermal conductivity. Disadvantages of this approach exist, such as difficulties in achieving a good quality coating and limited post-processing steps that may be applied as these can remove or damage the thin layer.

## 3.5 RF Power

The power that drives RF cavities is supplied by RF power sources such as Klystrons or solid state amplifiers. The RF power is transported from the source to the cavities via waveguides or coaxial transmission lines and is fed into the cavities through input couplers. These can be antennas inserted into the cavity or beam-pipe that couple to the electric field inside the cavity, or a loop that couples to the magnetic field.

The strength of this coupling can be described by the coupling factor, $\beta_i$, defined as the ratio of the intrinsic quality factor of the cavity to the external quality factor of the coupler $i$.

$$\beta_i = \frac{Q_0}{Q_{ext_i}} = \frac{P_{ext_i}}{P_c} \tag{3.25}$$

Overcoupling, when $\beta_i > 1$, implies that more power would leave the cavity through port $i$ than would be dissipated on the cavity walls, whereas under-coupling, $\beta_i < 1$, would be the opposite case. Matched or critical coupling implies equal power loss to the cavity walls and port $i$, so $\beta_i = 1$. Different operating conditions benefit from different coupling conditions, but SRF cavities are generally operated on the beam line in a heavily overcoupled state. Since the input coupler is generally the most significant coupler, the subscript is usually dropped and is referred to as simply $\beta$.

Power supplied to the cavity from the power source is referred to as the *forward* or *generator* power, labelled $P_g$ for this analysis. Some power is delivered into the cavity, while the remainder is reflected, a quantity labelled $P_r$. The reflection coefficient, $\Gamma = \sqrt{P_r/P_g}$, can be related to the coupling factor by

$$\Gamma = \frac{1-\beta}{1+\beta}. \tag{3.26}$$

The power that reaches the cavity is the difference between the forward and reverse powers. The power dissipated on the cavity surface can then be related to the reflection coefficient by:

$$P_c = P_g - P_r = P_g(1 - \Gamma^2). \tag{3.27}$$

As power builds up the fields within the cavity, it is either transferred to the beam, dissipated on the cavity walls, or transmitted to other external losses.

### 3.5.1 Generator Induced Voltage

Using Equations (3.13), (3.26), and (3.27), the deflecting voltage built up inside an RF deflecting cavity with shunt impedance $R_\perp$ from a generator supplying RF power $P_g$ at the resonant frequency of the cavity is

$$V_{gr} = \frac{2\sqrt{\beta}}{1+\beta}\sqrt{R_\perp P_g}. \tag{3.28}$$

If the cavity is driven at a frequency that differs from the resonant frequency of the cavity, the voltage induced in the cavity will be lower than calculated by (3.28). The cavity frequency may differ from the drive frequency due to local mechanical vibrations (microphonics), fluctuations in the pressure of the helium bath, the force exerted on the cavity walls from the electromagnetic fields within the cavity (Lorentz force detuning), or by a deliberate shift in cavity frequency. This detuning of the resonant frequency results in the cavity being driven off resonance, resulting in a reduced generator induced voltage within the cavity, given by

$$V_g = V_{gr} \cos\psi e^{i\psi}, \tag{3.29}$$

where the amplitude is decreased and a phase shift introduced, given by the detuning angle $\psi$ which is defined using the amount of frequency detuning, $\Delta\omega$, as

$$\tan\psi = -2Q_L\frac{\Delta\omega}{\omega}. \tag{3.30}$$

In general, this means that driving a detuned cavity requires more power to provide stable voltage and phase.

### 3.5.2 Beam Loading

Beam loading occurs when the beam gains or loses energy when passing through the cavity by coupling to the longitudinal electric field and transferring energy to or from the cavity. In a deflecting mode, the longitudinal electric field is zero on the cavity

axis, so there is nominally no beam loading. However, the longitudinal field increases as the distance off axis increases, and therefore a beam passing through the cavity off axis would see a longitudinal component to the electric field and hence, could contribute to beam loading of the cavity.

For a cavity with a horizontal deflecting mode, the deflection voltage can be determined from the longitudinal electric field using the Panofsky-Wenzel theorem [28], which states

$$V_\perp = -\frac{i}{k}\int_{-\infty}^{+\infty}\frac{\partial}{\partial x}\left(E_z\right)dz, \tag{3.31}$$

where $k$ is the wavenumber, $k = \omega/c$. Manipulating this gives

$$V_\perp = -\frac{i}{k}\frac{\partial}{\partial x}\left(\int E_z dz\right) = -\frac{i}{k}\frac{\partial V_z}{\partial x}. \tag{3.32}$$

If $V_z$ is the accelerating voltage integrated on a line offset from the axis by small distance $\Delta x$, then $\partial V_z/\partial x$ can be approximated by $V_z/\Delta x$. Solving (3.32) for $V_z$ gives the voltage that would be gained (or lost) by an off-axis particle passing through a deflecting cavity, with deflecting voltage $V_\perp$.

$$V_z = iV_\perp k\Delta x \tag{3.33}$$

Now, if a bunch with charge $q_b$ passes through a cavity, on a line offset by $\Delta x$ from the cavity axis, it will couple to the longitudinal electric field and induce a voltage in the cavity of

$$V_{z,q} = -2k_d q_b, \tag{3.34}$$

where $k_d$ is the dipole loss factor defined as $k_d = (k\Delta x)^2\frac{\omega}{4}\frac{R_\perp}{Q_0}$ [34].

Combining (3.33) and (3.34), the deflecting voltage induced in the cavity by an off-axis bunch would then be

$$V_{\perp,q} = -i\frac{\omega}{2}\frac{R_\perp}{Q_0}q_b k\Delta x. \tag{3.35}$$

A beam made up of a series of bunches with charge $q_b$ and bunch spacing $T_b$ would have a resulting beam current of $I_0 = q_b/T_b$. As each bunch passes through the cavity, it induces a voltage $V_{\perp,q}$ that decays with a decay constant $\tau = 2Q_L/\omega = 2Q_0/\omega(1+\beta)$. As the train of bunches pass by, the induced voltages add up as

$$V_\perp = V_{\perp,q} + V_{\perp,q}e^{-Tb/\tau} + V_{\perp,q}e^{-2Tb/\tau} + \dots \tag{3.36}$$

$$= \sum_{n=0}^{\infty} V_{\perp,q}e^{-nT_b/\tau}. \tag{3.37}$$

If the bunch spacing is shorter than the damping time, $T_b < \tau$, this sum converges to

$$V_\perp = V_{\perp,q}\frac{\tau}{T_b}. \tag{3.38}$$

Using (3.35) and after some manipulation of (3.38), the cavity deflecting voltage induced by the beam is then

$$V_{br} = -i\frac{I_0 R_\perp}{1+\beta}k\Delta x. \tag{3.39}$$

The factor of $i$ in this equation indicates that the beam driven deflecting voltage is induced at a phase of 90° from the bunch phase. If the cavity's resonant frequency is detuned from a harmonic of the bunch repetition rate, the cavity will be driven off resonance, and as before, this would result in a lower induced cavity voltage.

$$V_b = V_{br}\cos\psi e^{i\psi} \tag{3.40}$$

### 3.5.3 Separator Cavity Voltage in Steady State

The generator and beam induced voltages add together to give the total voltage present in the cavity. Due to the principle of superposition, these voltages add linearly, taking into account the relative phase and amplitudes. In phasor notation, this can be written as

$$\tilde{V_c} = \tilde{V_g} + \tilde{V_b}, \tag{3.41}$$

where the voltages present in the cavity are represented by phasers that rotate counter clockwise in the complex plane at frequency $\omega$. The projection of the phasor on the real axis gives the voltage present in the cavity as a function of time, resulting in the expected sinusoidally varying voltage. The phasor for the cavity voltage, $\tilde{V_c}$, with maximum voltage $V_c$ and relative phase $\phi$, is given by

$$\tilde{V}_c = V_c e^{i(\omega t+\phi)}. \tag{3.42}$$

More conveniently for this analysis, we can define the phasors within a frame that rotates counter clockwise at an angular frequency $\omega$ such that the phasor becomes fixed in time in the new frame

$$\tilde{V}_c = V_c e^{i\phi}. \tag{3.43}$$

Note that although a new notation was not introduced for phasors in this new reference frame, all phasors referred to from this point onwards exist within the rotating frame.

A phasor diagram can be used to determine the required generator power to achieve the desired cavity voltage with beam loading. The real axis of the phasor diagram is aligned with the phasor for the beam current so that the phase of the cavity voltage is defined such that when $\phi = 0$, the deflecting voltage in the cavity is maximal. The phasor for the beam loading induced voltage can be added, then the generator voltage is determined using Equation (3.41). This is shown in Figure 3.3 for a simple general case with cavity detuning.

For a cavity voltage in the deflecting phase, the required $V_\perp$ sits on the positive real axis at $\phi = 0°$. As an off-axis bunch passes and couples to the longitudinal field, it will drive the deflecting field at -90° phase, so on the imaginary axis, as described by Equation (3.39). Due to cavity detuning, the true induced cavity voltage will lag behind by the detuning angle $\psi$.

The required induced generator voltage will provide the deflecting voltage in the cavity when vector summed with the beam loading voltage $V_b$, as per Equation (3.41). After some manipulation starting with Equations (3.28) and (3.41), the generator voltage can be determined and the generator power required from the input RF power source can be shown to be equal to

$$P_g = \frac{V_\perp^2}{{}^{R_\perp}\!/_Q Q_0}\frac{1}{4\beta}\left\{\left[1+\beta+\frac{{}^{R_\perp}\!/_Q Q_0 I_0}{V_\perp}k\Delta x\cos\phi\right]^2 + \right. \\ \left. + \left[(1+\beta)\tan\psi - \frac{{}^{R_\perp}\!/_Q Q_0 I_0}{V_\perp}k\Delta x\sin\phi\right]^2\right\} \tag{3.44}$$

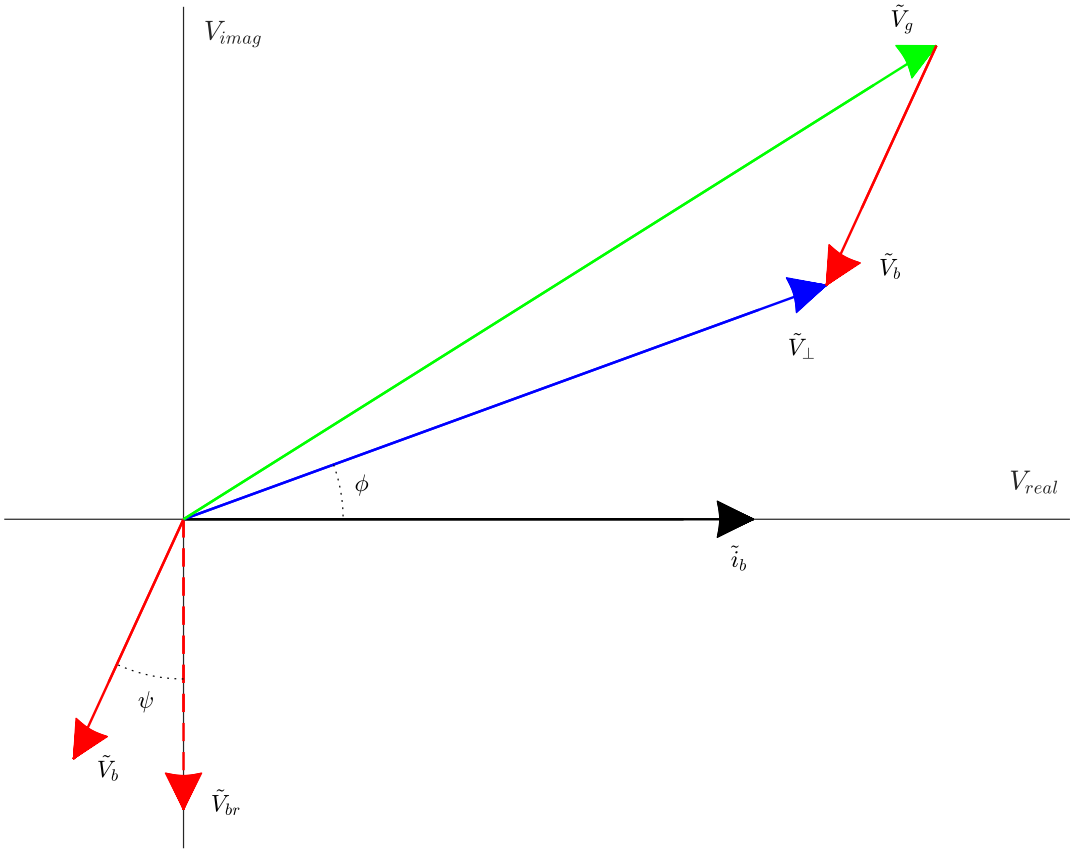


Figure 3.3: The vector diagram showing the sum of generator and beam loading induced voltages, $V_g$ and $V_b$, to produce the resultant deflecting voltage present in the cavity, $V_\perp$. The beam current phasor is plotted on the same axis to indicate its relative phase.

for the case of a beam with a single bunch phase in reference to the cavity voltage.

This formula can be used to determine the optimal input coupling factor, $\beta$, and the required power that must be supplied by the RF power source in order to reach the required cavity voltage. This will be calculated for the ARIEL separator cavity in Section 4.5.1. Beam loading in the ARIEL e-Linac is complicated by the fact that three sets of bunches will be passing through the cavity at different phases and beam currents, each contributing to the beam loading of the cavity.

The two terms added in quadrature in Equation (3.44) describe two ways that the beam couples to the mode. The first term, containing $\cos\phi$, represents active beam loading. Energy can be transfered between the beam and cavity through this term. The beam experiences maximal active beam loading in the zero crossing phase, where

$\phi$ is 90° or 270°. The second term represents the reactive beam loading, that takes place in the phase which cannot transfer energy to the beam.

These two terms can be understood through the mechanism of the beam coupling to the fields within the cavity through the longitudinal electric field. In the zero crossing phase, the off-axis longitudinal field is in a phase such that its integral over a bunch's trajectory is non-zero. This means that voltage induced in the cavity by active beam loading will directly add to or subtract from the cavity voltage, as can be seen on a vector diagram with the beam loading phasor aligned with the cavity voltage.

The reactive component however takes place in the phase where the integral of the longitudinal field over the first half of the trajectory through the cavity is cancelled by the second half. So, nominally, energy is not being transferred between the beam and cavity for a purely reactive beam, but the beam acts to alter the phase of the fields within the cavity. Vector diagrams of beams in pure active and reactive beam loading phases are shown in Figure 3.4.

Finally, due to the inclusion of a term related to detuning in the reactive side of Equation (3.44), reactive beam loading may be compensated by the appropriate selection of the detuning phase $\psi$, such that

$$(1+\beta)\tan\psi = \frac{{}^{R_\perp}/_{Q}Q_0 I_0}{V_\perp}\sin\phi. \tag{3.45}$$

This would correspond to detuning the cavity, and driving the cavity at a frequency that differs from its resonant frequency by an amount defined by Equation (3.30).

## 3.6 Higher Order Modes

As the beam passes though the cavity, it can excite other resonant modes that can exist within the cavity. As with the operating mode, this can happen when the beam couples to a longitudinal field component along the path of the beam, transferring energy between the beam and the mode. These modes can have detrimental effects on the beam and can lead to large amounts of power being dissipated within the cavity.

The HOMs will be categorized depending on their field orientations as either deflecting modes in the horizontal or vertical direction, or as accelerating modes. Deflecting modes have no longitudinal electric field on-axis and require an offset from the beam axis in order to excite the mode. Accelerating modes have a longitudinal

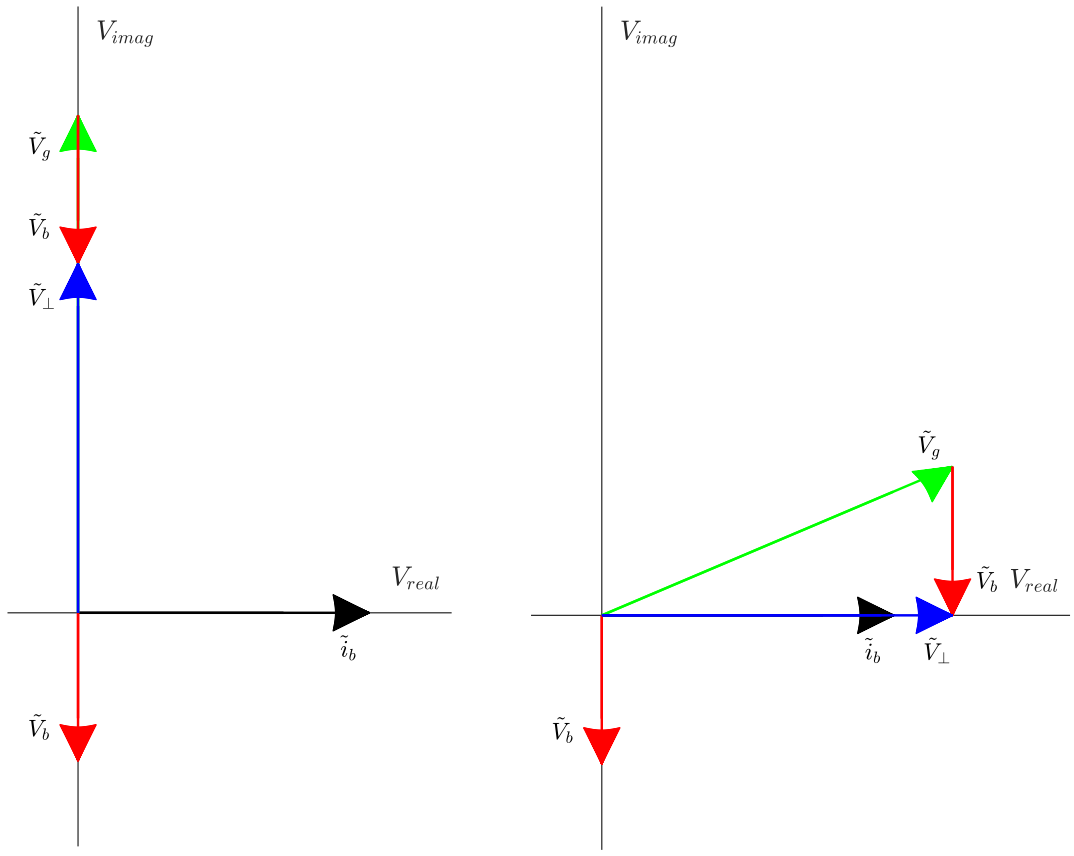


Figure 3.4: Vector diagrams for the case of a) pure active beam loading from a beam passing through the cavity in the zero crossing phase, and b) pure reactive beam loading.

electric field that can couple strongly to the beam and can result in the dissipation of large amounts of energy into the cavity.

The strength of the HOMs are characterized by their geometric shunt impedance, which as before, describes how efficiently the cavity may transfer energy between the cavity and the beam. The $R/Q$ of deflecting and accelerating modes can be determined by integration of the fields along the beam axis as

$$R_\perp/Q = \frac{\left| \int_{-L/2}^{+L/2} \left[ \vec{E}_\perp(z) + i(\vec{v} \times \vec{B}_\perp(z)) \right] e^{\frac{i\omega z}{c}} dz \right|^2}{\omega U}, \tag{3.46}$$

$$R_{acc}/Q = \frac{\left|\int_{-L/2}^{+L/2} E_z(z) e^{\frac{i\omega z}{c}} dz\right|^2}{\omega U}. \tag{3.47}$$

The HOM fields excited by the beam can interact with subsequent particles causing instabilities, loss of beam, and energy to be deposited in the cavity. In order to limit these processes, the HOMs can be damped or the mode frequencies controlled to avoid resonant build up of the field amplitude induced by the beam. Damping is achieved by increasing the loaded $Q$ of the mode by adding couplers or dampers that couple to the modes and remove their energy. A thorough analysis of the HOMs present in a cavity is required to identify the $R/Q$ and $Q_L$ of all modes to ensure sufficient damping.

Some of the important ways that the beam and cavity can interact are described next. Some numbers have been inserted from the ARIEL separator cavity to quantify the importance of each effect.

### Single Bunch Effects

These are interactions in which the fields excited by the head of a bunch perturb the electrons in the tail of the same bunch causing a disturbance across the bunch. Deflecting HOMs can cause transverse deflections of the tail of a bunch relative to the head that intensify along the length of the linac. This growth is generally quantified by a transverse growth parameter that describes the relative oscillation amplitude of the tail relative to the head due to betatron motion along the linac. The growth parameter, calculated from a two-particle model [39], is

$$\Upsilon = -\frac{{}^{q_b}\!/_{e} r_0 W_1(z) L_0}{4 k_\beta \gamma L_c}. \tag{3.48}$$

where $r_0$ is the classical electron radius, $W_1(z)$ is the transverse wake function at the back of the bunch, $L_c$ is the cavity length, while $L_0$ is the total linac length. $k_\beta$ is the betatron wave number that describes the periodic transverse oscillation of the bunch about the reference trajectory. Using typical numbers again, including a value on the order of $-1\,\mathrm{cm}^{-2}$ for the wakefield term, $W_1(z)$, the growth parameter is also much less than one, meaning the tail of the bunch follows along the same path as the head.

Single bunch effects from HOMs are not a concern for the separator cavity. This is as expected since these effects tend to be more significant for linacs comprised of many multicell cavities that make up a significant fraction of the length of a linac.

### Multipass Beam Break Up

In an accelerator where the beam makes multiple passes through the same cavity, a process called multipass beam breakup (BBU) can destroy the beam quality. On its first pass through the cavity, a bunch may receive an undesired transverse deflection from an excited HOM. If the bunch returns to the cavity with the correct phase and transverse displacement, it can drive more energy into the mode, increasing the mode intensity and deflections of subsequent bunches. If the beam current is high enough this feedback can lead to an exponential growth of the HOM amplitude and loss of beam.

The formula for the threshold current, $I_{th}$, at which exponential growth of the $m$-th deflecting HOM can occur is given by

$$I_{th} = -\frac{2E}{{}^{R_m}\!/_{Q} Q_L e c \omega_m M_{ij} \sin(\omega_m t_r)} \tag{3.49}$$

where $t_r$ is the recirculation time between passes of the cavity and $M_{ij}$ is the transfer matrix element that defines the transverse offset on the second pass that occurs from an angular deflection on the first pass.

The maximum recirculated beam current in the e-Linac will be 20 mA in an ERL-only mode of operation, requiring the BBU threshold current to be greater than 20 mA. The optics of the recirculation loop are not yet fully defined, so taking a worst case scenario of $\sin(\omega t_r) = 1$ and $M_{ij} \cong 10\,\mathrm{m}$[2], the maximum $R/Q \cdot Q_L$ for deflecting modes is approximately 8 MΩ for HOMs at 3 GHz and 20 MΩ at 1 GHz. For extra precaution, a safety factor of 10 will be applied such that all transverse modes should have goal of $R/Q \cdot Q_L \lesssim 1\,\mathrm{M}\Omega$.

### Power Dissipated by the Beam

Another consideration is the power transferred to the cavity by the beam when HOMs are excited. The amount of energy dissipated by the beam depends on the current, $R/Q \cdot Q_L$ of the mode, and the timing of the bunches with respect to the frequency of the HOM. Modes that are resonant with the bunch frequency are capable of dissipating large amounts of power whereas modes off resonance dissipate little power, generally $<<$ 1 W. The bandwidth of a mode is given by $f_m/Q_L$ and therefore is usually very narrow for SRF cavities.

[2] this corresponds to a 1 mrad deflection resulting in a 10mm offset of the beam

The beam structure of the interleaved beams is not a simple repetitive bunch structure, but rather the two frequencies overlaid. The ERL frequency has not yet been fixed, but will be less than 650 MHz to allow for a higher bunch charge. This frequency must satisfy 650 MHz/$n$, where $n$ is an integer, in order to be compatible with the accelerating and separator cavities' RF. HOM frequencies in resonance with either 650 MHz or the lower ERL frequency need be avoided.

The power dissipated by an accelerating mode on resonance with the bunch frequency is

$$P_b = I_0^2 \frac{R_{acc}}{Q} Q_L. \tag{3.50}$$

So for ${}^{R_{acc}}/_{Q} \cdot Q_L$ of about $10^6\,\Omega$, the beam can dissipate 100's of Watts into a resonant accelerating HOM. Figure 3.5 shows the power that would be dissipated by an accelerating mode with a shunt impedance of $10^6\,\Omega$ as a function of the mode frequency for a 10 mA beam to ARIEL and a 6 mA ERL beam at 130 MHz. The modulation of the peak power that may be dissipated on resonance depends on the relative phases of the 3 interleaved beams. If a HOM frequency is resonant with all three beams, maximal power may be driven into the mode. Conversely, if the frequency is resonant with multiple beams but they arrive in the cavity at different phases, they will counteract each other, resulting in less power becoming coupled to the mode.

The power that may be dissipated from deflecting modes depends on the transverse beam offset in the cavity. Therefore, the peak power dissipated from a resonant mode has a factor of $(\Delta x\,\omega_m/c)^2$ multiplying Equation (3.50). This decreases the maximum power dissipated by deflecting modes by a factor of $\sim 100$ from accelerating modes for typical transverse deflections.

### Summary

The limiting HOM effect for transverse deflecting modes is multipass BBU, putting an ultimate limit on $R_\perp/Q \cdot Q_L$ of less than $\sim 10\,\mathrm{M}\Omega$, with a goal of less than $\sim 1\,\mathrm{M}\Omega$. Very little power is expected to be coupled from deflecting HOMs and dissipated within the cavity.

For accelerating modes, the main concern is power being dissipated by the beam into resonant HOMs. This can be limited in two ways: avoiding HOM frequencies resonant with the bunch frequencies, or restricting $R_\perp/Q \cdot Q_L$ to less than $1 \times 10^5\,\Omega$,

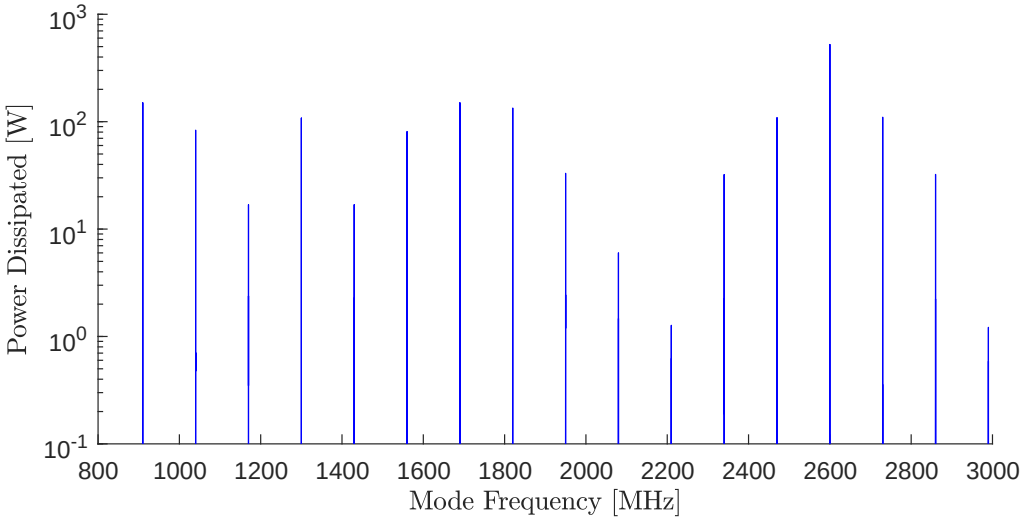


Figure 3.5: The frequency dependence of the power that would be dissipated in a accelerating HOM with ${}^{R_{acc}}/_{Q} \cdot Q_L = 10^6\,\Omega$, for a 10 mA ARIEL beam and a 6 mA recirculating beam at 130 MHz.

limiting the dissipated power to up to 40 W for a HOM resonant with 20 mA of beam current.

# Chapter 4

# Cavity Design

A deflecting mode cavity operating in CW at 650 MHz is required to initiate the separation of the interleaved ARIEL and ERL bound beams. This chapter introduces a selection of deflecting mode cavities that have been developed for use in various accelerator projects over the last 60 years. This is followed by a summary of the development of a separator cavity design for the ARIEL e-Linac. Considerations regarding the cavity's shape, mechanical design, input and HOM coupling, and thermal behaviour of the cavity are all summarized.

## 4.1 Historical Development of Deflecting Cavities

Deflecting mode cavities have been used in particle accelerators since the early 1960's for many purposes including beam diagnostics, increasing luminosity of colliding beams, compressing bunches, and separating particle beams. A brief history will be provided of the development and varied applications of this type of cavity. This is not meant to be an exhaustive list of all deflecting cavities developed, but is intended to introduce the wide variability of designs and applications of this technology.

### 4.1.1 TM Mode Cavities

#### Early Development

The first deflecting cavity built and tested on a particle beam was constructed at Stanford in 1960 and tested on a 150 MeV electron beam [40]. This cavity was a normal conducting device, with a single rectangular shaped cell operating in the

$TM_{012}$ mode at 2.856 GHz. The losses on this structure where quite high, dissipating up to 1.3 MW of power to reach a deflecting voltage of about 0.8 MV. It was therefore operated with a duty factor of 0.06% to limit the average power dissipation on the structure.

Soon after this initial cavity, long multi-cell structures were being developed at CERN, SLAC, and BNL [41, 42, 43]. These were 2.855 GHz travelling wave structures built with over 100 individual cells brazed together. Again, since these were normal conducting devices, large power dissipation limited their operation to low duty factors. An early use of these cavities was as particle mass separators, where they were operated in pairs to give varying transverse momentum to particles of different masses, allowing for the detection and differentiation of different particle species making up a single beam.

In order to impart higher transverse deflections and at longer duty factors, CERN and the Karlsruhe Institute of Technology collaborated to develop one of the first superconducting niobium deflecting cavities ever built for use as a particle mass separator at CERN [44]. As a superconducting device, the dissipated power was decreased from megawatts in room temperature devices to only 7 W of power, dissipated at the bath temperature of 1.8 K, and reaching a mean deflecting voltage of $\sim 3.3$ MV. The cavity operated at roughly the same frequency as the previous normal conducting multi-cell designs, utilizing 104 elliptical shaped cells machined from solid niobium. The operating mode was a standing wave, $TM_{110}$ mode, rather than a travelling wave mode as the previous cavities employed.

Modern versions of these long multicell deflecting mode cavities are still in use today at many labs, such as the XTCAV at LCLS [45]. This is an X-band (11.4 GHz) travelling wave TM mode cavity, with 113 cells per structure and roughly 1 m long. It can provide a 48 MV transverse kick, but since it is a normal conducting structure, is operated in pulsed mode only and requires 40 MW of input power.

Rather than being used to mass separate particle beams, these types of structures are more commonly used these days for diagnostic purposes by correlating longitudinal position within the bunch to a transverse momentum. Rotation of a bunch is achieved by passing the beam through the cavity at the zero crossing, such that the head of the bunch receives transverse momentum in the opposite direction to particles in the tail. Viewing the transverse distribution of the beam at a downstream location would then provide longitudinal information from the beam, based on a transverse coordinate.

### Single Cell TM Mode Structure

Single cell cavities have also been developed, such as the KEKB crab cavities [46], which are the only crab cavities operated to date in a particle accelerator. Crab cavities are used in colliding beam experiments to impart a time varying transverse momentum across the length of bunches before they reach the interaction point. This rotates the bunches, as shown in Figure 4.1, compensating for the crossing angle of the two beams, and resulting in increased luminosity (i.e. a higher rate of collisions). Bunches in the colliding beams are rotated by passing through cavities located in both beam lines before the interaction point, and then rotated back by a second set after the collision point.

The KEKB cavities are elliptical shaped cavities operating at 508.9 MHz. They are axially asymmetric, with larger height than width. The conceptual design of these cavities is shown in Figure 4.1. The operating mode is a standing wave $TM_{110}$ mode, where the deflection is imparted by an on axis transverse magnetic field. In an axially symmetric cavity, this mode can take on any azimuthal orientation. The non-axial symmetry of this cavity fixes the orientation of the fields by causing a splitting of the mode into two modes with horizontal and vertical polarizations at different frequencies. The desired horizontal crabbing mode has the lower frequency of the two.

In addition to the HOMs, the cavity also supports a lower order $TM_{010}$ accelerating mode. Damping of these modes is achieved through two methods. On one side of the cavity, a resistive material in the beam pipe damps the modes that are above the cutoff frequency of the beam pipe, including the higher order vertical crabbing mode. On the other side of the cavity, a coaxial coupler was developed, consisting of a tube inserted coaxially into the beam pipe and extending slightly into the cavity. This coupler provides strong coupling to the LOM and other HOMs, directing them to an RF absorber outside of the cavity. A notch filter built into the coupler is used to reject the operating mode from coupling to the coaxial coupler.

The KEKB crab cavities operate at deflecting voltages of over 1.4 MV in the KEKB electron-positron collider at a frequency of 508.9 MHz. At this frequency, the TM mode cavity has large transverse dimensions with a height of 866 mm and a width of 483 mm. Due to the long coaxial coupler in the beam pipe, the length of the cavity is also quite long, with a length of about 1.5 m.

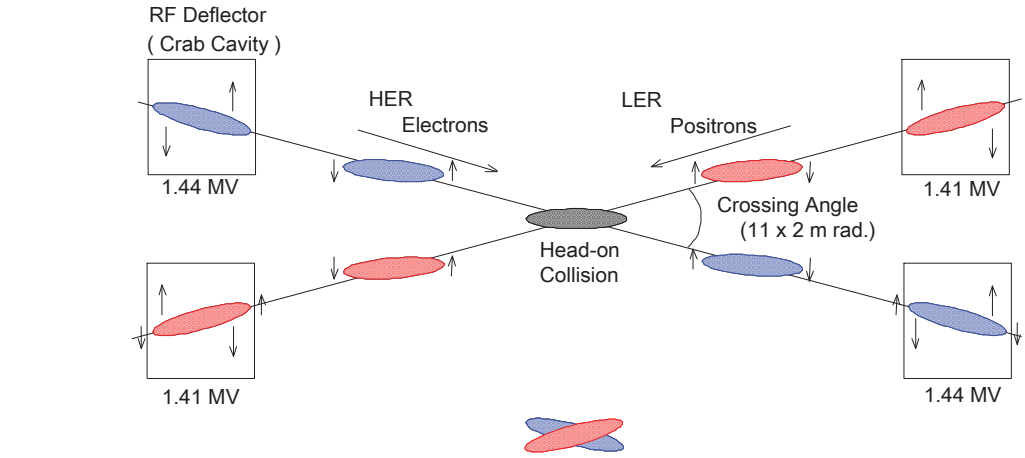


(a)

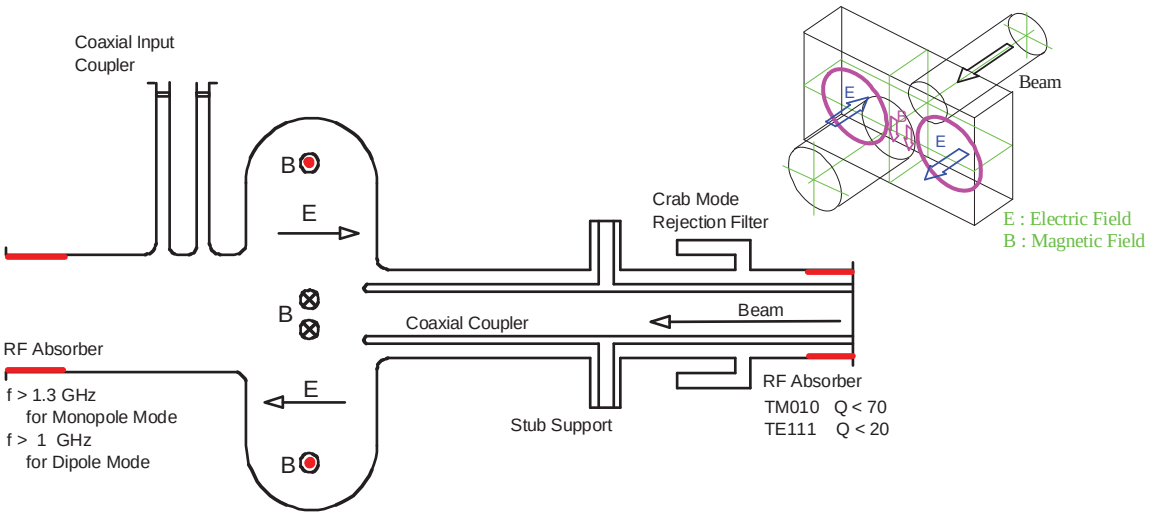


(b)

Figure 4.1: a) The crab crossing scheme in use at the KEKB electron positron collider. b) The conceptual design of the KEKB crab cavities. Images reproduced from [47] with permission from the author.

### 4.1.2 Non-TM Mode Cavities

TM mode cavities are convenient for high frequency applications, but as seen with the KEKB crab cavity, require large transverse dimensions at lower frequencies. Cavities that operate in TE-like or TEM-like modes tend to have smaller dimensions than TM mode cavities of the same frequency. Additionally, TEM mode cavities can have higher shunt impedance, leading to more efficient transfer of voltage from cavity to beam.

### CEBAF Separator Cavity

The first deflecting mode cavity to employ a TEM mode was the CEBAF deflector cavity, developed at CEBAF in the 1990's [1]. This cavity operates at a frequency of 499 MHz and has a diameter of about 300 mm. This is about a third of the height of the KEKB crab cavity that operates at a similar frequency. These cavities are used in the horizontal and vertical separator systems of the extraction system in the CEBAF recirculating electron accelerator. The 1497 MHz beam can be split into either two or three directions by a 499 MHz cavity operating at different phases, as depicted in Figure 4.2.

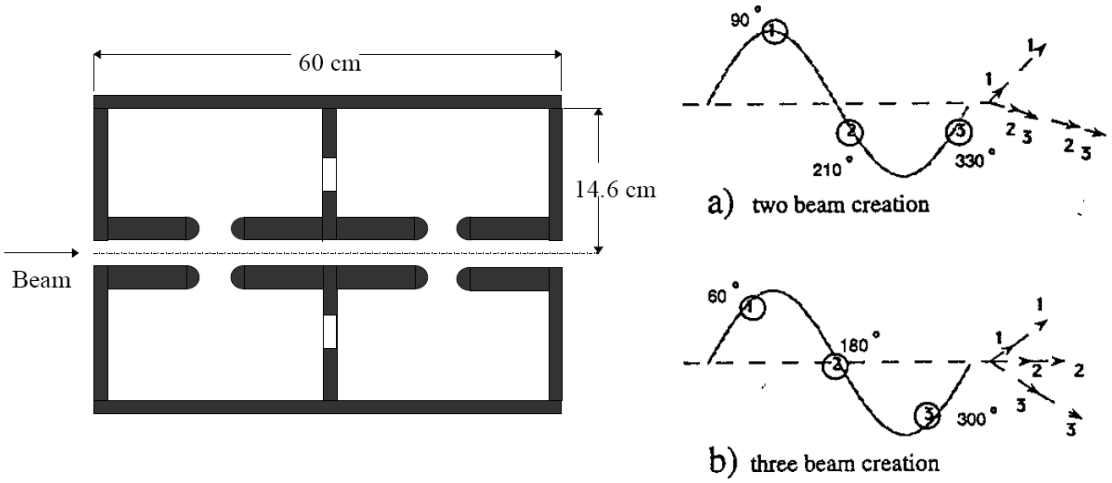


Figure 4.2: a) The CEBAF separator cavity and b) the creation of two and three beams using the RF separator. Images reproduced from [48] with permission from the author.

The cavity is a normal conducting cavity with two cells. Each cell has a cylindrical shape with two rods running parallel to the beam axis on either end of the cells, as shown in Figure 4.2. The cavity supports a mode with an electric field oscillating between two adjacent, parallel rods, in opposite phase on either side of the cell, and magnetic fields that circulate around the rods. The net result of this field pattern is a transverse deflection of a passing beam in the plane of the two rods.

The geometry of the CEBAF separator cavity has since been modified and improved upon for better shunt impedance and lower peak fields for use in the Cornell ERL Injector [49]. The ARIEL e-Linac employs a similar version of the Cornell cavity in the low energy diagnostics beam line, operating at 1.3 GHz, shown in Figure 4.3.

In this cavity, the rods have been modified from simple cylinders, to a shape that curves around the beam axis, increasing the on axis fields, as well as the uniformity of the fields across the transverse aperture. Bunches pass through the cavity in the zero-crossing phase for use as a longitudinal diagnostics device [50].

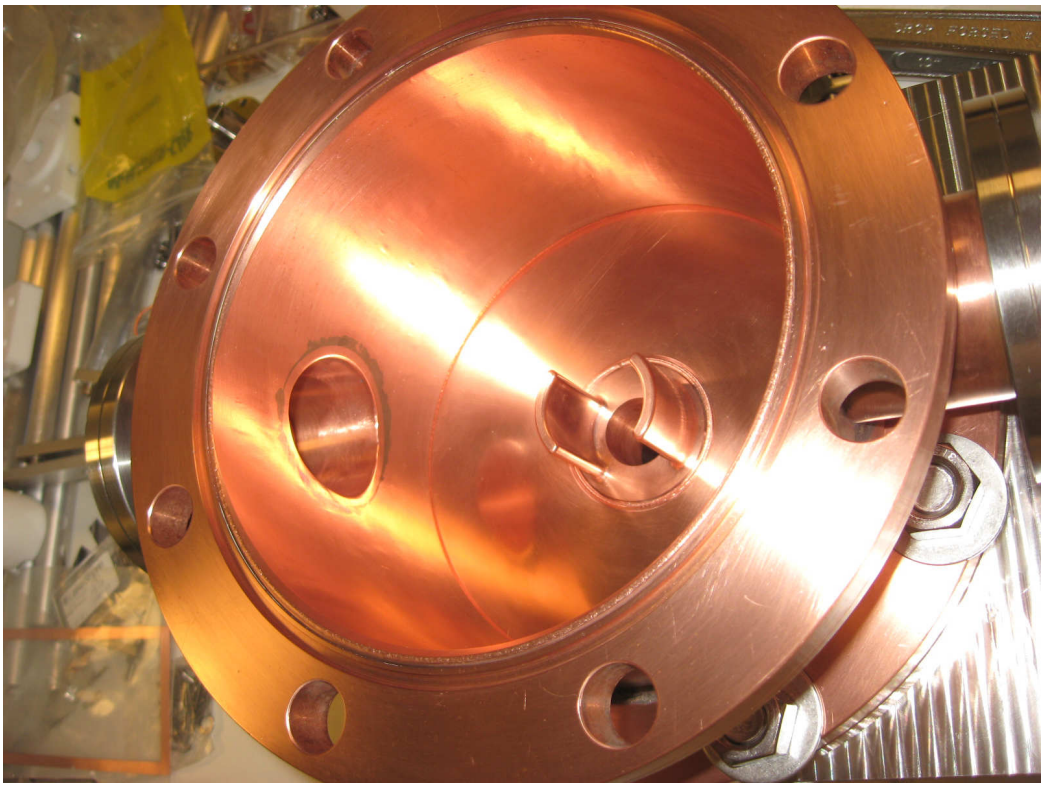

Figure 4.3: The inside of the normal conducting ARIEL diagnostics deflector cavity. The rods, or nose cones, can be seen on end plate of the cavity around the beam pipe.

### HL-LHC Crab Cavities

The upcoming Hi-Luminosity Large Hadron Collider (HL-LCH) upgrade will employ the use of crab cavities at the two high luminosity interaction points feeding the ATLAS and CMS experiments at CERN. With the addition of other hardware modifications, the upgrade is planned to increase the luminosity by a factor of 10 [51]. As discussed earlier, crab cavities rotate bunches to achieve more effective interaction between colliding beams.

To achieve the required crabbing angle for beam energies of up to 7 TeV, multiple cavities are required for each beam to provide a total of 10 MV deflecting voltage [2]. Crab cavities will be placed along both beam lines and on either side of the two

interaction points. The second set of crab cavities is required to remove the imparted rotation of the bunches so that they may continue to recirculate around the ring without excess beam loss. In total, the LHC luminosity upgrade requires 16 cavities, each operating in CW at a design deflecting voltage of 3.3 MV.

The space requirements on the cavities are very restraining due to the positioning of the two beam pipes. The counter-rotating beams are contained in adjacent beam pipes that are separated by less than 200 mm. A very compact geometry crab cavity is then required to act on one beam while clearing the adjacent beam pipe. A worldwide design effort has produced numerous novel conceptual designs for compact, low frequency, superconducting deflecting cavities. Three of these designs, shown in Figure 4.4, were selected for further study and prototyping, all of them operating in non-TM modes.

The first cavity type pictured here is referred to as the RF Dipole (RFD) cavity that was jointly developed by Old Dominion University and SLAC [3, 55]. The main feature of this geometry is two inward facing ridges located on the plane of the desired deflection. The deflecting mode is a TE-like mode, with the main deflection force imparted by an electric field between the two ridges. The magnetic field circulates around the ridges, resulting in a force in the opposite direction to the electric field.

The geometry was optimized to maximize the deflecting field, while minimizing the surface electric and magnetic fields and the power dissipation. The operating mode of this cavity is the fundamental mode, with the nearest higher order mode separated by a large frequency, simplifying the damping of HOMs.

The next cavity is the Double Quarter Wave crab cavity (DQW), designed at BNL [53]. This cavity operates in a similar mode to the RF dipole, with a geometry consisting of two quarter wave resonators stacked together, resulting in a fundamental mode with a transverse electric field between the two inner conductors. Similar to the RF Dipole geometry, the nearest HOM is separated by about half the fundamental mode frequency. The geometry was optimized to minimize the on-axis accelerating field component and non-linearities of the deflecting voltage when offset from the beam axis of the cavity.

And finally, the third contender developed for the HL-LHC was a superconducting 4-rod crab cavity (4RCC) [56]. This geometry was modified from CEBAF's normal conducting deflector design for use at a lower frequency, with larger beam pipes, and much more compact outer dimensions, in addition to operating at 2 K. The rods of the 4RCC were modified from the simple cylindrical shape to a conical, non-circular

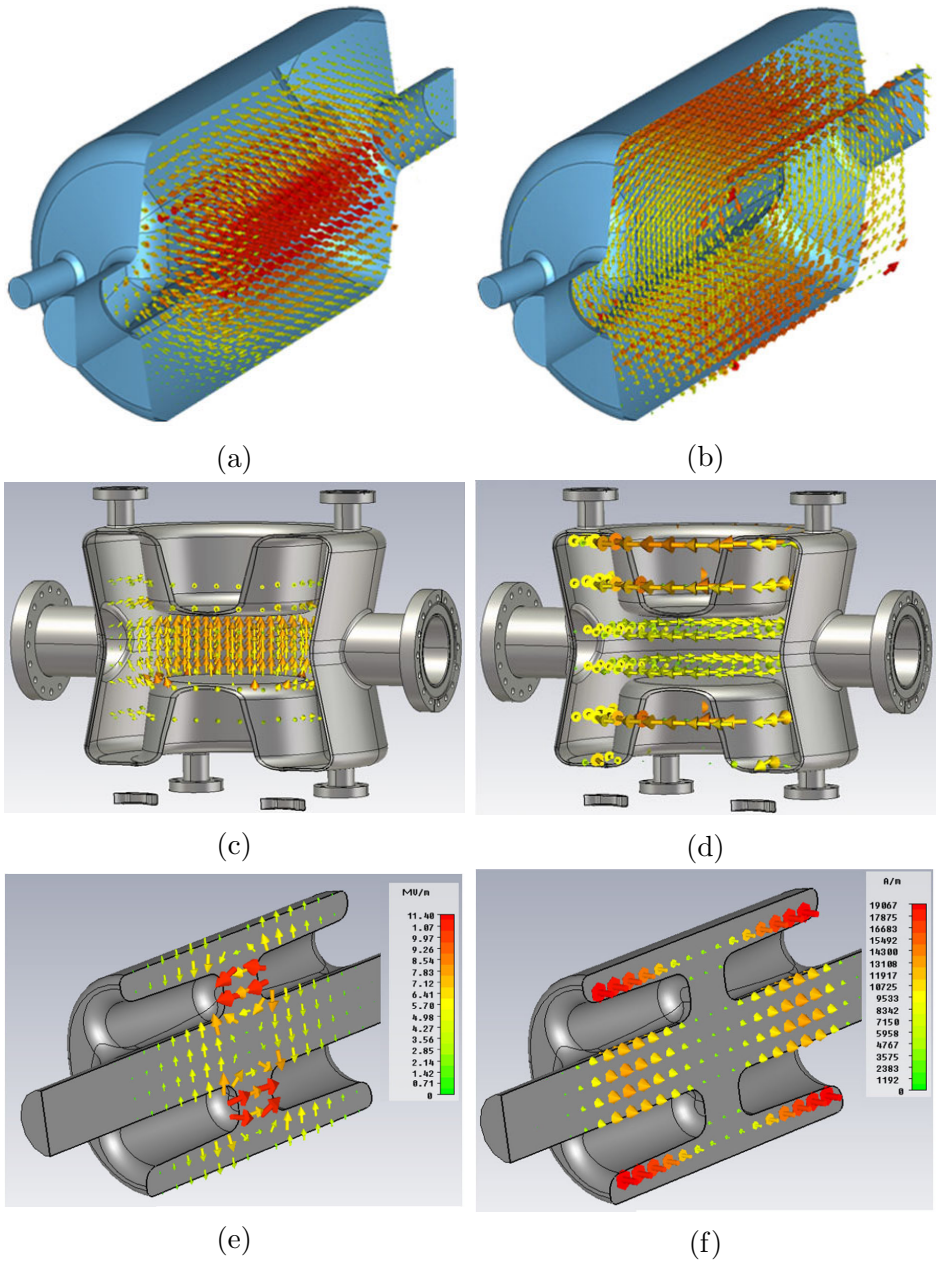


Figure 4.4: The three HL-LHC crab cavity prototypes. a) The electric and b) the magnetic fields in the RFD cavity operating mode [52], c) and d) the field's in the DQW cavity [53], and e) and f) the 4RCC [54]. In the orientations pictured, the RFD cavity would provide a horizontal deflection while the DQW and 4RCC would impart a vertical deflection. Images have been reproduced with permission from the authors.

cross-section to decrease the peak fields and to increase field uniformity across the aperture.

The 4RCC has a lower order mode very close to the operating mode frequency of the cavity, although this may be effectively damped due to the locations of the magnetic fields within the cavity. Additionally, two HOMs exist at frequencies near to the operating mode, with low shunt impedances.

Table 4.1: The RF properties of HL-LHC crab cavities and results of the cryogenic tests of the proof-of-principal cavities.

| Parameter | RFD [57] | DQW [58] | 4RCC [54] | Units |
|---|---|---|---|---|
| Design Frequency | 400 | 400 | 400 | MHz |
| Frequency of nearest mode | 590 | 570 | 371/439 | MHz |
| Transverse Dimension | 281 | 288 | 290 | mm |
| Shunt Impedance, $R_\perp/Q$ | 287 | 429 | 325 | Ω |
| Geometry Factor, $G$ | 107 | 87 | 53 | Ω |
| Peak electric field*, $E_p$ | 36.5 | 37 | 30.8 | MV/m |
| Peak magnetic field*, $B_p$ | 64 | 72 | 72.4 | mT |
| Max deflecting voltage at 2K | 7.0 | 5.8 | 3.3 | MV |

* at $V_\perp = 3.4\,\mathrm{MV}$

Proof of principle cavities have been built for all three cavity options and tested at 2 K, [52, 53, 54]. The RF properties are summarized in Table 4.1. All three cavities reached the design specification of 3.3 MV deflecting voltage, while the RFD cavity far surpassed the goal, reaching 7.0 MV before quenching, while the DQW cavity reached 5.8 MV. It was decided to continue pursuing the RFD and DQW cavities for further testing in the SPS beamline at CERN. Two of each cavity are being built and will be installed in cryomodules on the CERN's SPS beamline for commissioning starting in 2018.

## 4.2 Conceptual Design of the Separator Cavity

After throughly reviewing the historical development of deflecting mode cavities, it was decided to pursue a non TM-mode type cavity geometry to avoid large transverse dimensions of the cavity, and to take advantage of the design efforts toward the HL-LHC crab cavities. Due to the generally higher transverse shunt impedances achieved by non-TM mode cavities, this would also allow for reduced power requirements from

the cavity and more efficient operation.

The decision to pursue a superconducting design was made by considering the power that would be dissipated within a normal conducting cavity. Typical shunt impedances for large aperture non-TM mode geometries are typically in the range of several hundred Ω's, as seen in Table 4.1. A geometry optimized for operation as a normal conducting cavity can often reach higher shunt impedance than superconducting cavities since the peak surface magnetic field is not limited by the critical field. A deflecting cavity with a shunt impedance of ∼500 Ω, a geometry factor of about 100 Ω and operating at the upper end of the operating range being considered would dissipate roughly

$$P_c = \frac{V_\perp^2 R_s}{R_\perp/_Q G} \sim 50\,\mathrm{kW} \tag{4.1}$$

in a room temperature copper structure. This is a very large amount of power to dissipate in a cavity with approximate dimensions of half the RF wavelength, or about 0.2 m, when operating in CW. While it may be technically feasible to dissipate this scale of power load, it would constitute a significant engineering challenge. Alternatively, under the required operating conditions, a similar superconducting cavity could provide a deflecting voltage of up 0.6 MV in CW with less than 2 W at 4.2 K, a relatively low power dissipation for a superconducting cavity.

To further investigate the feasibility of a normal conducting cavity design, a parameter search was performed to find a rough optimization of the 4-Rod and RFD type geometries under normal conducting conditions. With a 50 mm beam pipe aperture, the lower limit to the dissipated power in either cavity geometry was determined to be 30–40 kW. This heat load would still be a technical challenge to effectively cool for the size of the cavity.

Furthermore, the peak surface power loss on the cavity walls would reach around 100 W/cm$^2$ in some areas, dissipated continuously as the cavity will be operated in CW. Typical surface power losses on normal conducting cavities are usually on the order of 10's of W/cm$^2$, with some references giving an upper range for water cooling of ∼110 W/cm$^2$ [59]. So while perhaps not technically infeasible, such a localized power load would provide a challenge beyond that normally applied to normal conducting cavity design. A possible 4-Rod type cavity geometry is shown in Figure 4.5, with a peak power dissipation near the root of the rods of over 100 W/cm$^2$.

For these reasons, and the fact that liquid helium services are already available

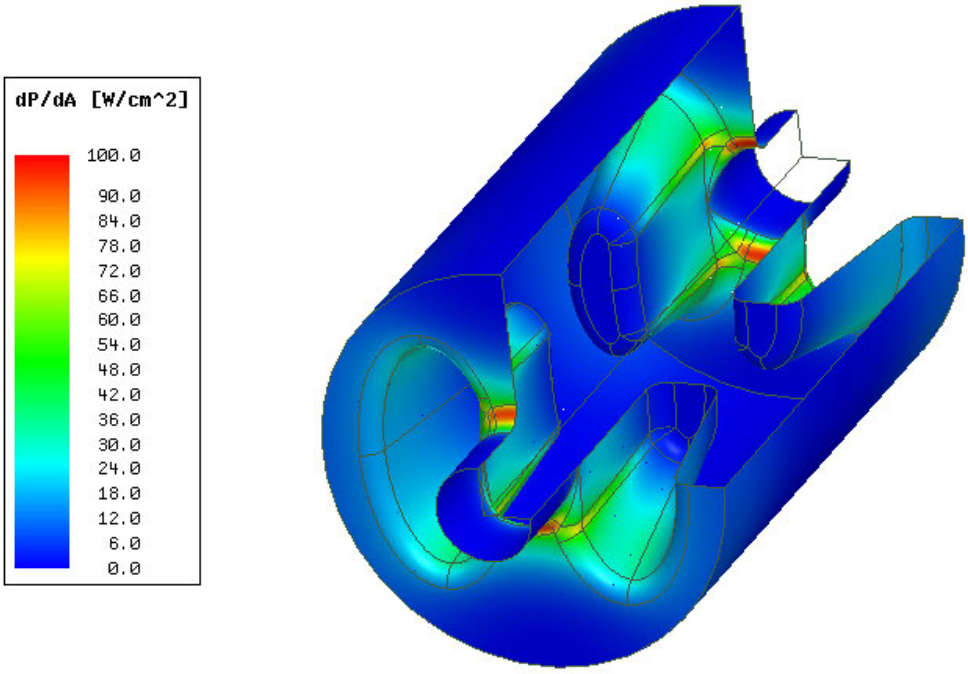


Figure 4.5: A possible NC cavity with the 4 Rod geometry, showing the RF power dissipated on the cavity surface, reaching over 100 $\mathrm{W/cm^2}$ at the root of the rods.

in the ARIEL electron hall for supplying the injector and accelerator cryomodules, a superconducting cavity has been developed to meet the needs of the ARIEL e-Linac. The relatively low deflecting voltage required from the separator cavity allowed for some flexibility in the design, allowing for a significant decrease of the cavity length, as well as investigations into non-standard fabrication techniques for building the cavity.

### 4.2.1 Superconducting Separator Cavity Geometry

Making use of the design effort toward the HL-LHC crab cavities, the geometry of the separator cavity for the ARIEL e-Linac was based on the RFD crab cavity design, which had been developed and parametrized in [55]. This cavity geometry was chosen due to its compact geometry with high net deflection and low peak surface fields. With the HOM damping requirements in mind, the absence of a lower order mode and the large separation between the operating mode and HOMs are key aspects of this geometry.

The main feature of this cavity geometry is the pair of ridges that face each

other along the deflecting plane of the cavity and generate an oscillating electric field between them in the cavity's fundamental mode. This field provides the main contribution to the transverse deflecting force. The magnetic field oscillates around the ridges, in an orientation such that the force generated by the magnetic field opposes the force from the electric field, but resulting in a net deflection in the direction of the electric force.

A baseline design was optimized by varying the geometry parameters of the RFD design to determine the optimal performance of a 650 MHz cavity with the required aperture. The key parameters of the design are labelled in Figure 4.6. These include properties of the ridge such as its size and angle of the ridge backing, the diameter and length of the cavity, and additional features such as the fillet radii on edges.

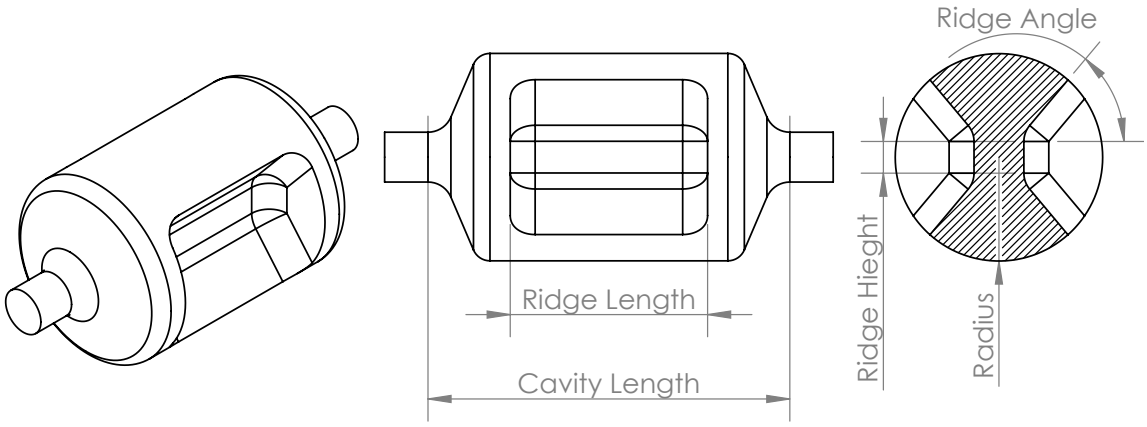


Figure 4.6: The key geometry parameters describing the RFD cavity geometry.

After an initial feasibility study that determined the baseline geometry of the cavity, a more complex parameterization of the model was developed to allow investigation of a *Post and Ridge* type geometry, with the aim of increasing the shunt impedance of the cavity. In this geometry, the shape of the inner ridge face was separated from the back of the ridge, allowing for a larger parameter space to be explored.

The development of the cavity geometry will be described in the following sections, from the initial concept to final cavity shape. To determine the behaviour of a cavity geometry, simulation tools were used to model the fields that would be supported by a given geometry. A brief introduction to the tools used in this work will be provided before describing the results of the optimization studies.

## 4.3 Computational Eigenmode Solvers

As discussed in Chapter 3, an RF cavity supports electromagnetic eigenmodes with electric and magnetic fields of a particular configuration that oscillate at specific frequencies. Each mode satisfies Maxwell's equations with the cavity geometry providing the boundary conditions imposed by the conducting cavity walls, namely that the electric field must be perpendicular to a surface and the magnetic field parallel to the surface. Computational methods are generally required to solve Maxwell's equations for most cavity geometries.

The code primarily used in this work is HFSS [17], which uses the Finite Element Method to determine the 3D electromagnetic fields. This code determines the eigenmode field solutions by breaking the volume contained within a model of the cavity geometry into a large number of smaller regions, called elements, that each locally satisfy Maxwell's equations. Together, the collection of elements that make up the cavity model are referred to as the finite element mesh.

In HFSS, the elements are four sided tetrahedrons with the local electric fields being represented by field functions at the vertices and midpoints of each tetrahedral element, points referred to as nodes. These local functions are linked to each other through the shared boundary conditions of adjacent elements, resulting in a matrix form of Maxwell's equations that may be solved using matrix techniques.

Codes such as HFSS allow the calculation of the 3D electromagnetic field profile inside complex structures. The achievable accuracy is generally limited primarily by the available computing resources. The matrix solution provides the field values at the locations of the nodes, and uses interpolation to provide values in between. Therefore, smaller mesh elements provide a more accurate solution as they require less interpolation, as well as provide a more accurate representation of the geometry.

To optimize the available computing resources, the mesh needs to be fine enough to provide a good estimation of the fields, but not contain too many elements that the solution requires excessive memory and time to compute. HFSS uses an adaptive analysis to perform mesh refinements in critical areas of the geometry in subsequent iterations of the solution to increase the accuracy of the calculation. In general, the mesh is refined until the parameters of interest, such as the frequency, or fields converge to within the desired accuracy.

The HFSS simulations were performed on a desktop computer with a mesh composed of $\sim$200 000 elements in most of the simulations performed. Usually after 2

to 3 mesh refinements, the values of the simulated frequency and calculated field parameters were found to converge to within about 0.1%. In the initial large parameter searches however, the accuracy was decreased to allow for more rapid simulations times, allowing for a more thorough search of the parameter space.

Additional software tools were used to verify the simulation results and to perform further studies not possible within HFSS. One of these was ACE3P [18], a suite of simulation codes developed for modelling accelerator structures. This code was primarily used to determine the multipacting susceptibility of the cavity geometry, but also allowed for a verification of the parameters determined through HFSS. ACE3P runs on the NERSC supercomputers [60], allowing for large scale simulations of accelerator structures. With a mesh size approximately 20 times finer than HFSS, the frequencies and RF parameters calculated with ACE3P were found to agree within $< 0.1\%$ of the HFSS results.

Multiphysics simulations were performed using ANSYS [19] which allowed for coupled RF, thermal, and mechanical simulations to be performed. This allowed for studies into effects such as the frequency shift resulting from mechanical deformations from pressure or temperature changes, or the equilibrium temperature of the cavity surface due to RF heating. An important feature for the accuracy of these multiphysics simulations was the ability to retain the same mesh throughout the simulations of different physics phenomena. This was especially important when modelling small changes in geometry due to pressure or temperature changes. ANSYS allowed for a deformed mesh from a mechanical simulation to be passed on to an electromagnetic model so that any changes that were observed could be attributed to mechanical deformations rather than changes in the determination of the mesh.

## 4.4 Geometry Optimization Studies

The final cavity geometry was developed through an optimization procedure that aimed to meet the operational requirements while adhering to limitations such as the cost of materials and fabrication, material limitations, and power requirements. This optimization was performed primarily with HFSS to solve the electromagnetic modes of different cavity shapes, with a Matlab script guiding the optimization to automate some of this process.

### 4.4.1 Feasibility Study

Starting from a parameterized RFD geometry, an optimization study was performed to determine a baseline design for the 650 MHz cavity to determine its feasibility for use as a separator cavity in the ARIEL e-Linac. The main goals of this optimization study were to optimize the shunt impedance and field uniformity while minimizing the peak electric and magnetic fields. The optimization was performed by analyzing multi-dimensional parameter sweeps of the key features of the design shown in Figure 4.6.

The separation of the ridges very strongly affects the efficiency of the RFD cavity, as was reported in [55]. Decreasing the distance between the ridges strongly increases the shunt impedance and field uniformity. Since the minimum separation of the ridges is defined by the required minimum beam aperture, the separation was held constant at the minimum value of 50 mm during the parameters sweeps. For each design iteration, the diameter of the cavity was adjusted to keep the frequency of the operating mode equal to 650 MHz.

The first parameter sweep varied both the ridge length and cavity length to determine the optimal ridge length. The peak electric field, $E_p/E_\perp$, and transverse shunt impedance, $R_\perp R_s$, are plotted in Figure 4.7. These results show that when the ridge length was approximately 0.6 times the cavity length, the peak fields were consistently found to be minimum for a given cavity length. A longer cavity length was also found to decrease the peak fields and increase the shunt impedance. This result was used to fix the ridge length to 0.6 times the cavity length for the remainder of this initial study.

The other defining features of the ridge, namely the height of the ridge face and the angle sloping back toward the outer cavity wall, were varied along with the cavity length, with the ridge length set by the relation discovered in the previous study. The results of these simulations, Figure 4.8, show the peak fields are lowest when the ridge height and angle are large, which increases the capacitance between the two ridges. The shunt impedance however decreases with increased ridge height and angle, meaning that both design goals cannot be simultaneously fulfilled.

To compromise the conflicting goals between minimizing the peak fields while maximizing the shunt impedance, intermediate values for the ridge height of 50 mm and angle of 50° were chosen, and the overall length of the cavity was set to 330 mm, after which the shunt impedance can be seen to decrease rapidly. Decreasing the

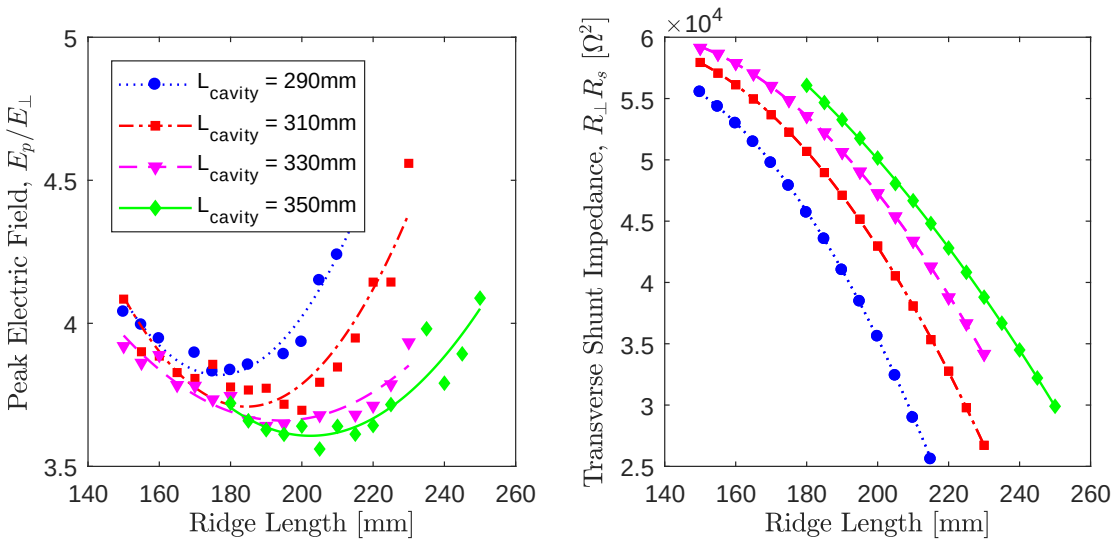


(a) (b)

Figure 4.7: a) The peak field on the cavity across the parameter space of cavity length and ridge length. b) The transverse shunt impedance dependence on the same parameters. A solution which simultaneously minimizes the peak fields and maximizes the shunt impedance is not possible.

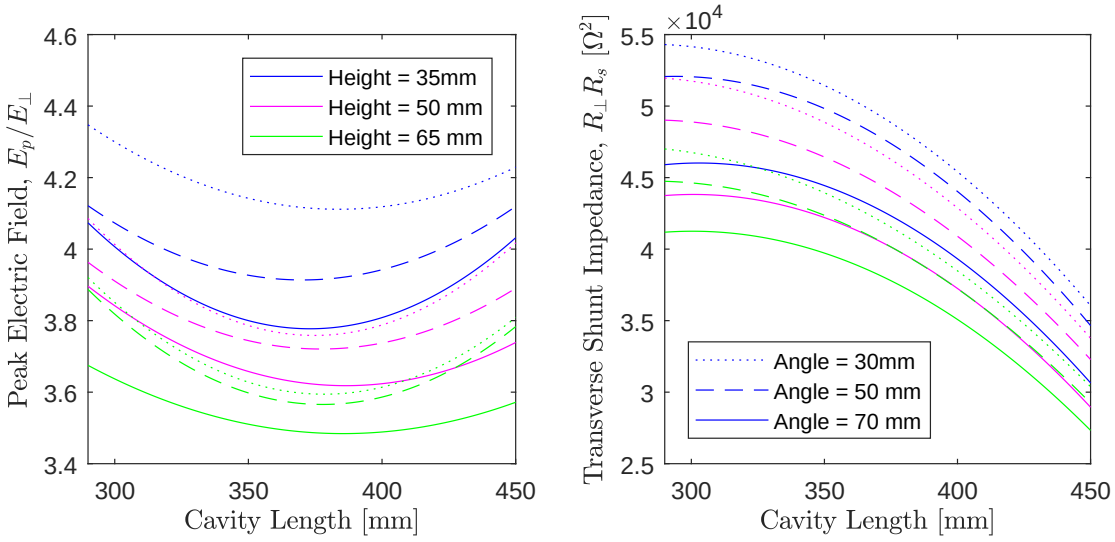


(a) (b)

Figure 4.8: The a) peak electric fields and b) shunt impedance for varying ridge height and angle as a function of the cavity length cavity length. Only the trend lines are displayed and not the individual simulation results. In both plots, the colour of the line represents the ridge height and the line type represents the angle.

length further would result in marginal gains to the shunt impedance while causing increased peak fields.

The remaining parameters, including the angle of end plates and the radius of curvature on the corners were defined through further optimization studies, but were found to have only a small effect on the overall performance of the cavity design. The properties of the optimized cavity geometry are summarized in Table 4.2. This design achieved the required deflecting voltage with very low RF power loss at 4 K and almost negligible peak electric and magnetic fields.

Table 4.2: The RF properties of the baseline design, optimized for minimized peak electric and magnetic fields.

| Parameter | Value | Units |
|---|---|---|
| Frequency of the deflecting mode | 650 | MHz |
| Cavity length | 330 | mm |
| Cavity diameter | 210 | mm |
| Inner ridge length | 198 | mm |
| Nominal transverse deflecting voltage, $V_\perp$ | 0.3 | MV |
| Geometry Factor, $G$ | 117 | Ω |
| Transverse Shunt Impedance, $R_\perp/Q$ | 411 | Ω |
| $R_\perp R_s$ | 48,000 | $\Omega^2$ |
| Peak electric field at 0.3 MV, $E_p$ | 4.5 | MV/m |
| Peak magnetic field at 0.3 MV, $B_p$ | 7.8 | mT |
| 4 K power loss at 0.3 MV | 0.4 | W |

### 4.4.2 Post and Ridge Design

Since the baseline design exhibits very low surface electric and magnetic fields for the e-Linac design operating parameters, the geometry was further optimized with less importance placed on reducing the peak fields. This new optimization method allowed the cavity to be optimized to achieve higher shunt impedance and to decrease the overall length of the cavity to reduce its longitudinal footprint.

As discussed earlier, the main contribution to the deflecting voltage is the electric field between the two ridges, with the magnetic field acting in the opposite direction to decrease the net deflection. The magnetic field component decreases the net deflecting voltage by almost 40% in the baseline design. One way to increase the shunt impedance of the cavity then is by decreasing the on-axis component of the magnetic field.

The on-axis magnetic field was decreased by adopting a *post and ridge* type design, as seen in Figure 4.9, which has similar features to a normal conducting RF Dipole cavity design developed for an RF separator for LCLS-II [61]. This geometry was inspired from the H-mode structure in an Interdigital H-mode accelerator [62]. In the post and ridge deflecting mode geometry, undercuts to the back of the ridge allow the magnetic field to be pulled away from the axis to circulate around the *post*. This results in a decreased magnetic field density on the beam axis and lowers the negative contribution to the net transverse momentum.

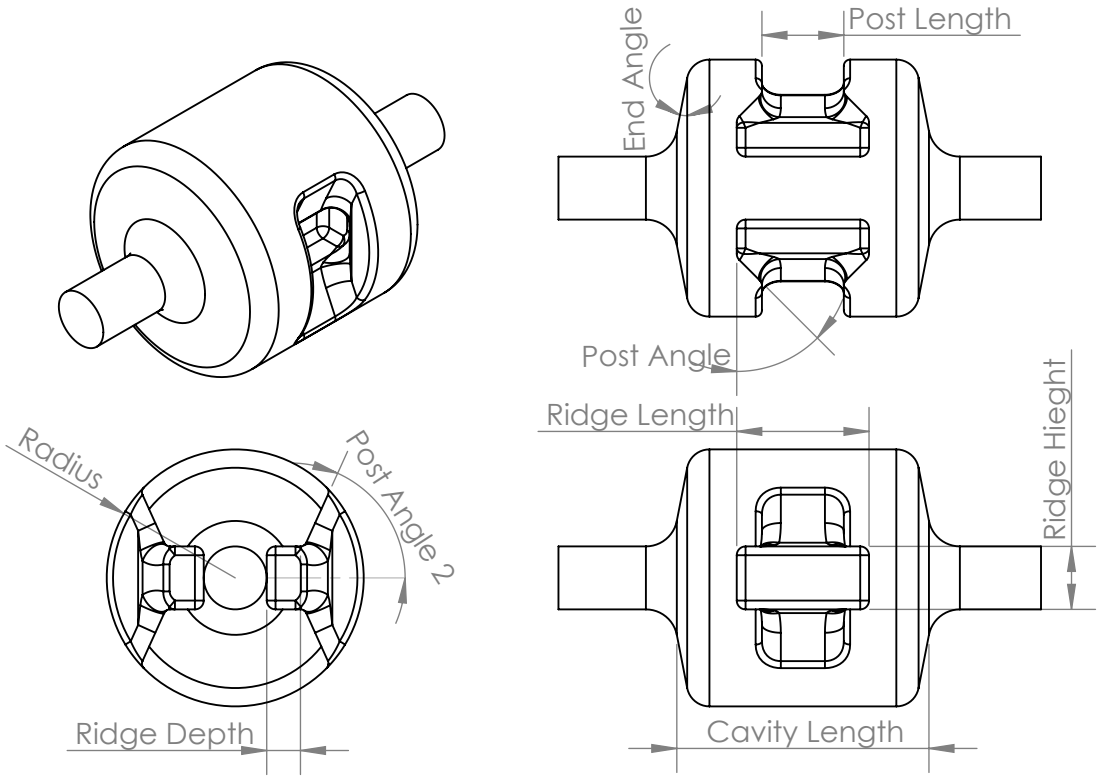


Figure 4.9: Parameterization of the post and ridge cavity geometry. Note that in the case of both the ridge depth and post angle going to zero, the undercuts are removed and the geometry returns to the RFD geometry.

A large parameter search was performed to maximize the shunt impedance of the cavity. A Matlab script was written that managed the HFSS simulations, sweeping through the parameters describing the ridge, post, and outer shape of the cavity, and recording the RF performance parameters for each geometry. With such a large number of free parameters, a full parameter search across the entire parameter space was not possible. Instead, the optimization was guided by the experience gained in

the optimization of the baseline design.

The cavity geometry with maximized $R_\perp R_s$ is shown in Figure 4.10. It exhibits a clear separation of the ridge into defined post and ridge sections, with a large undercut behind the upstream and downstream ends of the cavity. The effect of the magnetic field on the deflecting voltage has been decreased by almost half in this geometry relative to the baseline design. This results in an increase of the shunt impedance from $R_\perp R_s = 48,000\,\Omega^2$ for the baseline geometry, to $R_\perp R_s = 71,000\,\Omega^2$ for the post and ridge design, an increase of roughly 50%. The expense of this modification is that the peak electric and magnetic fields are roughly doubled for the post and ridge geometry.

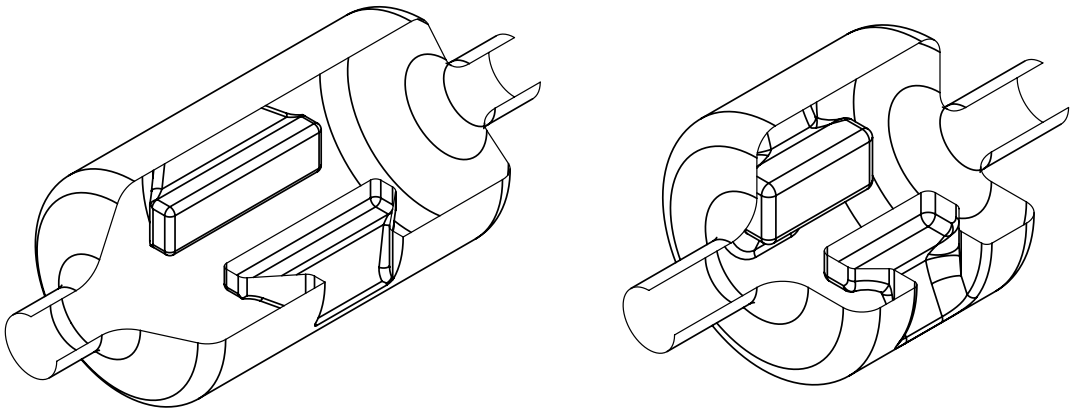

(a) (b)

Figure 4.10: The optimized post and ridge cavity geometries. a) shows the design with maximized shunt impedance, while b) is the design after decreasing the length by half.

The geometry was further modified to decrease the length of the cavity to minimize the cavity's longitudinal footprint. The resulting geometry is also shown in Figure 4.10. In addition to the length, this geometry was more carefully optimized, taking more care to optimize details such as the radii of the edge fillets. These modifications resulted in a slight decrease of the shunt impedance and an increase to the peak electric field. The peak magnetic field however was found to decrease in this configuration. In decreasing the length by almost half, from 350 mm to 178 mm, the shunt impedance was reduced from $R_\perp R_s = 71,000\,\Omega^2$ to $62,000\,\Omega^2$.

The RF performance parameters of the baseline, optimized (long) post and ridge design, and shortened post and ridge design are summarized in Table 4.3.

Table 4.3: The RF properties of the baseline and post and ridge cavity geometries.

| Parameter | Baseline | Post and Ridge | Short Post and Ridge | Units |
|---|---|---|---|---|
| Frequency of the deflecting mode | 650 | 650 | 650 | MHz |
| First HOM frequency | 1000 | 1030 | 935 | MHz |
| Cavity length | 330 | 350 | 175 | mm |
| Cavity diameter | 210 | 178 | 204 | mm |
| Inner ridge length | 198 | 150 | 105 | mm |
| Transverse deflecting voltage, $V_\perp$ | 0.3 | 0.3 | 0.3 | MV |
| Geometry Factor, $G$ | 117 | 96 | 99 | $\Omega$ |
| Transverse Shunt Impedance, $R_\perp/Q$ | 411 | 737 | 625 | $\Omega$ |
| $R_\perp R_s$ | 48,000 | 71,000 | 62,000 | $\Omega^2$ |
| Peak electric field at 0.3 MV, $E_p$ | 4.5 | 9.1 | 9.5 | MV/m |
| Peak magnetic field at 0.3 MV, $B_p$ | 7.8 | 16.5 | 12 | mT |

The short post and ridge cavity design was selected as the final cavity geometry. This geometry exhibits a high shunt impedance, reaching 50% higher $R_\perp R_s$ with 50% less length than comparable non-TM mode cavity geometries. This should result in a dissipated power of well below 1 W at 4 K, with relatively low peak electric and magnetic fields.

### 4.4.3 Beam Dynamics

In the deflecting phase, ideally all particles within a single bunch receive the same transverse momentum when passing through the cavity. However due to their spatial distribution, particles off the beam axis will see different fields than those on-axis. The nonuniform field experienced by the particles within a bunch can lead to emittance growth and multipole field components beyond the dipole field, such as quadrupole or sextupole fields. Operation of an FEL requires a beam with low emittance in the recirculation arc, and therefore minimal emittance dilution of the ERL beam as it passes through the RF separator cavity. A limit on the emittance growth of 25% has been set, while multipole effects were not considered.

The emittance growth through the RF separator was investigated with varying incoming beam parameters, cavity field strength, and cavity geometry options using the particle tracking software General Particle Tracer (GPT) [63]. The electric and magnetic fields were imported into GPT from the HFSS RF simulation and bunches of 100,000 macro-particles were tracked as they passed through the cavity.

Under nominal conditions the emittance growth of the beam through the cavity was found to be well under 1%, far below the 25% limit. The horizontal emittance was found to be most sensitive to the transverse beam size, particularly in the horizontal axis, $\sigma_x$. The nominal RMS beam sizes are less than 1 mm at the location of the RF separator, but for beam sizes greater than $\sim$ 2.5 mm the emittance could grow by more than 5% using the baseline geometry or 10% for the post and ridge cavity, as shown in Figure 4.11.

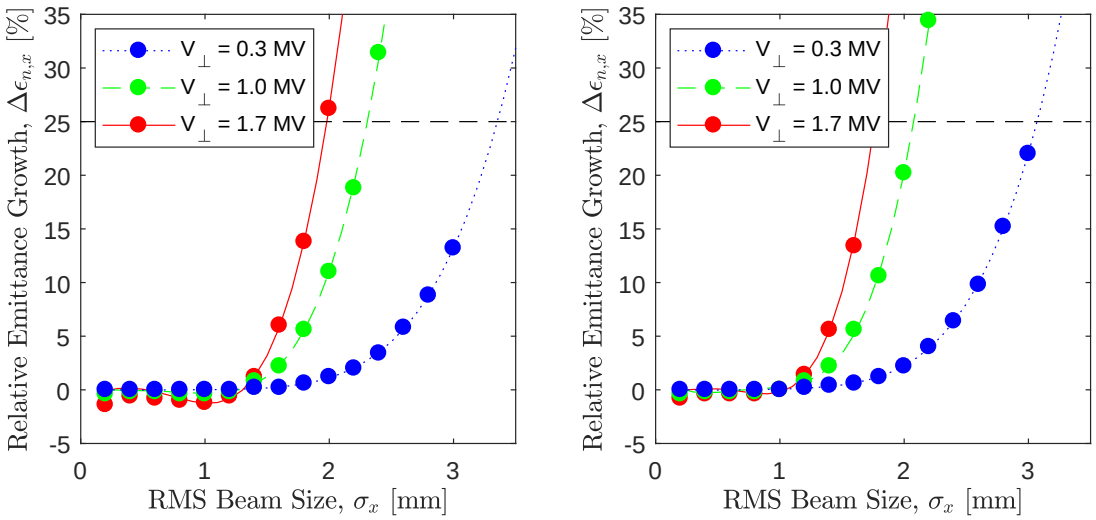


Figure 4.11: The relative transverse emittance growth, $\Delta\epsilon_{n,x}/\epsilon_{n,x}$, at the exit of the RF separator with a) baseline cavity geometry, and b) post and ridge geometry, for varying beam widths and cavity voltages. The nominal beam width is 0.7 mm.

Increasing the deflecting voltage in the cavity would also contribute to a higher emittance growth. The emittance growth can again be seen to remain less than 1% for nominal beam parameters and for deflecting voltages up to 1.7 MV. However, for higher imparted deflecting voltages, the emittance growth becomes increasingly sensitive to transverse beam sizes over 1 mm. As a result of these simulations, it was determined that the post and ridge cavity geometry would not contribute to significant emittance growth to the beam under conditions beyond nominal operating conditions.

### 4.4.4 Field Uniformity

The fields can be made more uniform across the beam aperture by adding a concave curvature to the ridge faces, as is used in the HL-LHC RFD crab cavity design. This effect can be seen in the relative magnitude of the imparted deflecting voltage across the transverse aperture in Figure 4.12 for the baseline with flat and curved ridge faces. Adding this curvature to the ridge also results in an increase in the peak electric field on the cavity, found on the edges of the ridge faces.

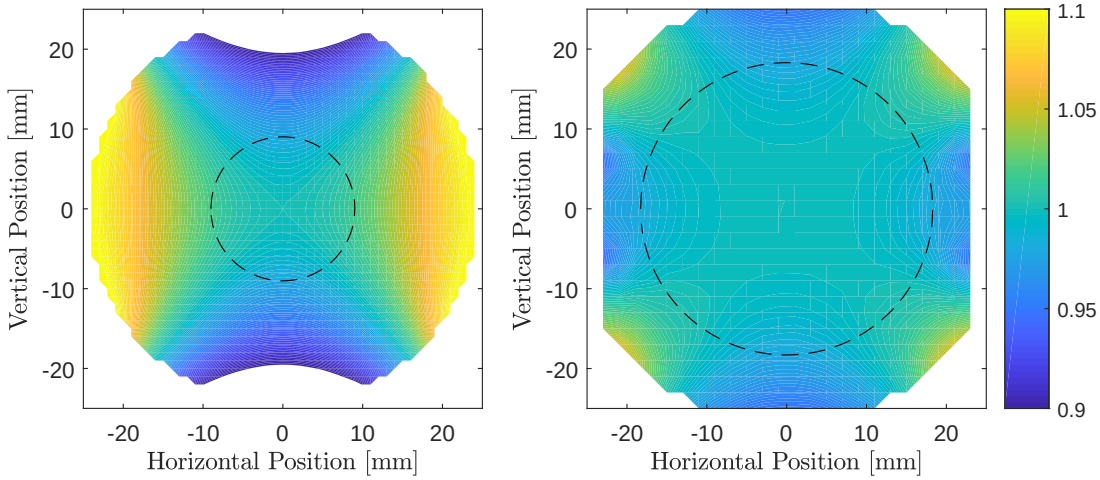


Figure 4.12: The relative magnitude of the transverse voltage as a function of the transverse position of the beam for a) the baseline geometry, and b) the baseline geometry with curved ridge faces. Both figures are plotted with the same colour scale, with the colour indicating the kick strength relative to what an on-axis particle would receive. The area within the dashed black line indicates the area with $< 2\%$ change in kick strength.

Beam dynamics simulations with the curved face geometry show increased resistance to emittance growth, as shown in Figure 4.13. However, at the nominal operating deflecting voltages required from the cavity, and across a range of beam conditions expected at this location of the linac, the cavity imparts no significant emittance growth with flat ridge faces. The ridges of the cavity were therefore left flat to avoid an increase to the peak fields and increased complexity of fabrication that would result from the change in geometry.

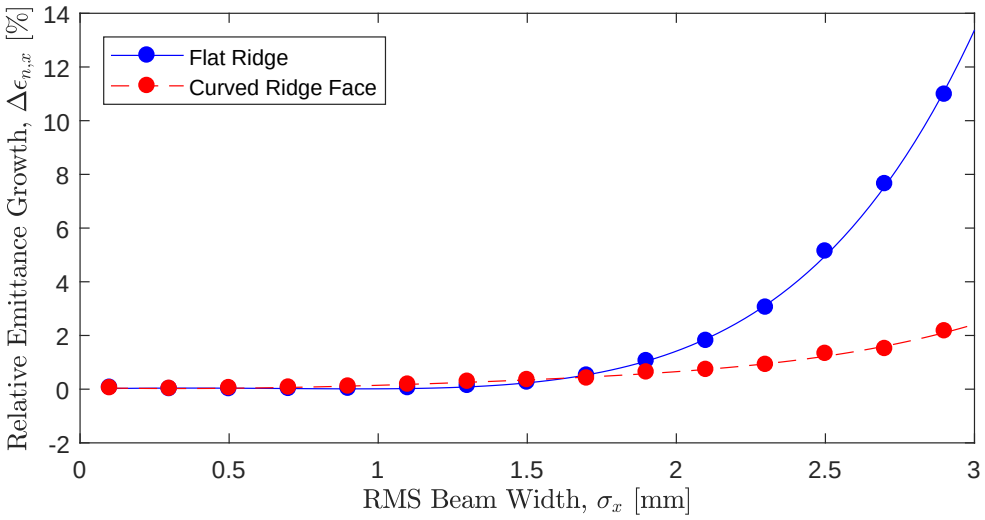


Figure 4.13: The relative emittance growth for a 5 mm-mrad incoming beam with increasing horizontal beam width for the baseline geometry with both flat or curved ridge faces.

## 4.5 Input Coupling

The input coupler, sometimes referred to as the fundamental power coupler, supplies power to the cavity to drive its operating mode. Although SRF cavities have very high $Q_0$ and generally only dissipate up to 10's of W of power, the input coupler can be required to transmit 10's of kW of RF power if the cavity is heavily beam loaded. The beam loading for the separator cavity however is expected to be quite low, as discussed in Section 3.5.2. Vector diagrams can be used to determine the optimal coupling factor for the input coupler and the power that is required to drive the cavity. This section will describe the choice of quality factor of the input coupler, and the conceptual design of a fixed input coupler that will meet this specification.

### 4.5.1 Beam Loading in the ARIEL e-Linac

As discussed previously, the bunch pattern that will pass through the separator cavity consists of bunches bound for ARIEL, the ERL, and the decelerated beam dump. The cavity will see the ARIEL bunches in the deflecting phase, spaced at 650 MHz and up to 10 mA average current, interleaved with a beam at lower frequency and high charge per bunch for the ERL in the opposite deflecting phase, most likely at 130 or 108.3 MHz. And finally, the recirculated ERL beam at the same bunch frequency will

pass through the cavity in the zero crossing phase. The ARIEL and first pass ERL bunches can contribute to reactive beam loading, while the recirculated ERL bunches may contribute to active beam loading, if offset from the cavity axis.

The beam induced deflecting voltages in the cavity from the three sets of beams passing through the cavity, $\tilde{V}_{b_{ERL}}$, $\tilde{V}_{b_{RIB}}$, and $\tilde{V}_{b_{rec}}$, accounting for their phases and cavity detuning, are

$$\tilde{V}_{b_{ERL}} = -i\frac{I_{ERL}{}^{R_\perp}\!/_Q Q_0}{1+\beta} k\Delta x_{ERL} \cos\psi e^{i\psi} \tag{4.2}$$

$$\tilde{V}_{b_{RIB}} = +i\frac{I_{RIB}{}^{R_\perp}\!/_Q Q_0}{1+\beta} k\Delta x_{RIB} \cos\psi e^{i\psi} \tag{4.3}$$

$$\tilde{V}_{b_{rec}} = \pm\frac{I_{ERL}{}^{R_\perp}\!/_Q Q_0}{1+\beta} k\Delta x_{rec} \cos\psi e^{i\psi} \tag{4.4}$$

where $I$ is the average beam current in each beam, remembering that $I_{ERL} = I_{rec}$, and $\Delta x$ is the offset of each beam from the beam axis. $\psi$ again is the detuning angle, defined in Equation (3.30). The beam loading from the decelerated beam may change directions depending on which zero crossing phase the decelerated bunch passes through the cavity at.

With these three beams passing through the cavity, the total voltage induced in the cavity, including the generator induced voltage, is given by the vector sum

$$\tilde{V}_c = \tilde{V}_g + \tilde{V}_{ERL} + \tilde{V}_{RIB} + \tilde{V}_{rec}. \tag{4.5}$$

The vector diagram in Figure 4.14 shows the vector sum of the beam loading from the three beams present in the cavity, here assuming that the offset of all the beams is in the same directions. The beams bound for ARIEL and the ERL are plotted on the real axis, indicating that they would see the maximal cavity voltage, while the recirculated beam sits on the imaginary axis.

As before, solving for the generator voltage that would result in the desired cavity voltage can lead to an expression for the required power. Using a simplified notation for the contributions from each beam in the format of

$$V_{ERL} = \frac{I_{ERL}{}^{R_\perp}\!/_Q Q_0}{1+\beta} k\Delta x_{ERL}, \tag{4.6}$$

and similarly for $V_{RIB}$, and $V_{rec}$ after substituting their beam currents and beam

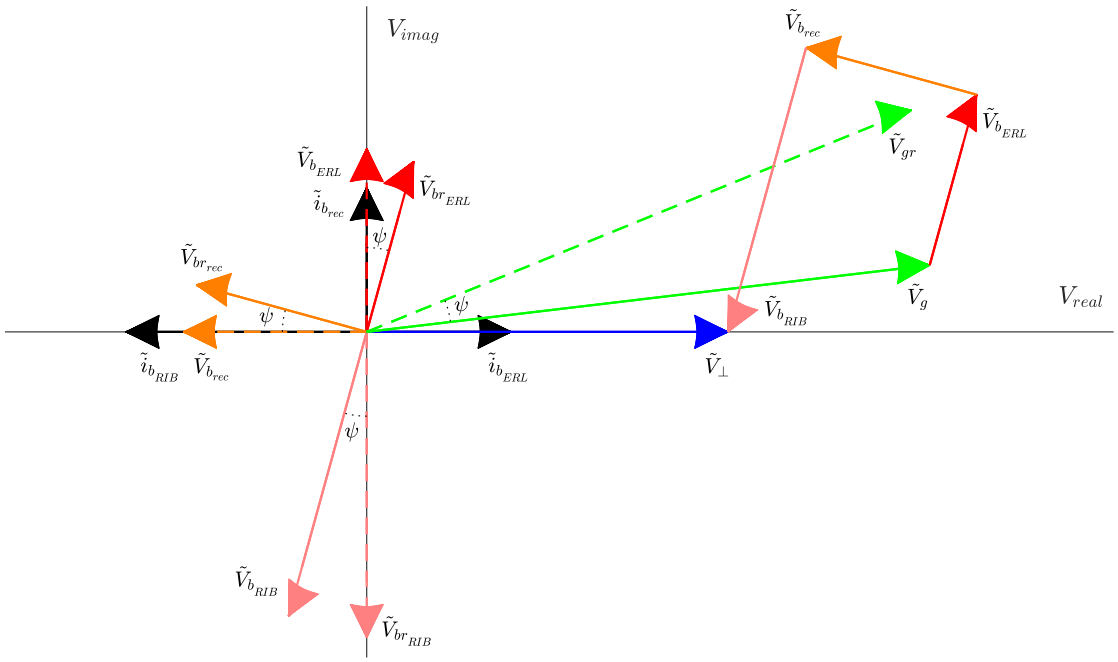


Figure 4.14: Vector diagram representing the beam loading for the separator cavity in the case of a 10 mA beam bound for ARIEL and a 6 mA ERL beam, all with a 1 mm horizontal offset within the cavity and 50° frequency detuning.

offsets, the formula for the required power is

$$P_g = \frac{(1+\beta)^2}{4\beta}\frac{1}{R_\perp/_Q Q_0}\left\{\left[V_\perp + (V_{ERL} - V_{RIB})\sin\phi \mp V_{dec}\cos\phi\right]^2 + \right.$$
$$\left. + \left[(V_{ERL} - V_{RIB})\cos\phi \pm V_{dec}\sin\phi - \tan\psi\right]^2\right\}, \quad (4.7)$$

which simplifies to Equation (3.44) in the case of a single beam. The nominal operating phase here would be $\phi = 0$.

Different possible combinations of beam currents in the ARIEL and ERL beams, beam offsets, and detuning, lead to a large parameter space of beam loading conditions. In one limit, the different beams may act together to drive the power requirements higher, while in other combinations, the different beams may cancel out each other's beam loading, or even drive the cavity voltage, resulting in a reduced power requirement. Figure 4.15 shows the required power as a function of the input coupler's $Q_{ext}$ for several cases of beam loading.

A value for the $Q_{ext}$ of the input coupler in the range of $3 \times 10^6$ would result in

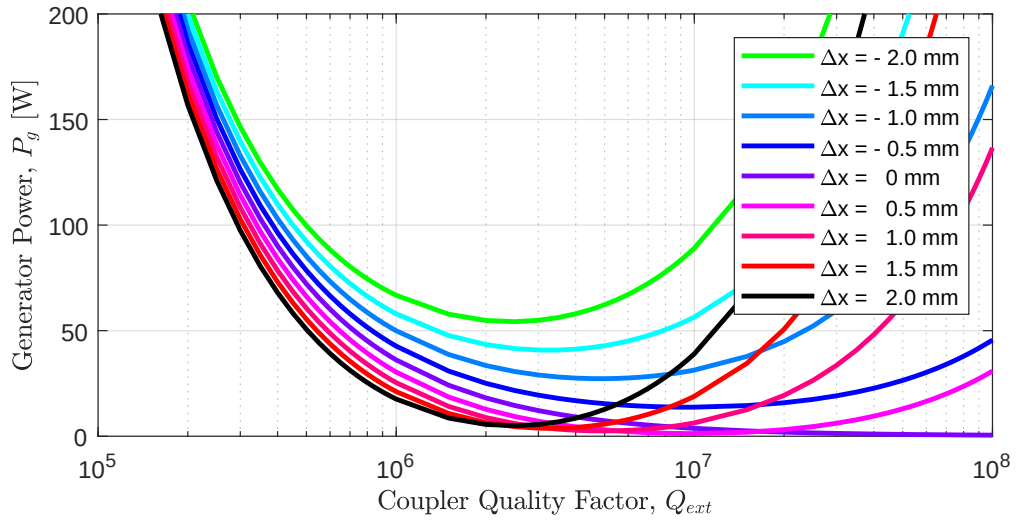


(a)

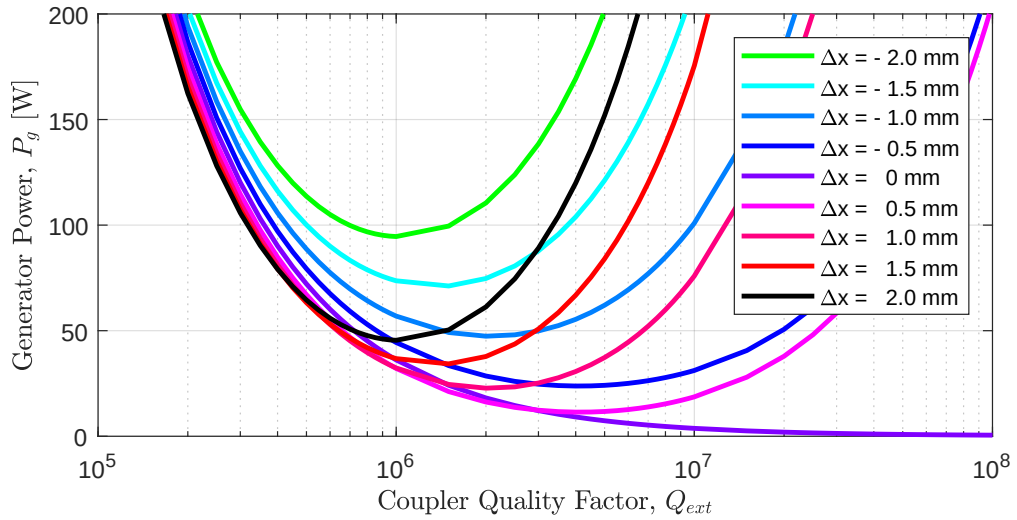


(b)

Figure 4.15: The required power to drive a 0.3 MV deflecting voltage as a function of the input coupler quality factor for different cases of beam loading. In both plots, a 10 mA ARIEL beam and a 6 mA ERL (and recirculated) beam pass through the cavity. In a) all beams are offset in the same direction, and in b), the ARIEL beam is offset in the opposite direction to the ERL and recirculated beams, increasing the power requirements significantly.

reasonable power requirements for up to 2 mm of transverse beam displacement. With this coupling, the cavity will require 10–20 W of power under nominal conditions with no beam loading or detuning of the cavity. With a 200 W amplifier, the cavity may sustain a deflecting voltage of 0.3 MV with up to several mm of beam offset. The power requirements scale with the deflecting voltage squared, meaning operating at 0.6 MV under these conditions would require at minimum 20–40 W.

The required power from the amplifier may be decreased further under conditions where the reactive component of the beam loading is compensated for by detuning the cavity. The amount of detuning can be determined from Equation (4.7) by setting

$$\tan\psi = (V_{ERL} - V_{RIB})\cos\phi \pm V_{dec}\sin\phi. \tag{4.8}$$

The effectiveness of this is illustrated in Figure 4.16, where the power requirement is plotted under the same beam conditions with and without detuning. At the design $Q_{ext}$, the required power is decreased by half by changing the goal frequency of the tuner by 150 Hz.

### 4.5.2 Conceptual Design of the Input Coupler

Power will be provided to the cavity through a coaxial input coupler located on the end plate of the cavity, with an antenna that couples to the electric fields of the operating mode. The coupler port is located near the beam pipe, in the horizontal plane of the cavity, as this region has the highest surface electric fields other than on the ridge itself. The distance from the tip of the antenna to the cavity surface determines the strength of the coupling, and the $Q_{ext}$ of the coupler. Due to the limited space available and low beam loading, a fixed input coupling will be used.

The input coupler will run parallel to the beam pipe near the cavity, but due to spatial constraints, will make a 90° bend to direct the path of the input coupler away from the cavity, as shown in Figure 4.17. After the bend, a bellows will separate the cold section of the coupler to a liquid nitrogen intercept on the outer wall of the coupler that will conductively cool the inner conductor. A vacuum feedthrough will connect to a 50 Ω coaxial cable, delivering power from the RF amplifier.

Although the thermal transition section has not been fully designed, initial studies were performed on the temperature response of the inner conductor to the dynamic heat load on the tip of the antenna, cooled by liquid nitrogen at the root of the inner conductor. This heat load is a result of the magnetic fields from the operating mode

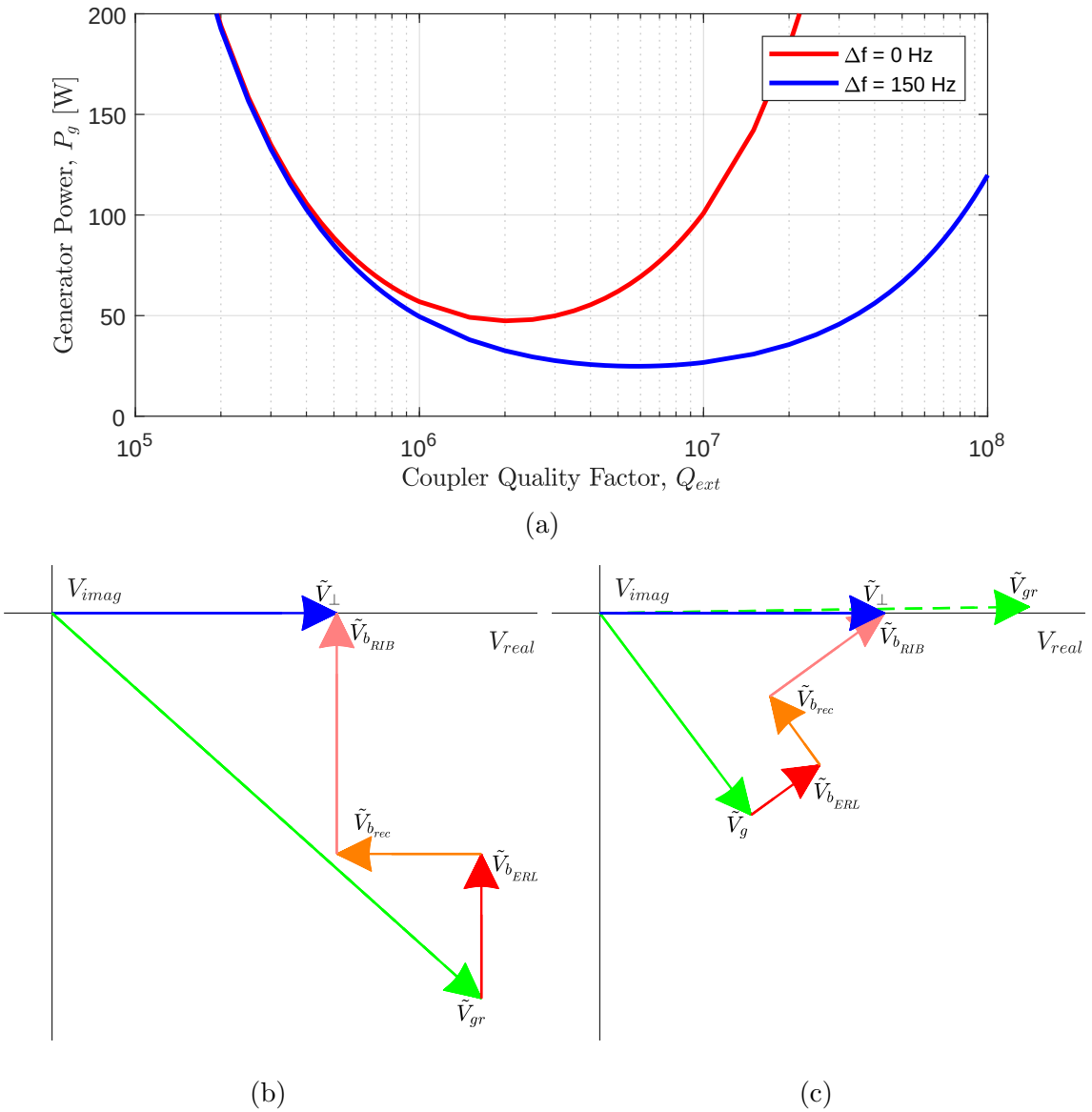


Figure 4.16: a) The power required to drive the cavity with and without cavity detuning. The vector diagrams for these two cases are shown at the same scale in b) with no detuning, and c) with detuning. With detuning, the length of the generator induced voltage vector, $V_{gr}$ is reduced, reducing the required power by about half in this case.

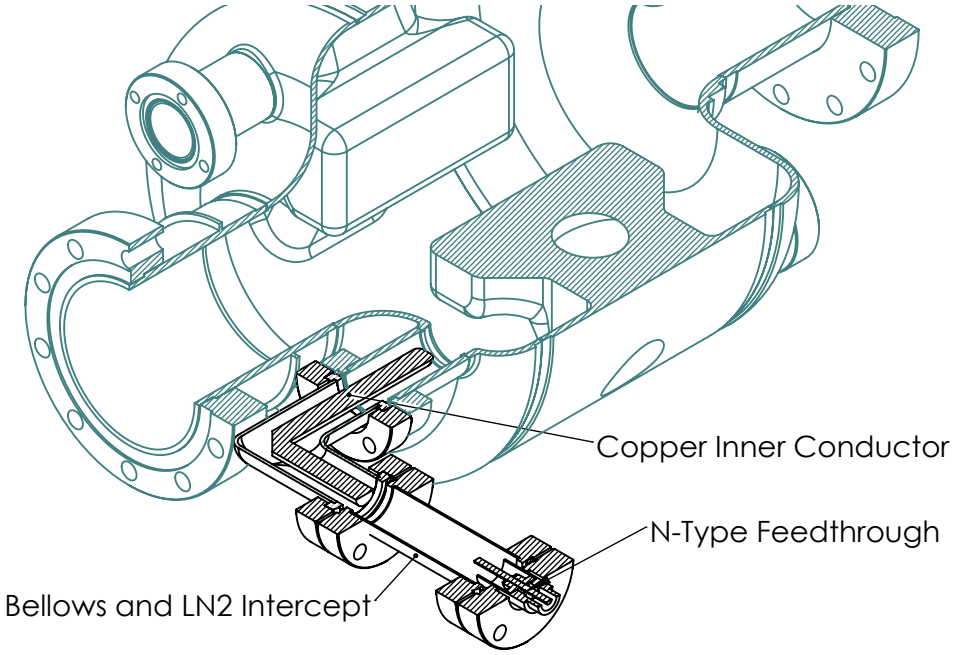


Figure 4.17: A cross section of the fixed input coupler mounted on the cavity. The transition from 4 K to the liquid nitrogen cooling intercept is not shown.

reaching the antenna and dissipating on its normal conducting surface. Under normal operating conditions, up to a couple watts of power can be dissipated on the tip of the copper antenna. This heat must be conducted down the inner conductor to be removed by the liquid nitrogen cooling.

Thermal simulations show that the maximum temperature rise of the antenna could reach 50 to 100 K under the maximum operating voltage, depending on the geometry of the inner conductor. This would result in less than 1 mW of radiative heat transfer to the cavity and will not affect the performance of the cavity.

## 4.6 HOM Damping Studies

HOM couplers and dampers are structures that are required to extract energy transferred to the cavity from the passing bunches that excite HOMs. If not sufficiently damped, HOMs can dissipate power on the cavity walls and cause instabilities in the beam. These devices must couple to modes at the HOM frequencies, but reject damping power from the operating mode. The extracted power may be transmitted away from the cavity to be dissipated at a higher temperature to limit the heat transfer to

the liquid helium system.

The geometric shunt impedances of the modes that can be supported by the cavity geometry were calculated using HFSS. The values of the transverse and longitudinal geometric shunt impedances where determined by integrating the fields along the beam axis using Equations (3.46) and (3.47). The modes are classified as either longitudinal – with electric field along the beam axis, or deflecting modes that impart a transverse kick. The deflecting modes can deflect in either the horizontal or vertical directions, depending on their field orientation. The spectrum in Figure 4.18 shows the geometric shunt impedance, $R/Q$, of all of the modes up to 3 GHz.

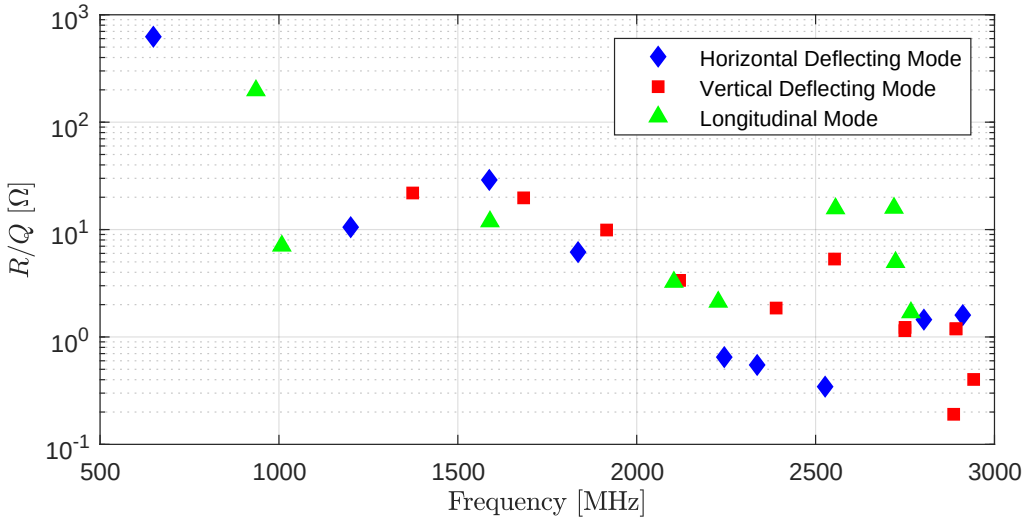


Figure 4.18: The geometric shunt impedance of modes up to 3 GHz. The operating mode has the highest shunt impedance and the first HOM has a frequency of 935 MHz.

The effect that a HOM may have on the beam is characterized by the shunt impedance, $R/Q \cdot Q_L$, through the processes described in Section 3.6. Reducing the shunt impedance of a HOM can be achieved either by decreasing the geometric shunt impedance, which is a property of the cavity geometry, or by decreasing the loaded $Q$ of the HOM, through the addition of HOM damping structures.

In addition to damping HOM power from the cavity, HOM couplers and dampers may also act as vacuum barriers and transitions from cold to warm temperatures. Due to their proximity to the cavity, they can experience power dissipation from the operating mode and sometimes require superconducting components – depending on their location relative to the cavity. They also need to be cleaned and handled with the same care as the cavity.

### 4.6.1 HOM Coupler and Damping Structures

The three main categories of HOM dampers are coaxial couplers, waveguides, and beam pipe absorbers. The type employed depends on a number of factors ranging from the frequencies of the modes to be damped, to mechanical considerations such as available space or the expected heat load.

Coaxial couplers can be compact structures and are able to transmit power at any frequency to an external load. The operating mode must therefore be blocked from being transmitted through the coupler to avoid significant power transfer to the HOM load. Coupling to the modes can be achieved though either the electric or magnetic fields by inserting an antenna or loop coupler into the cavity in an area with field components in the mode to be damped.

By placing the antenna in such a location that the operating mode has no field components present, no power can be transfered to the HOM coupler. More commonly, suppression of the fundamental mode is achieved by including a high pass or notch filter in the transmission line that results in low transmission at the operating frequency and optimized transmission at the frequencies of the HOMs.

Waveguide HOM couplers are generally rectangular tubes that usually connect directly to the cavity body to couple to the electric field of the HOMs. Waveguides may be designed to naturally block the operating mode from propagating by selecting dimensions such that the cut-off frequency of the waveguide is higher than the fundamental mode frequency. If the frequencies of the HOMs to be damped are low, waveguides can be quite large and can result in significant thermal transfer to the cavity. Additionally, multiple waveguides installed at different positions are usually required to couple to different mode polarizations, resulting in a very bulky cavity.

Beam pipe absorbers are used to damp power from modes that propagate down the beam pipe. These consist of a lossy material placed in the beam pipe that dissipates power when a mode has a magnetic field component present on the surface of the damper. Materials such as ferrite or stainless steel have been used [64, 65], and these can be cooled either by water cooling if the damper is located outside of the cryomodule or by liquid nitrogen if located at a cold location.

The beam pipe acts as a high-pass filter, blocking the propagation of modes below a characteristic cutoff frequency. For a circular waveguide, the cutoff frequency can be estimated as

$$f_c = \frac{1.842c}{2\pi a}, \tag{4.9}$$

which is the frequency of the lowest order TE mode that can be supported within the waveguide with radius $a$, where 1.842 is the first root of the derivative of the first order Bessel function of the first kind, $J_1(r)$. Fields from resonant modes that are below the cut-off frequency may also be dissipated on a beam pipe damper, but these experience an exponential decay in their intensity along the beam pipe. The design of a beam pipe HOM damper must consider the power dissipated from the operating mode, ensuring that the damper is located far enough from the cavity that fields have decreased sufficiently.

### 4.6.2 HOM Damping Design

The HOMs in the separator cavity will be damped through a combination of a coaxial HOM coupler mounted on the end wall of the cavity and a stainless steel damper located in the beam pipe. These are shown mounted on the cavity in Figure 4.19.

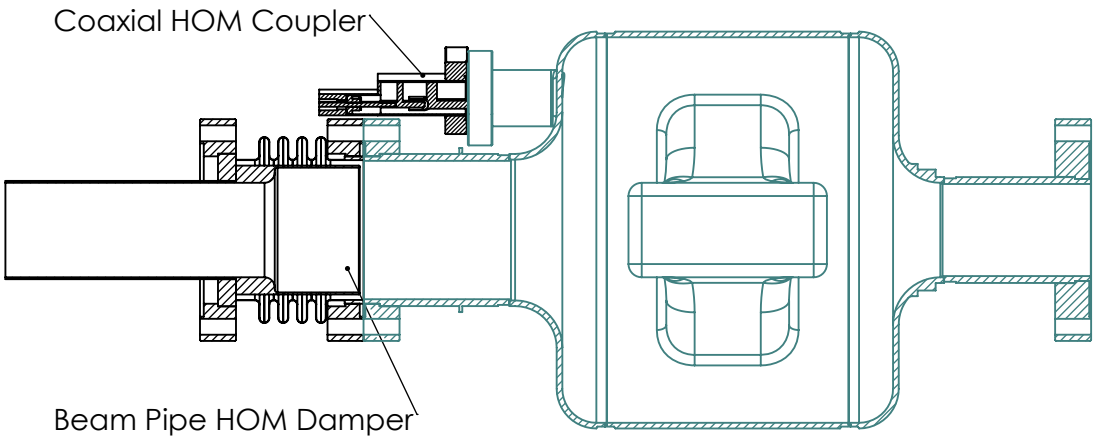


Figure 4.19: The cavity with HOM coupler installed on the cavity end plate, and the HOM damper on the upstream beam pipe.

The HOM damper consists of a stainless steel tube, located just at the end of the cavity beam pipe that is cooled by liquid nitrogen to 77 K. The beam pipe was enlarged on one side of the cavity from 50 mm to 73 mm to reduce the cut-off frequency of the

beam pipe from 3.5 GHz to 2.4 GHz to allow the propagation of more HOMs toward the beam pipe damper. The positioning of the stainless steel damper was chosen such that the power loss to the HOM damper was about an order of magnitude less than to the cavity walls, resulting in a $Q_{ext}$ of $5 \times 10^9$ for the operating mode.

With the stainless steel HOM damper alone, most transverse modes with frequency greater than the cut off frequency of the beam pipe would be damped to below the goal shunt impedance set by multipass BBU, as seen in Figure 4.20. The design of the coaxial HOM coupler was then focused primarily on the first 10 to 15 modes, plus a few non-propagating accelerating modes around 2.5 GHz.

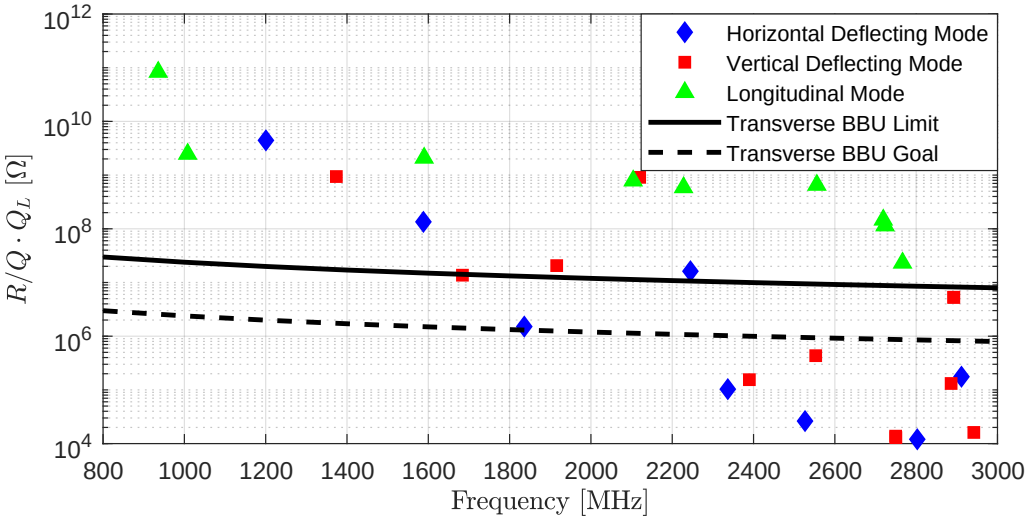


Figure 4.20: The shunt impedance of modes up to 3 GHz, damped by the stainless steel HOM damper alone.

The HOM coupler is mounted on the cavity end plate, on the same side of the cavity as the input coupler and the beam pipe damper. Due to the enlarged beam pipe, the fields for most modes are slightly higher on this end of the cavity, resulting in stronger coupling than on the downstream side of the cavity. A single HOM coupler will be used that is required to couple to all of the modes that are not sufficiently damped by the HOM damper. Its placement on the cavity is limited such that it couples to many modes, and cannot be placed in a location with no coupling to the operating mode. Therefore the coupler consists of a coaxial antenna with a notch filter built in to block transmission of the operating mode at 650 MHz.

A single stage notch filter was developed that features a band-stop centred at 650 MHz to block the operating mode. The design was based on single and double

stage filters such as those used for LEP cavities [66] and developed for eRHIC [67]. The filter is integrated into the coupler and is shown in Figure 4.21.

The notch filter consists of a capacitive gap and inductive stubs that are tuned to provide the band-stop at the fundamental mode frequency and a fast rise in transmission to allow the first HOM to be transmitted. A simplified circuit model was developed of the coupler, and simulated in LTspice [68] to study how these different features would affect the transmission characteristics. A schematic of the circuit studied is shown in Figure 4.21.

The values of the capacitors and inductors in this model were varied to optimize the transmission spectrum. The goal was to achieve a broad stop band at 650 MHz to ease tuning of the filter. A fast rise in transmission is required to allow power transfer of the first HOM at $\sim$ 940 MHz, followed by good transmission to frequencies of at least several GHz where the modes are primarily damped by the beam pipe damper.

Once a reasonable solution was found using the circuit model, the components had to be translated into geometric parameters in the physical device. This was primarily achieved through modelling in HFSS by trial and error. A parametrized model was developed that allowed the different dimensions to be varied while comparing the transmission spectrum to that achieved through the LTspice model.

The resulting HOM coupler design is shown in Figure 4.21. The two stubs provide mechanical support of the inner conductor as well as the inductive components to the filter. A large capacitance was required, which resulted in the cup-like gap between the first and second inner conductors. Additionally, the first inner conductor was placed off the centre axis to include a second capacitance to ground. The resulting transmission spectrum of the coaxial coupler is plotted in Figure 4.22. The coupler blocks power at the operating mode, decreasing the output intensity by more than 50 dB over a range of 20 MHz about the operating mode frequency. The filter has exceptional transmission for modes above 1 GHz.

The physical realization of this coupler has been considered, although not finalized. The inner conductor of the damper is required to be fabricated from niobium to reduce the dynamic heat load on tip of the tip of the antenna. Cooling the niobium to below the critical temperature requires liquid helium cooling of the coupler body. The mechanical stability of the structure and the dimensional changes due to the cool down from room temperature have also been analyzed. While the HOM coupler still requires some details to be worked out, this conceptual design has provided the confidence that sufficient HOM damping can be achieved in the separator cavity.

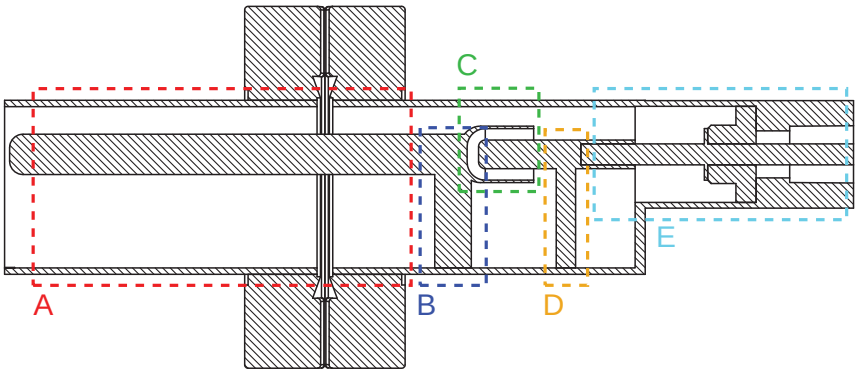


(a)

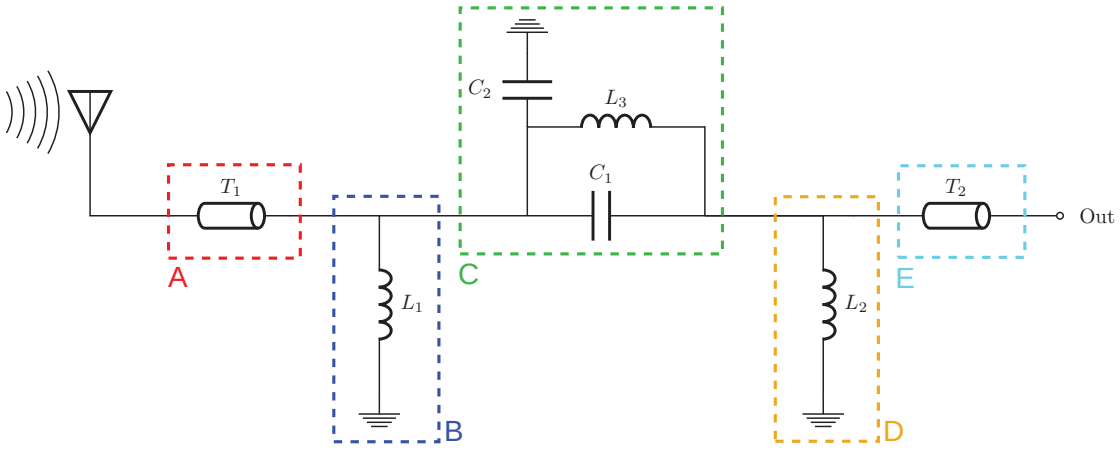


(b)

Figure 4.21: a) A cross section of the HOM coupler. The antenna is on the left and vacuum feedthrough on the right. The filter is made up of the elements in between the antenna and feedthrough. b) The equivalent lumped circuit model of the HOM coupler. The coloured boxes indicate how each section of the coupler are represented in the circuit model.

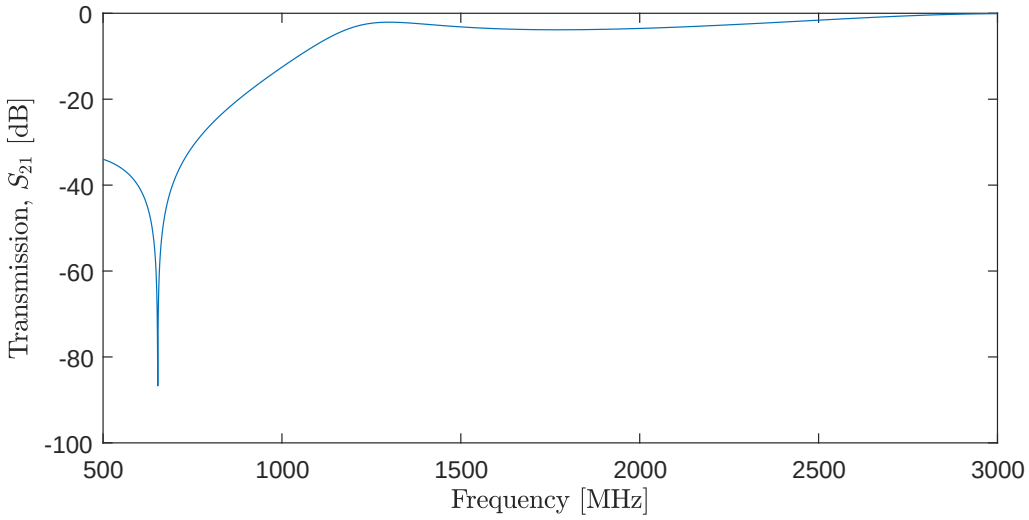


Figure 4.22: The transmission spectrum of the HOM coupler.

The placement of the HOM coupler on the cavity was optimized using HFSS by considering the $R/Q \cdot Q_L$ of all HOMs up to 3 GHz, with the objective of reaching the goal shunt impedance set by multipass beam breakup for transverse modes and to limit the power dissipation of longitudinal modes. Coupling on the end plate of the cavity was found to couple to most modes, and was mechanically more convenient than other possible locations.

The key parameters defining the placement of the HOM coupler on the end plate of the cavity were its radial and angular position, and the extension of the antenna into the cavity. Simulations of the full geometry, including the HOM damper and coupler were used to determine the dependence of the shunt impedance on the placement of the HOM coupler for the modes of interest. With only a single HOM coupler, sufficient coupling to all of the required modes was difficult to achieve.

After numerous design iterations, a solution was found that placed the coupler at an azimuthal position of 25° from the vertical plane such that it would be able to couple to modes of both horizontal and vertical polarizations. Even so, a few modes exist that contain an electric field minimum at the location of the coupler, limiting their ability to couple to the HOM coupler antenna. The distributions of the surface electric field on the upstream end plate of the cavity for a few modes are shown in Figure 4.23 to illustrate this point.

The final positioning of the HOM coupler was determined that damped all transverse modes to at or below the goal shunt impedance, as shown in Figure 4.24. The

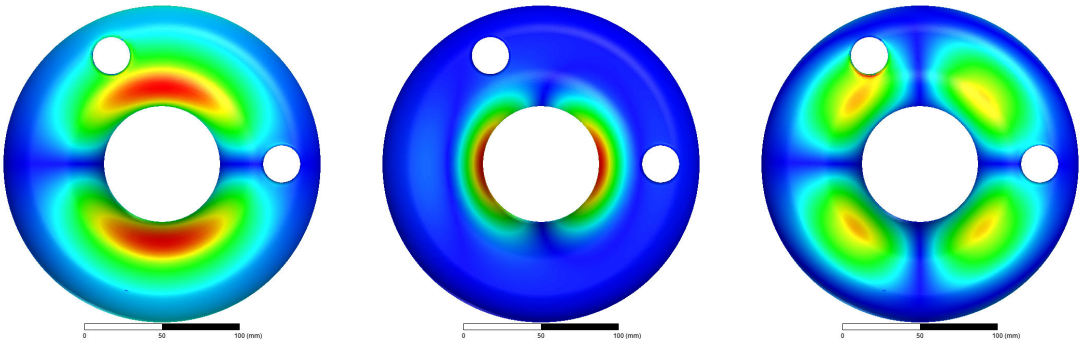

(a) (b) (c)

Figure 4.23: The magnitude of the electric field on the upstream end plate for HOMs at a) 935 MHz, b) 2344 MHz, and c) 2725 MHz. The location of the HOM coupler port is indicated by the white circle on the upper left. The HOM coupler is able to couple to the electric fields in a) and c), but not strongly to the mode in b).

placement of the coupler was such that the few modes that were not coupled to the HOM coupler, experienced significant damping by the HOM damper. One such mode exists at 2344 MHz that experienced weak coupling to the HOM coupler – with a $Q$ of $5 \times 10^8$, while the HOM damper provided a much more significant damping of $2 \times 10^5$. Most modes were damped to a $Q$ of below $10^4$ by the HOM coupler alone.

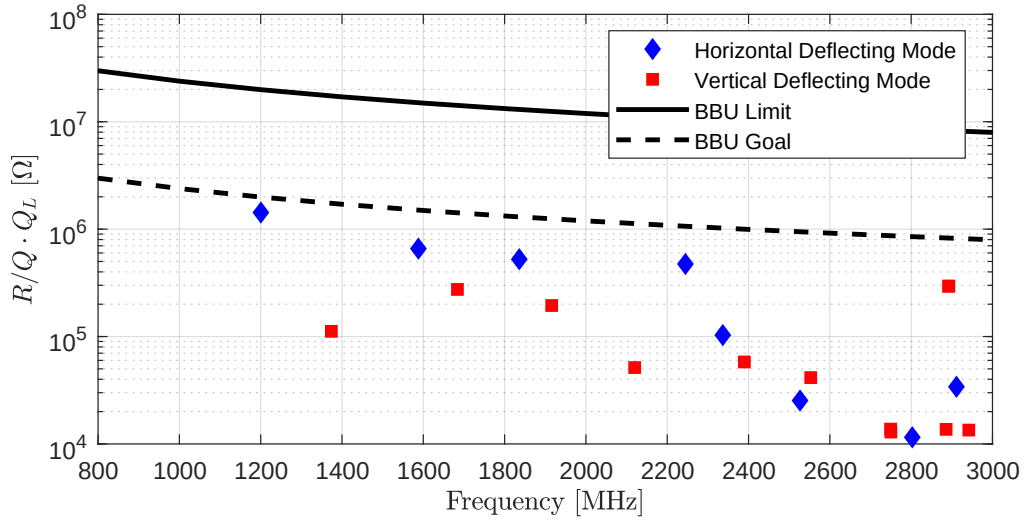


Figure 4.24: The shunt impedance of the transverse deflecting modes up to 3 GHz, damped by the stainless steel damper and HOM coupler.

The power dissipated in the HOMs depends strongly on the mode frequency compared to the bunch structure passing through the cavity. This power is maximum if

the mode frequency is at an integer multiple of the bunch repetition rate, resulting in resonant driving conditions. Additionally, transverse modes require an offset from the beam axis to couple energy into a mode. Since the beam nominally passes through the cavity on axis, only minimal power was found to be dissipated in transverse modes, even under resonant conditions. The frequency of most of the longitudinal HOMs are far from resonant with a beam harmonic and therefore would dissipate less than a mW of power. Figure 4.25 shows the power dissipated at mode frequencies and over a range of 1% of the simulated resonant frequency for the longitudinal HOMs.

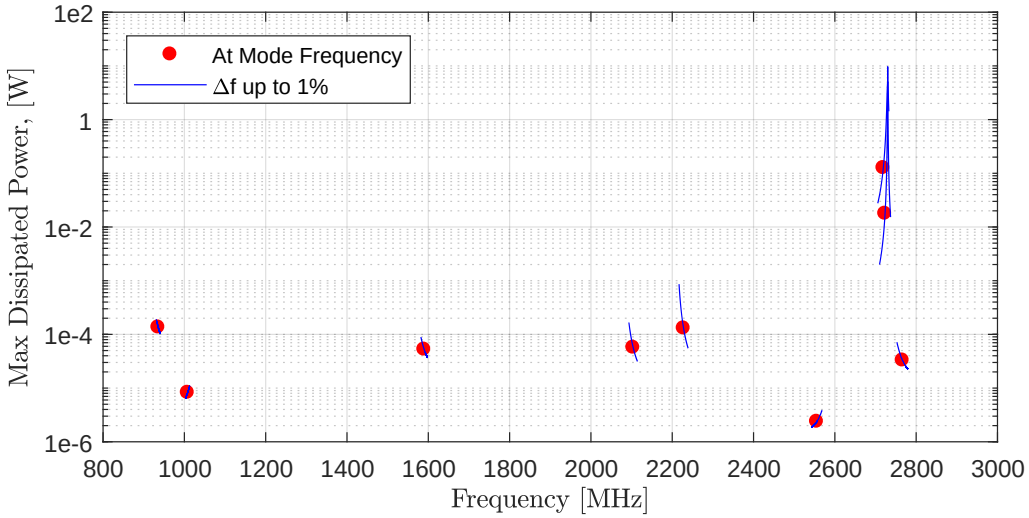


Figure 4.25: The power dissipated from longitudinal HOMs from a 20 mA ERL beam with 130 MHz bunch spacing. The red circle represents the power dissipated at the frequency determined from simulation studies, and the blue line shows the power that would be dissipated at frequencies by up to 1% on either side.

Only two modes located near 2730 MHz were found to have resonant frequencies close to a 130 MHz beam harmonic. These modes were studied further to determine how their frequency and shunt impedances changed depending on geometrical tolerances. It was determined that under typical fabrication errors, the maximum power that could be dissipated from these modes would be on the order of a few watts.

The final geometry of the HOM damping scheme is shown in Figure 4.26. Nominally, less than 1 W will be transfered through the HOM coupler to be transmitted out of the cryomodule through a coaxial cable and dissipated in a room temperature load. Less than 1 mW will be dissipated on the stainless steel HOM damper that will be cooled by an active liquid nitrogen cooling loop. The damper will be separated

from the cavity through a bellows between the location of the liquid nitrogen intercept and the cavity flange to limit the heat transfer to the helium bath.

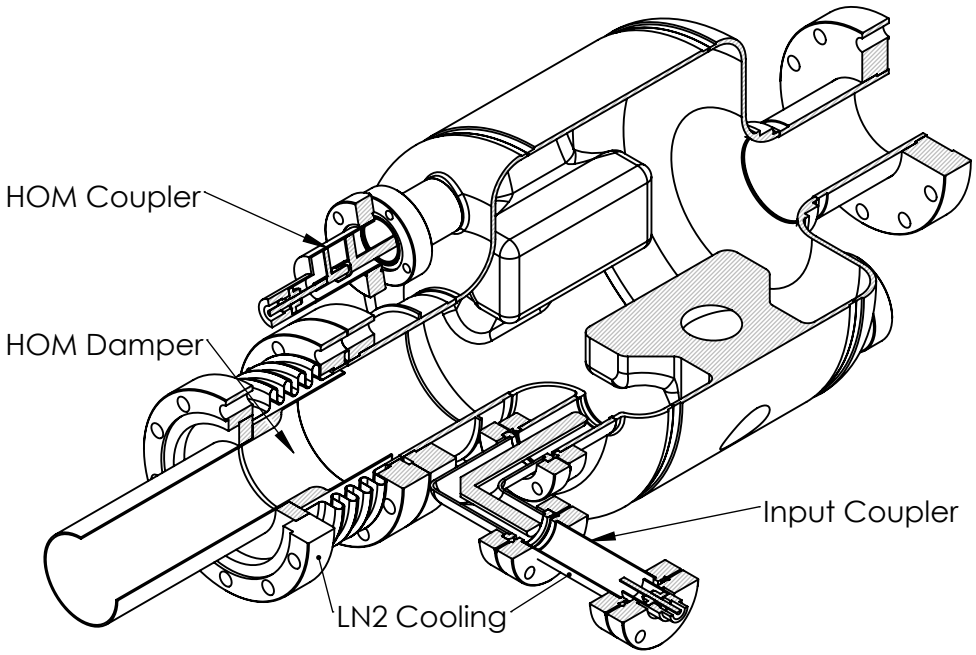


Figure 4.26: The cavity with HOM coupler installed on the cavity endplate, and the HOM damper on the upstream beam pipe.

## 4.7 Pick Up Probe

A pick up probe is included on the cavity to measure the field amplitude within the cavity during operation. The pick up probe weakly couples to the operating mode, transferring the pick up signal to the cavity control system to control the input power fed back to the cavity and the tuner to adjust the cavity frequency. The quality factor of the pick up is typically a couple orders of magnitude higher than the cavity $Q_0$ such that it does not drain significant power from the cavity.

The pick up antenna couples to the electric field of the cavity, requiring it to be located at a position with a surface electric field. It was decided to position it on the downstream side of the cavity, such that it mirrored the location of the HOM coupler, placing it on the lower half of the cavity. A key reason for the positioning of the port here is that together with the HOM coupler port, they provide access to a rinse wand for performing a high pressure water rinse of the upper and lower faces of the ridges

performed during surface preparation of the cavity. These are areas that would not be reached through the beam pipe alone. The process of high pressure water rinse will be discussed in more detail in Section 5.6.1.

The pick up probe consists of an antenna mounted to a vacuum feedthrough. The diameter of the antenna was set to match the radius of the inner conductor of a Type N feedthrough. The length of the antenna determines the coupling to the operating mode and its quality factor. HFSS was used to model the coupling of the pick up antenna to determine the required length, with the results plotted in Figure 4.27. For cryogenic tests, the length was chosen to achieve a $Q_{pu} \sim 10^{11}$ to be at least an order of magnitude greater than the possible $Q_0$ at 2 K of $\sim 10^{10}$.

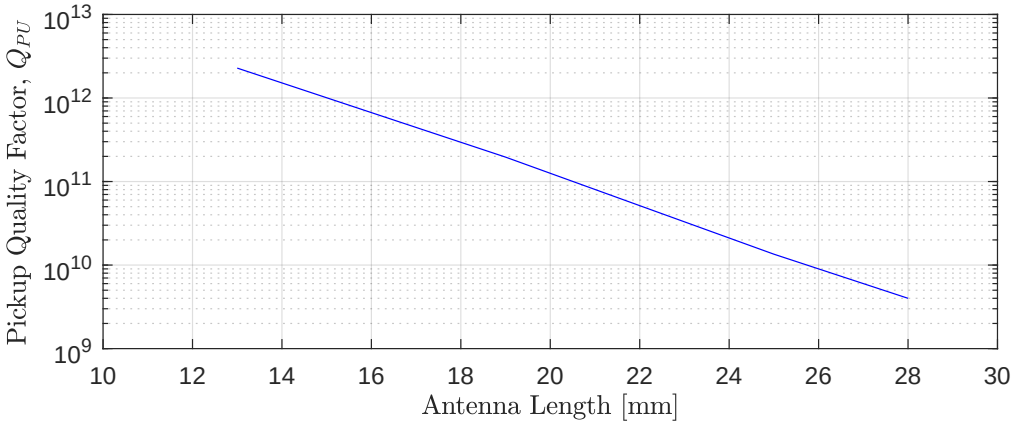


Figure 4.27: The external quality factor of the pickup coupler with varying antenna length. A length of 20 mm was chosen for the cavity cold tests.

## 4.8 Multipacting Studies

Multipacting is the process of periodic bombardment of the surface of an RF cavity due to ambient electrons being accelerated by the RF fields present within the cavity. These electrons experience a time varying force from the electric and magnetic fields of the operating mode, and because the RF fields within a cavity are oscillating, resonant trajectories can exist that repeatedly bring the electrons back to the same location on the cavity surface, or between two surfaces.

The impact of the electrons on the cavity wall can result in the release of multiple electrons from the surface that themselves can be accelerated by the cavity fields. The secondary emission yield (SEY) is a property of the surface material that quantifies

how many electrons may be released from a single impact event. A number greater than unity indicates a net increase in the number of electrons released from the surface. Besides the surface material, the SEY depends on the energy of the impact and on how the surface was prepared.

If present, multipacting can very quickly pull the energy out of the cavity, depositing it onto the surface during impacts. If the resulting heat load is high enough, this can quench the cavity. Multipacting can limit the field amplitude at which the cavity can be operated, as any increase in input power will simply go to accelerating the electrons taking place in the multipacting process. In some case, multipacting can be suppressed through RF conditioning of the surface. Conditioning is the process in which the continued bombardment of the cavity surface reduces the SEY at that location, to the point where the multipacting no longer occurs.

RF conditioning can be a very time consuming process, although once a multipacting barrier is *conditioned away* it generally does not come back until the vacuum is broken or some other change to the surface takes place. With modern simulation tools, the geometry can be studied to estimate how susceptible the cavity will be to multipacting, allowing for design changes to be considered that attempt to avoid the conditions leading to resonant trajectories. The accuracy of the results depends on the assumed SEY curve of the material, as well as the available computing power for calculating the solution. Multipacting simulations are commonly used during the design process and have been shown to accurately predict multipacting in RF structures [69].

Multipacting analysis of the geometry was carried out using TRACK3P, a particle tracking code in the ACE3P suite of finite elements codes [18]. In simulations of multipacting, electrons are tracked from their release from various surface locations throughout the cavity, initiated at different RF phases, and their trajectories tracked as they interact with the fields in the cavity over a number of RF periods. Resonant trajectories are identified, and using the SEY curve, it can be determined if they are at risk of multipacting.

The code was used to track electrons initiating from surfaces within one quarter of the cavity and over the whole surface of the couplers through 50 RF periods, identifying any particles that became trapped in resonant trajectories. These were defined as paths that repeatedly returned to the same surface location, or bounced between two surfaces, by the end of the simulated time scale. The impact energy of these resonant particles within the cavity are shown in Figure 4.28. The order refers

to the number of RF periods it takes for the electron to return to the surface.

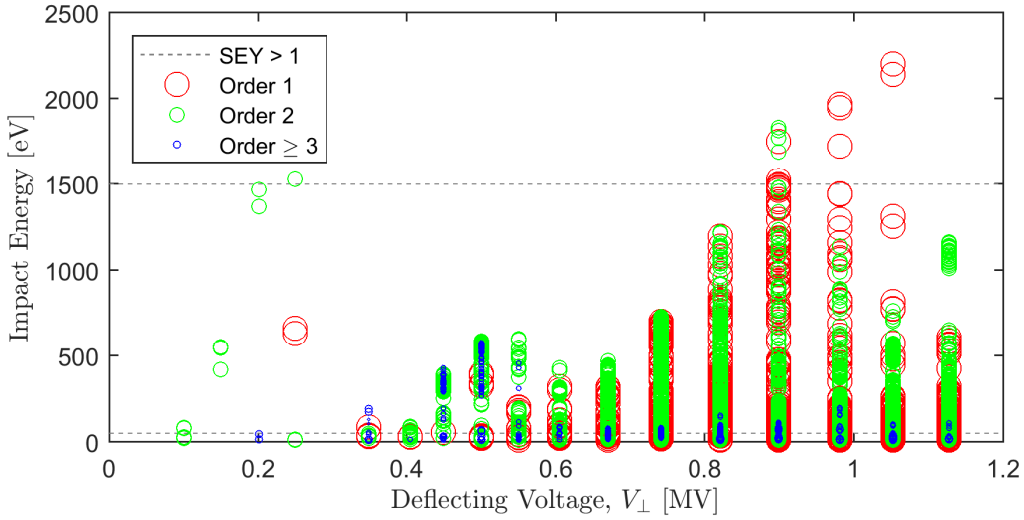


Figure 4.28: The impact energy of electrons trapped in resonant trajectories simulated at discrete cavity voltages. The area between the dashed lines indicate an SEY of greater than 1 for baked niobium.

Few resonant tracks were identified within the cavity below about 0.3 MV, increasing to local peaks at about 0.5 MV and 0.9 MV. These tracks were found to be located primarily on the outer cylinder of the cavity, around the ridges, as shown in Figure 4.29. The existence of resonant tracks with impact energies within the range where SEY $> 1$ indicates the potential for multipacting to occur within the cavity. Previous experience in cryogenic tests of the RFD and DQW cavities showed some multipacting during initial cold tests, although these were found to be fairly easily processed and were not seen again in later measurements [52, 70, 53]. Since the distribution of impact energies simulated in this cavity geometry show a similar trend to that reported in these other cavities, it was expected that multipacting would not pose a serious risk for this geometry.

## 4.9 Mechanical Design Considerations

### 4.9.1 Pressure Sensitivity

The cavity will be cooled during operation by being submersed in liquid helium at a temperature of 4.2 K and atmospheric pressure. Fluctuations in the bath pressure can

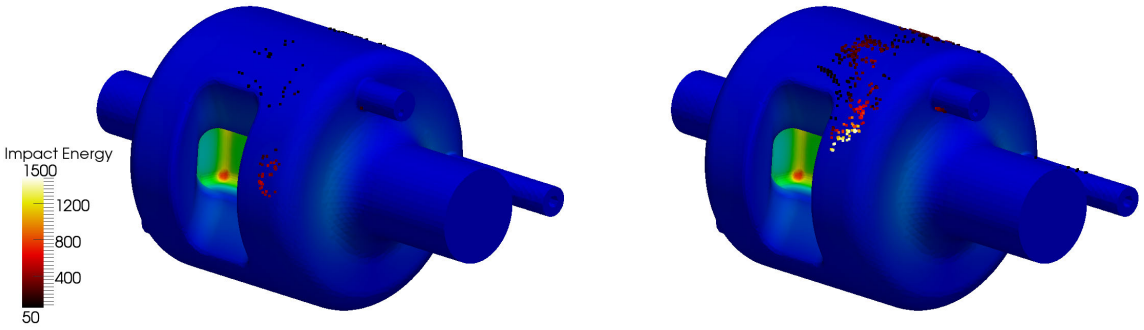


(a) (b)

Figure 4.29: The location of surface impacts for resonant tracks at a) 0.5 MV and b) 1 MV deflecting voltages. The intensity of the data points indicates the impact energy within the range where the SEY may be greater than 1 for baked niobium.

be caused by boiling helium and variations in the compressor and Dewar pressures in the cryogenics system. Experience with TRIUMF's ISAC II cryomodules, which operate at 4.2 K, shows fast oscillations of about 2 mbar in the pressure inside the cryomodule [71].

The pressure applied on the cavity from the helium bath deforms the cavity causing a small change to the resonant frequency. Fast fluctuations in pressure can result in changes to the frequency faster than can be compensated by an active tuning system. High $Q$ SRF cavities have a narrow bandwidth, with the power required to drive the cavity increasing substantially if the cavity is driven off its resonant frequency. With a loaded $Q$ of $3 \times 10^6$, the bandwidth of the 650 MHz cavity is 220 Hz. The goal pressure sensitivity must then be less than 10 Hz/mbar such that the changes in resonant frequency remain within 10% of the bandwidth under the 2 mbar fast pressure fluctuations.

The pressure sensitivity of the cavity was modelled using ANSYS APDL, allowing for coupled mechanical and RF simulations. The simulation determined the resonant frequency of the cavity before and after applying an external pressure to the outer surfaces of the cavity. An important boundary condition in determining the deformation of the cavity is how the cavity would be supported. The ends of the cavity could be allowed free motion, as they would be during a bare cavity test inside the cryostat, or fixed, as they would inside a cryomodule where they would be fixed to a rigid tuner.

Using standard fabrication techniques, the cavity would be made from niobium

sheet, resulting in a thin walled structure of typically 2 to 4 mm thickness. Under fixed beam pipe conditions, the cavity with 4 mm walls would exhibit a pressure sensitivity of 80 Hz/mbar. The large change in frequency is primarily due to the high sensitivity of the resonant frequency to the position of the ridges, which would be forced inwards by an external pressure. The inward motion of the ridge faces would result in a decreased frequency.

Various ways of supporting the ridge were modelled, such as adding more material to the high stress areas, adding bracing structures, or tying the ridge to the helium jacket. The most effective technique was to fabricate the entire ridge from solid niobium. The extra material on the ridges provided the required stiffness to decrease the pressure sensitivity to about 1 Hz/mbar with the remaining cavity walls set to 3 mm thick. The maximum stress in the cavity walls in this configuration was found to be 24 MPa with an external pressure of 1 atm. This is well below the yield strength of niobium at cryogenic and room temperatures. The simulated deformation and stress intensity of the thin walled and solid ridge cavities are shown in Figure 4.30.

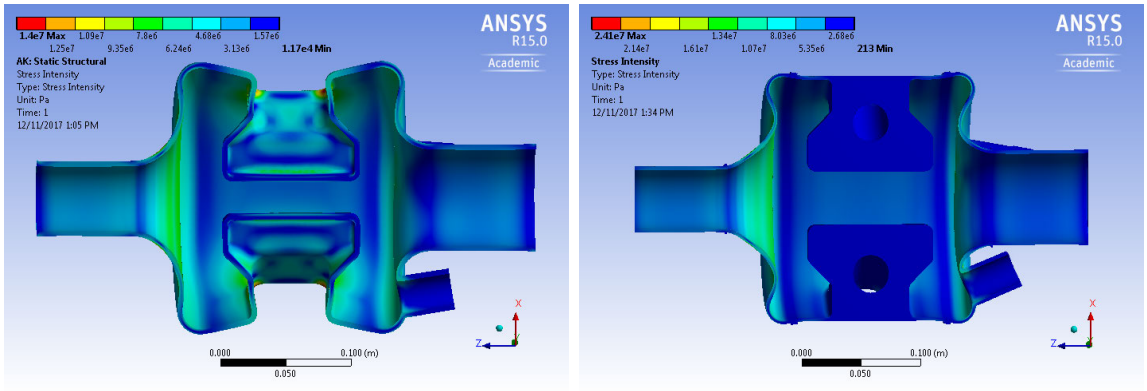


(a) (b)

Figure 4.30: The cavity response under 1 atm external pressure with fixed beam pipes for the a) 4 mm thin walled cavity, and b) 3 mm cavity with solid ridges. The deformation is shown by the deformed shape of the cavity, scaled by a factor of 1000, and colour indicates the stress intensity.

With the beam pipes free, the pressure sensitivity of the cavity with solid ridges decreases to 92 Hz/mbar. The cavity also sees an increase in the maximum stress on the cavity walls to almost 40 MPa in the end plates when evacuated. Plastic deformation of the copper prototype is observed when evacuated at room temperature, as this is above the yield strength for annealed copper. At room temperature, the yield strength of niobium is higher than this, although can be relatively close after

heat treatments [72].

A support frame was designed to be installed around the cavity during the cold test and during any room temperature evacuations of the cavity space. The frame provides the extra stiffness to the cavity to decrease the pressure sensitivity down to 13 Hz/mbar for testing, and removes the risk of deforming the cavity when pumping out the inner space. A summary of the simulated pressure sensitivity and maximum stress experienced by the cavity for the different scenarios studied are listed in Table 4.4. An image of the support frame installed on the cavity can be seen in Figure 5.24.

Table 4.4: The pressure sensitivity and maximum stress intensity on the cavity with 1 atm of external pressure.

| | $df/dp$ [Hz/mbar] | | Maximum Stress [MPa] | |
|---|---|---|---|---|
| Beam Pipe: | Fixed | Free | Fixed | Free |
| 4 mm thin wall | 80 | 60 | 14 | 26 |
| Solid ridge with 3 mm wall | 1 | 92 | 24 | 38 |
| Solid ridge with support frame | – | 13 | – | 20 |

### 4.9.2 Tuning

The ANSYS APDL simulation was also used to determine the tuning sensitivity of the cavity. Active tuning is required to compensate for frequency detuning that results mainly from helium pressure fluctuations, microphonics, or radiation pressure exerted by the fields within the cavity. The tuning sensitivity of the cavity is −380 kHz/mm with the frequency decreasing in tension. A tuning force of 5.4 kN is required to stretch the cavity by 1 mm. With a 1 mm deformation, the maximum stress intensity would be 270 MPa on the end plate of the cavity.

A conceptual design of a tuner was developed, based on the scissor-jack tuner used for the ARIEL accelerating cavities, which itself was based on the CEBAF scissor style tuner [73]. The tuner is driven by a warm motor, located outside of the cryomodule, that drives a vertical shaft up and down. The shaft transmits the drive force inside the cryomodule to a set of linkages that transform the vertical motion of the shaft to a horizontal force applied to the ends of the cavity. The concept is shown in Figure 4.31. The tuner is designed to apply a tuning force only while in tension so that there is zero backlash when the direction changes. To remain under tension over the entire tuning range, the relaxed frequency of the cavity is higher than the operating

frequency by roughly half the tuning range so that it can be pre-tensioned to the operating frequency.

The tuner will grasp the cavity by the outer rim of the helium jacket, to keep clear of the input and HOM couplers located on the upstream end plate of the cavity. Bellows will be installed on the helium jacket to allow the cavity to expand when a tuning force is applied. Bellows would also be used between the jacket and coupler ports to avoid twisting the cavity as it is tuned due to the non-symmetric port locations.

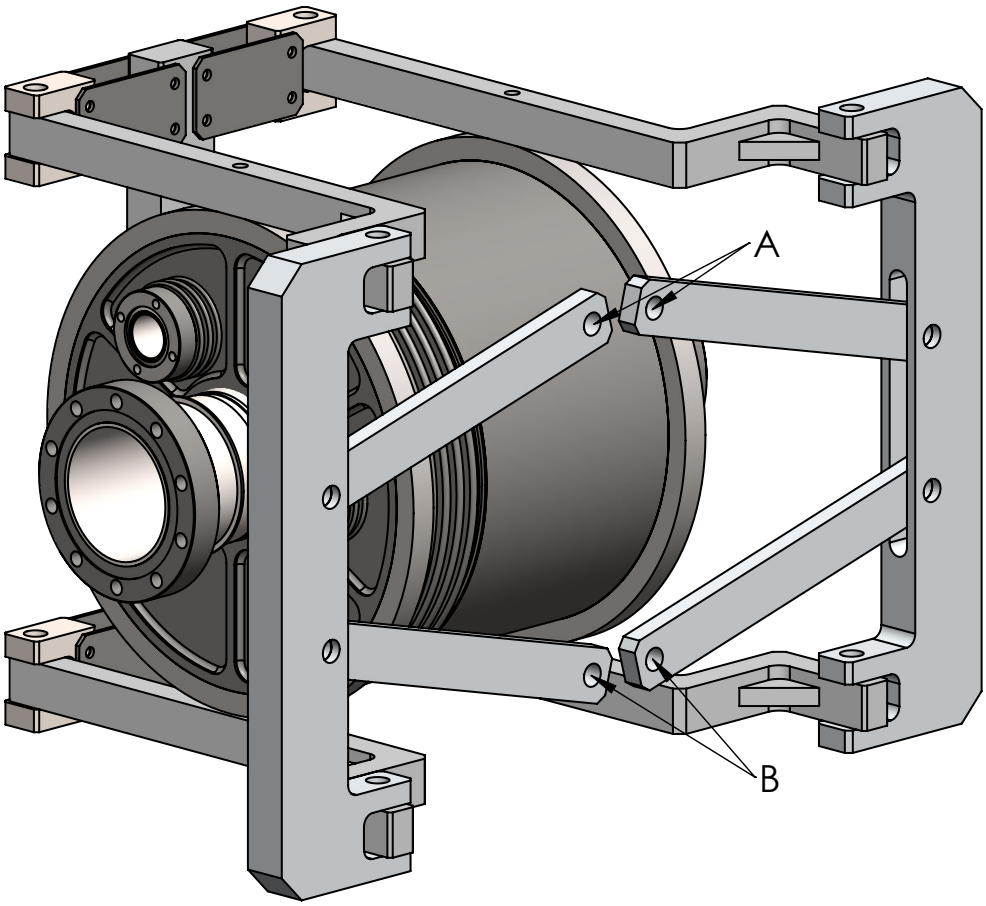


Figure 4.31: The conceptual design of a scissor jack tuner mounted to the jacketed cavity. Moving the points labelled A and B together will act to stretch the cavity. Solidworks model provided by Norman Muller.

### 4.9.3 Thermal Simulations

A thermal feedback model was developed, again using ANSYS APDL, to determine the equilibrium temperature of the cavity surface. The BCS component of the RF surface resistance depends on the temperature of the surface. As more power is dissipated, the assumption that the surface temperature remains constant becomes invalid. Of particular concern is the solid inner ridge that results in a large separation of the inner surfaces of the ridges and the liquid helium cooling bath.

The simulation works by starting with the entire cavity surface at the bath temperature and performing an RF simulation to determine the local power dissipation on the surface. This is followed by a thermal simulation that takes the power dissipated on each surface element as the heat load, and determines the static equilibrium temperature of the RF surface when the outer surface of the cavity is held at the bath temperature. The surface temperature distribution can then be used to calculate an updated local surface resistance on every surface element using a relation determined from the BCS resistance code [35]. A new heat load is determined from the increased resistance and this process is iterated until the change in surface temperature between iterations converges to within the desired accuracy.

Simulations were performed using the thermal feedback model at increasing cavity voltages until a point on the cavity reached the superconducting transition temperature, indicating at what fields the cavity may be operated before a quench will occur. However, this is a simplistic model and does not account for other effects that could initiate a quench such as magnetic quench or field emission induced quench, but allows for assessing the viability of fabricating the ridge from solid niobium.

Assuming a bath temperature of 4.5 K, a residual surface resistance of 20 n$\Omega$, and calculating the BCS resistance using $RRR = 45$, the maximum temperature reached on the cavity surface is only 4.56 K at the nominal operating voltage, as shown in Figure 4.32. A set of cooling channels were added to the ridges to allow the helium to cool closer to the ridge surfaces, but were found to have only a minimal effect on the temperature rise of the surface.

By the upper end of the operating range, 0.6 MV, the surface temperature only rises a further 0.2 K, but at this point, the increased heat load is enough to start decreasing the $Q_0$ of the cavity. Under these idealized conditions, the cavity would be expected to quench at a deflecting voltage of around 1.2 MV. The simulated $Q$-curve is plotted in Figure 4.33. The simulations were repeated with a bath temperature

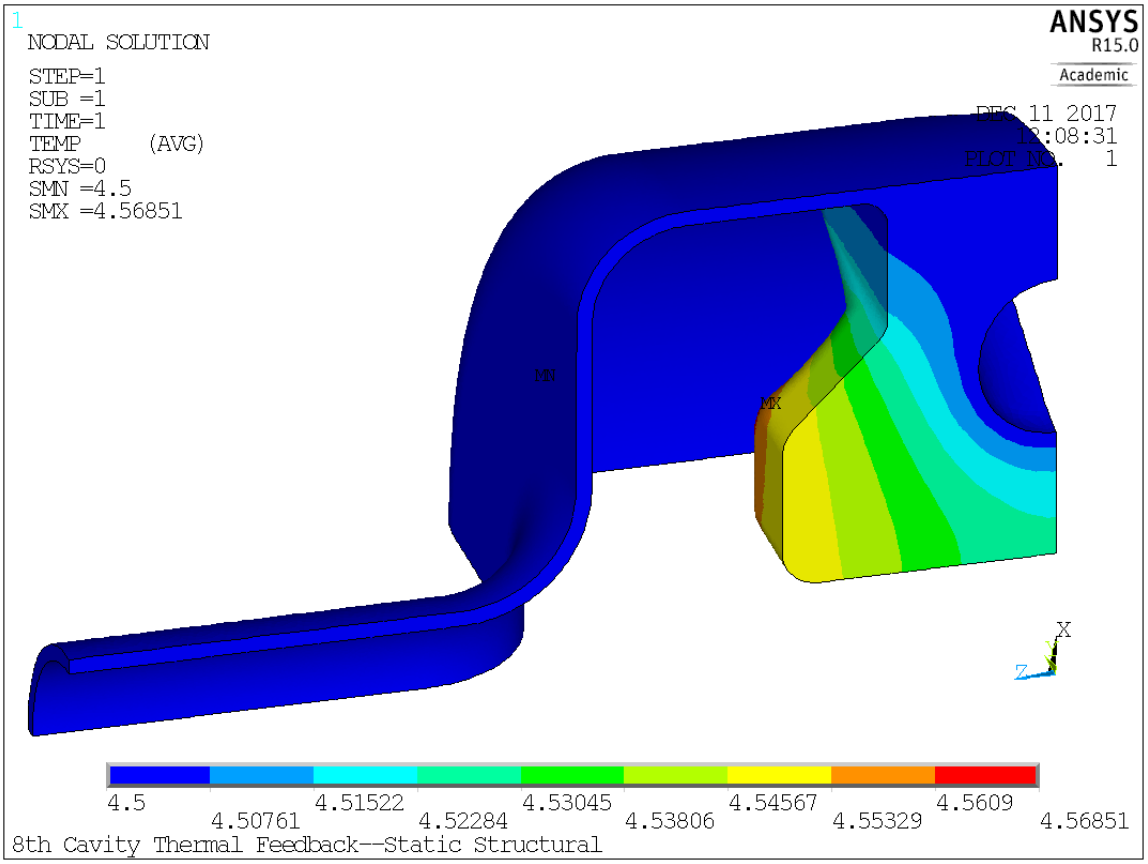


Figure 4.32: The temperature distribution across the cavity surface at a deflecting voltage of 0.3 MV and $RRR = 45$ material.

of 2 K. At this temperature, the BCS resistance is very low, allowing the cavity to reach much higher fields before the heat load would cause a thermal quench at about 2.5 MV.

The thermal feedback model was also used to determine the cavity response to a normal conducting surface defect. Defects of increasing diameter were placed on the cavity surface at the location of maximum magnetic field to determine at what size they would cause a thermal quench.

The cavity voltage at which the cavity would quench at 4 K with increasing defect sizes is plotted in Figure 4.34. Defects of up to 50 µm in diameter were found to have a negligible effect on the performance over the operating regime. With defects larger than 100 µm, the cavity could quench within the nominal operating regime. Care must therefore be taken during fabrication and preparations of the cavity for cold tests to ensure defects are not introduced onto the surface.

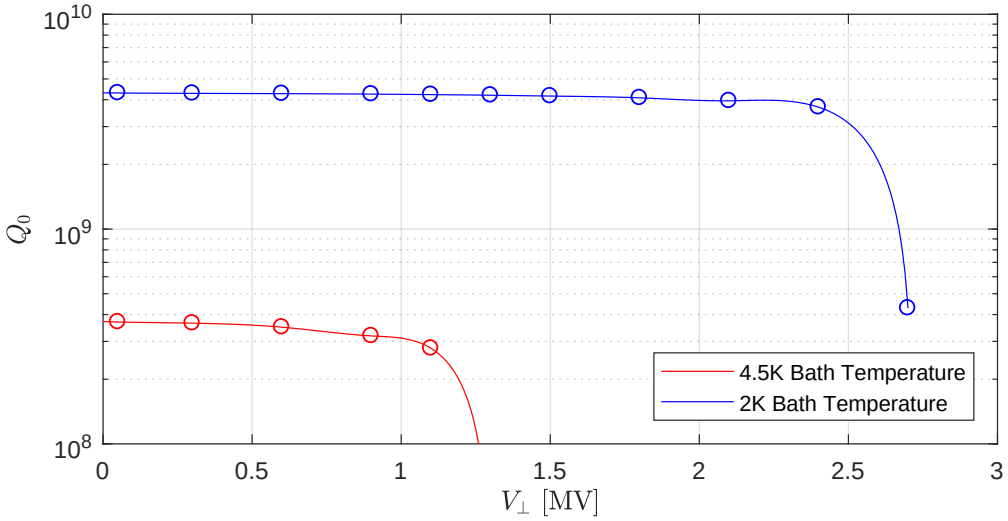


Figure 4.33: The simulated cavity response, taking the surface temperature into account.

The thermal simulations indicate that the cavity should operate across the nominal operating regime without risk of thermal quench. Fabricating the ridge from solid niobium is only expected to result in a small temperature rise of the RF surface, and the cooling channels allow for slightly improved cooling of the ridge. It is expected that the maximum field the cavity may be operated at will be limited by thermal quench due to the eventual temperature rise of the ridge.

## 4.10 Target Frequency

For the cavity to be able to reach the target operational frequency, a good understanding of the frequency changes throughout the fabrication and processing of the cavity is required. Simulation studies can help to set the goal room temperature frequency that will shift to the correct operating frequency when the cavity is in use on the beam line.

After the cavity is tuned at room temperature, it will undergo a chemical etch that will remove 120 µm from the surface. Ideally the removal is uniform, but complicating factors such as fluid flow and temperature will cause different areas of the cavity to etch at different rates. The etching process is difficult to model accurately, so the initial assumption is that the entire surface will experience the same removal. The shift in frequency was modelled in HFSS by adding a small layer onto the RF volume

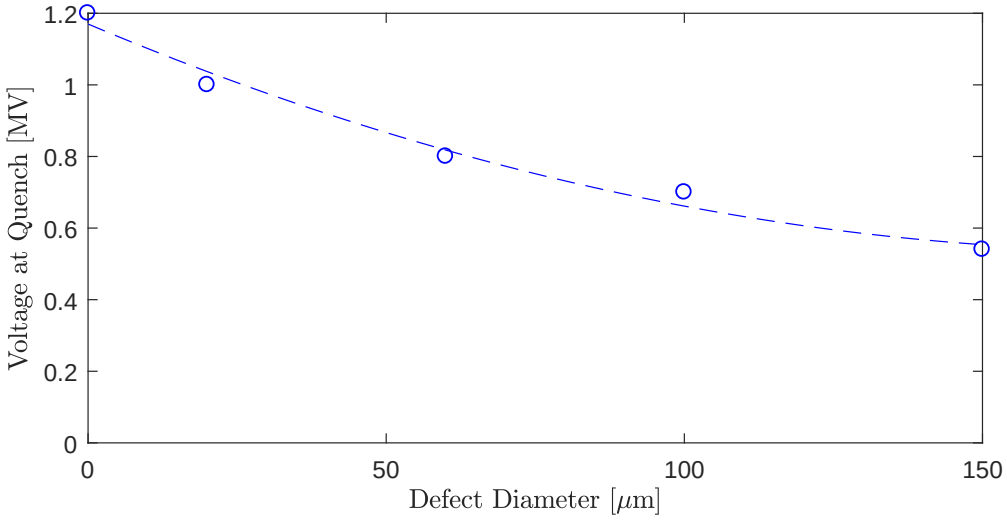


Figure 4.34: The simulated cavity response, with increasing normal conducting defect size on the cavity surface.

of the model and determining the resulting change in resonant frequency. Using the determined rate of change of the frequency with material removal, the estimated shift in the frequency due to a 120 µm etch is an increase of 96 kHz.

Evacuating the cavity space changes the frequency in two ways. The external pressure of the helium bath would result in only a 1 kHz increase in frequency. However, the change in relative permittivity of the RF space from air, at about 1.0007[1], to vacuum would cause the resonant frequency to change by about 230 kHz.

Thermal contraction of the cavity when cooling from room temperature to 4 K would also cause a significant frequency change. Rather than simulating this contraction, one can use the thermal expansion coefficient of niobium, integrated over the temperature change. The cavity size is reduced by a factor of 0.9986, increasing the frequency by 931 kHz. Finally, since the tuner can only apply force on the cavity in tension, the cavity is stretched through half of its tuning range, decreasing the frequency by $\sim$ 250 kHz.

Taking all of these frequency changes into account, as is summarized in Table 4.5, the goal room temperature frequency of the cavity was set to 649.01 MHz. The main uncertainty in this number is the frequency shift caused by etching. Further information can be gained by tracking the frequency changes during the etching process. Therefore, this room temperature goal can be updated and the cavity retuned by

[1] under typical Vancouver indoor conditions

plastically deforming the cavity after the initial cold tests are completed.

Table 4.5: The frequency changes from the bare cavity at room temperature, to the operational frequency.

| Step | Frequency Shift | Frequency |
|---|---|---|
| Operational frequency | | 650.000 MHz |
| Tuner tension applied | -250 kHz | |
| | | 650.250 MHz |
| Cooled to 4 K | +931 kHz | |
| | | 649.319 MHz |
| Cavity evacuated | +230 kHz | |
| | | 649.129 MHz |
| 120 µm uniform etch | +96 kHz | |
| Room temperature frequency | | 649.01 MHz |

# Chapter 5

# Fabrication

The fabrication of niobium cavities requires careful consideration of the techniques used to cut, form, and weld the niobium to ensure high performance of the finished cavity by avoiding procedures that can embed or dissolve contaminants into the material. Additionally, a high level of accuracy is required in producing the surface profile to accurately achieve the desired RF field profile and a smooth surface finish required to avoid increased surface fields due to local field enhancement.

The standard process to fabricate cavities starts with RRR grade niobium sheets, rolled to a few mm thick. These are stamped into shape through a process of deep drawing, where the sheets are pressed between the two sides of a die set that match the inner and outer profile of the part. This is a relatively quick process, and once the dies are created, can lead to the fast throughput of identical parts. Machining of components from bulk niobium may sometimes be performed, usually for a part with complex geometry. Although this method sees limited usage due to the cost associated with the amount of material wastage.

The shape of the ridges of the SRF separator cavity does not lend itself to be fabricated from sheet, due to the complex geometry and high surface angles of the ridges. For this reason, and to achieve the required rigidity of the cavity for pressure sensitivity, it was decided to machine the ridges from bulk niobium, rather than attempting a formed and welded structure that would require welds in the high magnetic field regions of the cavity. Due to the shape and size of the ridges, it was only marginally more costly to machine the entire cavity from bulk niobium, rather than machining only the ridges and forming the remaining components from sheet. Machining the ridges and outer cylinder from a single piece also reduced the total number of welds required and put them all in low field regions experiencing less than 4 mT magnetic

fields at the design deflection field.

To reduce the cost incurred from machining the cavity from bulk material, it was fabricated from lower purity, reactor grade niobium. This grade is roughly 1/3 to 1/2 the price of the RRR grade niobium that is typically used. It is possible to use this lower purity material due to the fact that the operating voltage of the cavity is relatively low, reaching peak fields of less than 20 MV/m and 24 mT, with the weld joints experiencing much less than this. To further reduce the manufacturing costs, the cavity was fabricated completely in house at TRIUMF using the available fabrication techniques.

The fabrication process will be described in the following sections, including fabrication of a copper prototype cavity, the development of the TIG welding procedure used for welding joints, and the post fabrication processes applied to prepare the cavity for SRF testing.

## 5.1 Copper Prototype

A copper prototype cavity has been fabricated to test the fabrication procedures and to allow for low power field measurements of the cavity geometry. The cavity was machined from solid copper in the same manner as the niobium cavity using wire EDM (electric discharge machining) and CNC milling. The machining accuracy from modern milling machines can easily reach better than 50 µm, so it is expected that the profile of the inner cavity surfaces match the ideal geometry used in the simulation tools with very good accuracy. The cavity components are brazed together instead of welded as the material properties of copper are different enough from niobium that useful information would not be gained through this part of the procedure. The completed prototype cavity is shown in Figure 5.1.

The prototype cavity also provided an opportunity to test the tuning procedure required to reach the goal room temperature resonant frequency. The centre body piece was intentionally made 15 mm longer than the design length to allow the frequency to be measured before trimming to the final length. Trimming was completed in several steps, with the frequency measured between each fabrication step to get the final fabricated frequency close to the goal frequency determined in Table 4.5.

During fabrication, the resonant frequency of the cavity was measured in an *RF stack-up*, where the components are stacked together in a jig that compresses the stack, ensuring good electrical contact between the parts. The jig was designed to

(a)

(b)

Figure 5.1: The prototype cavity fabricated from bulk copper. a) the end cap and centre body sub-assemblies, and b) the completed cavity.

compress uniformly on the end plates rather than on the beam pipe of the cavity to minimize deformation of the parts during the measurement. Tension is applied on the jig by four threaded rods, tightened to the same torque for every measurement. The resonant frequency was measured by a network analyzer (NWA) with antennas inserted into the input coupler and pick up ports.

The amount of material to trim is determined from RF simulations using HFSS, providing a sensitivity of around 1 MHz per mm removed, depending on the side of the cavity to be trimmed and how much material is being removed. The steps followed to reach the goal room temperature frequency are summarized in Table 5.1.

Table 5.1: The steps of the tuning procedure applied during fabrication of the cavity.

| | |
|---|---|
| 1. | All parts fabricated, with excess length on end caps and centre body. |
| 2. | Beam pipes and RF ports brazed/welded to end caps. |
| 3. | *Frequency measurement performed via RF stack-up.* |
| 4. | End caps trimmed of extra length. |
| 5. | *Frequency measurement performed via RF stack-up.* |
| 6. | Downstream end of centre body trimmed to compensate half of the frequency difference. |
| 7. | *Frequency measurement performed via RF stack-up.* |
| 8. | Downstream end cap brazed/welded to the centre body. |
| 9. | *Frequency measurement performed via RF stack-up.* |
| 10. | Upstream end of centre body trimmed to compensate remaining frequency difference. |
| 11. | *Frequency measurement performed via RF stack-up.* |
| 12. | Upstream end cap brazed/welded to centre body. |
| 13. | *Frequency measurement performed.* |
| 14. | Cavity is fine tuned to the goal frequency by plastic deformation of the cavity length. |

The tuning procedure was found to very accurately reach the goal room temperature frequency in the copper prototype. The frequency measurements, along with the trim amounts, are summarized in Table 5.2. After the brazing of the end caps was complete, the room temperature frequency of the cavity was measured to be only 100 kHz low, requiring only a small longitudinal deformation to reach the goal frequency. The degree of accuracy between the simulated and measured resonant frequencies throughout this procedure indicates that the amount of excess material

required could be decreased, resulting in a reduced cost of the bulk niobium to be ordered.

Table 5.2: The measured frequency of the copper prototype cavity throughout the fabrication process.

| Fabrication Step | Simulated Frequency (MHz) | Measured Frequency (MHz) |
|---|---|---|
| Initial RF stack-up | 634.90 | 635.25 |
| Upstream trim: 8.06 mm | 642.79 | 642.20 |
| Downstream trim: 7.54 mm | 649.06 | 648.96 |
| Tuned to goal frequency | 649.06 | 649.06 |

The field profile of the fundamental mode was probed using the bead pull technique, which will be described in more detail in Section 6.1. This method provides a measurement of the magnitudes of the electric and magnetic fields within the cavity. The electric field profile of the operating mode, measured along the cavity axis, is shown in Figure 5.2. These measurements are consistent with the simulated amplitude of the electric field calculated by HFSS, which is overlayed on the same plot. The frequencies and on-axis electric field profiles were also measured for all of the HOM's up to 3 GHz, with good agreement to the HFSS simulation results. The measured frequencies of the HOMs are within 0.2% of the simulated frequencies.

To confirm the pressure sensitivity of the cavity, the shift in resonant frequency due to pumping the RF space to vacuum was measured, resulting in an increase of 390 kHz if the cavity ends are left unsupported. Modelling this scenario in an ANSYS APDL simulation, considering the same boundary conditions, showed a similar shift of 330 kHz in frequency. The cavity was also determined to have experienced a small plastic deformation as a result of the pressure difference while under vacuum, resulting in a frequency shift of 10 to 20 kHz once vented back to atmospheric pressure. The cavity was heated to a high enough temperature during the brazing process that it became annealed, reducing its yield strength. While the yield strength of niobium is higher than annealed copper, the niobium cavity will only be pumped on while the beam pipes are supported to decrease the risk of plastic deformation.

The performance of the prototype cavity indicates the excellent accuracy of the machined RF surface profile and the robustness of the RF simulation tools. Based on these results, fabrication of the niobium cavity commenced with no significant changes to the design.

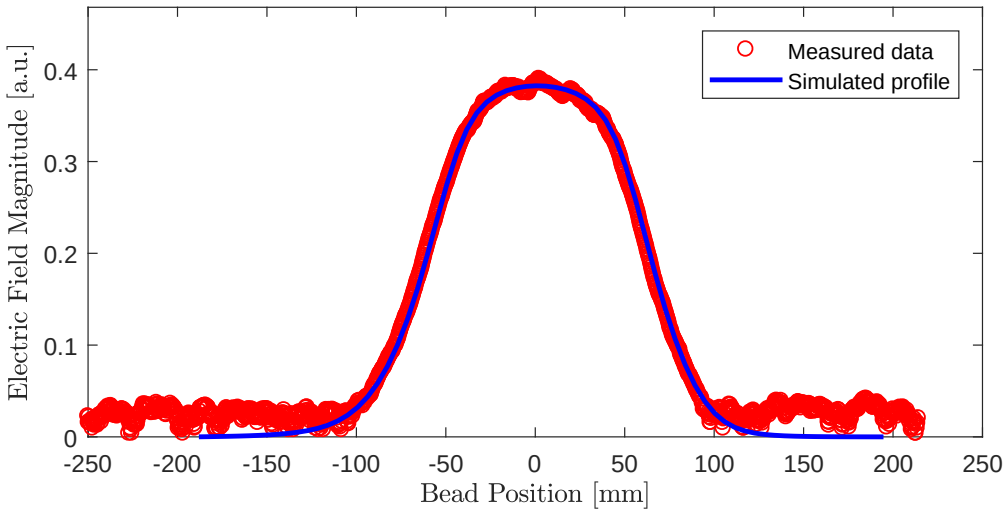


Figure 5.2: Comparison of the measured relative electric field along the beam axis of the copper prototype and the simulation results. The deviation from zero in the beam pipe is due to increased noise as a result of the relatively weak coupling used in this measurement. A more optimal choice of coupling and bead size were used when measuring the niobium cavity.

## 5.2 Fabrication of Niobium Components

The niobium cavity was fabricated using the same techniques as the copper prototype, with the exception of the welding. All components were machined from bulk niobium, using the wire EDM process to rough cut the profile, followed by standard machining techniques to yield the final geometry of the parts.

The usage of wire EDM for the fabrication of SRF components has been found to be very well suited for this application [74]. Cutting niobium by EDM has routinely been applied to SRF cavity fabrication, notably in the trimming of parts before welding and in the production of sheets from niobium ingots by slicing a large ingot into individual sheets that have been subsequently formed into half cells for elliptical cavity fabrication [75]. The EDM process results in good surface roughness when compared to other methods of cutting, but can leave an oxide layer formed due to arcing from the wire, and can introduce some contamination from the wire material. However, contamination introduced into the niobium through the EDM process is eliminated by a light BCP etching of the surface of about 5 µm.

Performing an initial rough cut of the niobium by EDM allowed the smaller components, including the RF tubes and beam pipes, to be machined from the offcuts

from the main body piece, decreasing the amount of required niobium, and the wasted material. The components were all cut from three niobium cylinders. The layout of the EDM cuts from these pieces are shown in Figure 5.3. In addition to cylinders being cut from the centre body piece to fabricate the beam pipes and RF tubes, cylinders were cut from the end caps from inside the beam pipe opening to save for test purposes.

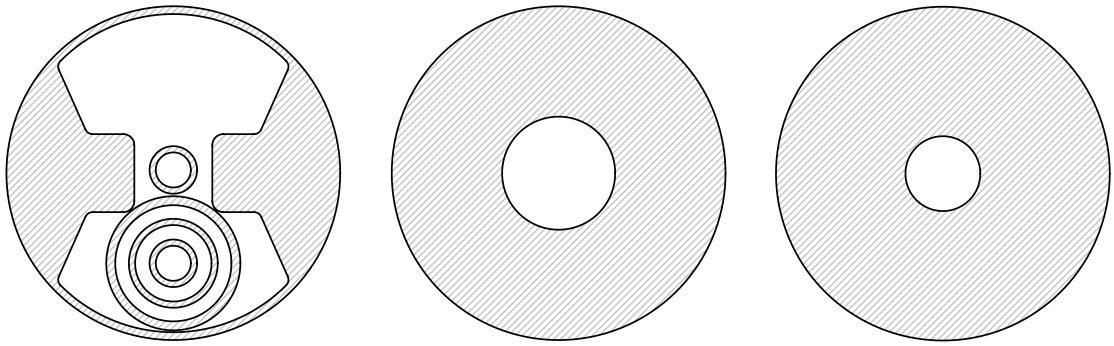

(a) (b) (c)

Figure 5.3: The layout of the EDM cuts made on the a) centre body piece, and b) and c) the upstream and downstream ends. The interior white areas are excess material, while the tubes were all cut from the excess material from within the body piece.

The niobium was purchased from Ningxia Orient Tantalum Industry Company in three cylinders of 214 mm diameter, with lengths of 135 mm and 56 mm for the centre body piece and two end caps. As discussed previously, reactor grade material was purchased to reduce the cost of the material. The $RRR$ of the niobium that was received was measured to be about 53, using the method described in Section 5.3.2.

After being rough cut by wire EDM, the final shape of the components was machined using CNC milling and lathe. The surface profile was machined to within 50 µm of the ideal design specified [76]. An initial rough cut was made using uncoated carbide tooling, leaving an excess of 125 µm for finishing. A final machining pass was made using ball endmills for curved profiles and sharp cornered uncoated carbide endmills for straight walls and flat surfaces to achieve as smooth a surface as possible. The surfaces were then hand polished to remove any remaining tool marks, finishing with ultra fine Scotch-Brite abrasive pads (grade ULF). Care was taken to ensure the temperature of the niobium stayed well below 150°C in all steps to limit the absorption of contamination into the niobium. Figure 5.4 shows some of the completed niobium parts.

(a) (b) (c)

Figure 5.4: A few of the niobium parts after machining. a) The centre body, b) the upstream end cap, and c) the upstream beam pipe and two RF ports.

An initial RF stack-up measurement of the unwelded components yielded a resonant frequency of 637.37 MHz, only 0.05% lower than the expected simulated frequency before trimming, indicating good machining accuracy of the components. This leads to a much more accurate reproduction of the surface profile than deep drawing due to the spring back of the niobium sheet after the pressure is released from the forming dies. In addition to the extra length added to the body piece for tuning during fabrication, the end caps were machined with all available length from the stock material to ensure excess length was available if required.

All parts were etched by 20 µm prior to welding to avoid introducing contaminants into the weld. After etching, the parts were rinsed and ultrasonically cleaned in deionized water before being allowed to fully dry in a clean room. The parts were held during welding using fixtures developed for each stage of welding. Figure 5.5 shows the parts assembled in the weld fixtures for the end cap welds and the final weld of the cavity. Niobium spacers were used in any place that the fixture had to touch the cavity directly, in case the high temperatures from welding caused the cavity to stick to a spacer.

The fixture used to hold the cavity together for the final welds contains a large

(a) (b)

Figure 5.5: The weld fixtures used during welding the cavity: a) the end cap fixture, shown on the upstream assembly, and b) the fixture used for the final welds.

spring to apply the compression required to hold the parts together. The goal of the spring is to minimize the shrinkage of these welds by allowing the material to expand more freely when heated, rather than compressing and resulting in decreased length of the cavity when the material cools.

The tuning procedure developed on the copper prototype was applied to the niobium cavity. The end cap assemblies were welded before trimming to their design dimensions, to account for deformation from the heat of welding the beam pipes and RF ports. Table 5.3 shows the progression of trimming and cavity frequency throughout the fabrication process.

Table 5.3: The frequency measured throughout fabrication of the niobium cavity.

| Fabrication Step | Simulated (MHz) | Measured (MHz) | Difference (kHz) |
|---|---|---|---|
| Initial RF stack-up | 637.67 | 637.33 | -340 |
| End caps welded | 637.67 | 637.58 | -90 |
| RF surface polished | 637.67 | 637.65 | -20 |
| End caps trimmed | 643.20 | 643.09 | -110 |
| Downstream trim 3.05 mm | 646.15 | 646.13 | -20 |
| Downstream welded | 646.15 | 646.13 | -20 |
| Upstream trim 3.05 mm | 649.06 | 648.97 | -90 |
| Upstream welded | 649.06 | 649.30 | 240 |
| Tuned to goal frequency | 649.06 | 649.07 | 10 |

## 5.3 TIG Welding

SRF cavities are typically fabricated using the process of electron beam welding (EBW) to join parts together. In the EBW process, the weld is performed in a high vacuum environment using an electron beam impinging on the joint to melt the material and form the weld. Welding under vacuum is required to avoid impurities diffusing into the heated niobium that would degrade its purity and reduce the *RRR* near the welded region. EBW has been used very successfully for the fabrication of niobium SRF cavities for many years and can achieve nearly no degradation in the purity of the material in welded joints when welded under sufficiently high vacuum.

However, the process of EBW is time consuming and costly due to the high cost of electron beam welding equipment and operators, and generally requires contracting this stage of the fabrication to one of a relatively small number of EBW vendors operating worldwide.

A potential alternative to EBW is Tungsten Inert Gas (TIG) welding that can be performed using conventional welding equipment within an inert gas environment rather than under vacuum. TIG welding would allow much more widely available welding equipment to be applied to SRF cavity fabrication and significantly decrease costs and fabrication times. Additionally, while the TIG welding process may be automated, similar to EBW, it can also be performed by hand, allowing better control and manoeuvrability to weld complex geometries or to perform repairs.

TIG welding for SRF cavities has been previously investigated at NSCL as an alternative to EBW [77]. A single cell elliptical cavity was fabricated by TIG welding

inside of an argon filled bubble chamber. This cavity showed only minor degradation of its quality factor compared to a cavity fabricated by EBW, but suffered an early quench. The performance of the TIG welded cavity motivated further systematic study of the effect of the environmental conditions on the quality of the welds using a more advanced welding system. Niobium coupons welded within an extremely pure argon environment were found to experience very little degradation in purity.

TIG welding uses a tungsten electrode to produce a welding arc between the electrode and weld joint by applying a high voltage difference between the electrode and the work piece. The welding arc delivers heat to the joint, melting and fusing the material together. A typical TIG welding setup is shown in Figure 5.6.

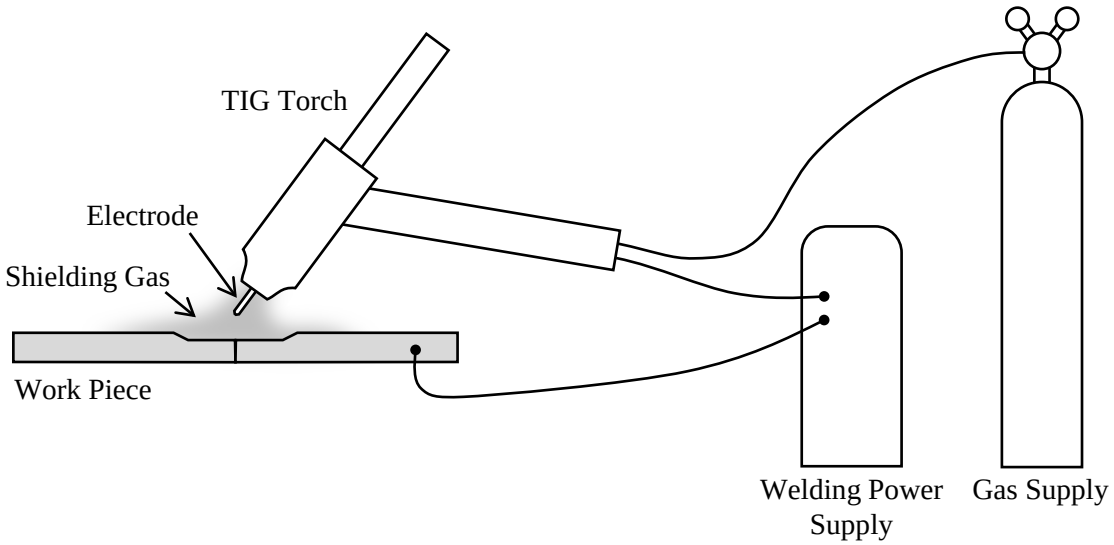


Figure 5.6: The typical TIG welding setup.

The electrode is made from tungsten so that it can withstand the high temperatures involved. Tungsten, with a melting temperature of 3422°C, has the highest melting temperature of all the pure elemental metals and almost 1000°C higher than niobium. The electrode therefore loses very little material during the welding process, reducing the contamination of the weld. The electrode and weld area are shielded from the air by flowing an inert gas such as argon or helium around the weld area to avoid oxidation or atmospheric contamination of the electrode and heated material.

The tungsten electrode is held by a TIG torch that provides the connection to the welding power supply and delivers the shielding gas to the welding area. However, the torch alone is not able to provide a pure enough environment at the weld location to weld niobium without degradation. To sufficiently shield the welded niobium from

air, the weld is required to be performed inside a chamber containing a high purity inert gas such as argon. At TRIUMF, this was achieved by welding within a glove box, as shown in Figure 5.7.

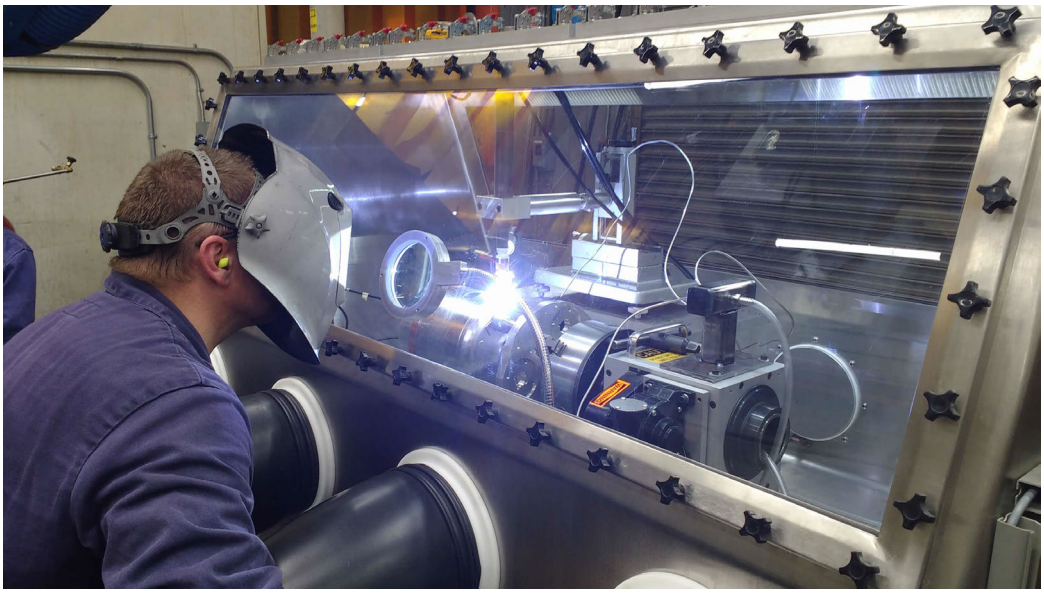

Figure 5.7: The glove box used for cavity fabrication. Pictured here is the welder, Neil Thiem, performing the final weld on the separator cavity.

Studies performed on the vacuum requirements for performing EBW have shown that a pressure remaining in the welding chamber of $5 \times 10^{-5}$ mbar is generally sufficient to limit the degradation of niobium during welding through the absorption of contaminants in the environment [78]. If the gases remaining in a vacuum chamber after pumping down are assumed to have similar composition to standard air, this corresponds to a partial pressure of oxygen of about $1 \times 10^{-5}$ mbar of oxygen. At atmospheric pressure, a 10 ppm concentration of oxygen inside a chamber purged with argon would result in a similar oxygen partial pressure. This sets the approximate scale that is required for the purity of the welding environment.

The following sections will describe the studies performed to characterize the TIG welding process, and the parameters used in welding the cavity. This work builds upon the work presented in [77] to apply TIG welding to the production cavity intended for installation in e-Linac.

### 5.3.1 Characterization of Niobium TIG Welding

Weld coupon studies were performed to determine the reduction in the purity of TIG welded niobium as a result of the diffusion of contaminants from the surrounding environment into the weld. Niobium samples of both RRR grade and reactor grade material were cut from 2 mm thick sheet into strips 12 mm wide and about 75 mm long to be welded together. All samples received a 20 µm etch prior to welding.

These samples have been welded in a glove box purged with high purity argon under different oxygen concentrations. The oxygen concentration was monitored by a GE O2X1 oxygen transmitter sensor [79]. The sensor measures the oxygen concentration over the full range from atmospheric concentrations down to a scale of 0–100 ppm with a reported accuracy of ±1 % of the measurement scale. This sensor was found to require a relatively long time to provide a stable measurement after being exposed to a higher oxygen concentration. Using a calibration gas mixture with concentration 70 ppm, the sensor was determined to read approximately 10 % high after being exposed to the calibration gas for a period of several hours.

The glove box is purged with ultra high purity argon (grade 5.0UH) with a purity of better than 99.999% and containing less than 2 ppm oxygen. Before reaching the glove box, the gas is passed through a filter and fed into the chamber continually through an inlet on the side of the chamber. The weld joint is additionally flushed directly on both sides of the weld through both the TIG torch and additional gas lines directed at the weld. This ensures the highest possible purity of the gas surrounding the location of the weld and helps to drive off any material that is evaporated during the weld. The gas leaves the glove box through an outlet located on the top of the enclosure fitted with a gravity operated valve. This allows the gas to be released when the glove box is slightly over pressure when the gas is flowing into the chamber, but closes when the input gas is turned off to seal the chamber.

After a weld is completed, the joint is continually flushed by argon through the torch for about 5 minutes while the coupons cool. The coupons are allowed to cool completely before being removed from the inert environment for further testing.

To determine the degradation of the welded material, the $RRR$ was measured after welding and compared to the $RRR$ of the material the coupons were cut from. The welded coupons are trimmed to a width of 5 mm centred on the weld joint to ensure the $RRR$ that is measured is reflective of the welded material.

### 5.3.2 Residual Resistivity Ratio Measurement

Measurements of the *RRR* are made using DC measurements of the voltage drop across a small sample at room temperature and cryogenic temperatures. The widely accepted definition of *RRR*, defined in Equation (3.22), is the ratio of the resistivity at 300 K to the normal conducting resistivity at 4.2 K. Since niobium is superconducting below 9.2 K, a number of measurement techniques have been developed to extract this value, as summarized in [80], including extrapolating the curve from measurements above 9.2 K, or suppressing the superconducting behaviour with a strong magnetic field.

Since the interest of this study is mainly the degradation of the material due to welding and not the absolute value of the *RRR*, the measurements made here were taken just above the superconducting transition, at about 10 K, to simplify the measurement. Therefore the *RRR* values reported here are defined as

$$RRR = \frac{\rho_{300K}}{\rho_{10K}}. \tag{5.1}$$

The *RRR* measured this way yields values roughly 10 % lower than using the measurement at 4.2 K.

The four-wire resistance measurement technique is used to measure the resistance of the niobium sample, using two pairs of leads in contact with the sample, as sketched in Figure 5.8. The outer two wires apply a constant current through the sample while the inner wires probe the voltage difference between the leads. By taking the room temperature and cold measurements without adjusting the setup between, the geometry and applied current remain consistent between measurements, assuming thermal contraction is negligible. In this case, the resistivity is proportional to the measured voltage, and the *RRR* may be taken as the ratio of the voltage measurements.

$$RRR = \frac{V_{300K}}{V_{10K}}. \tag{5.2}$$

To compensate for voltage drift induced by thermal gradients within the measurement setup, the current is applied across the sample as a 1 Hz sinusoidal waveform. This allows for a Fourier transform to be used to extract the voltage amplitude at the frequency of the current source, removing the effect of voltage drift and thermoelectric voltage. Even though an alternating current is being used, this is still a DC measurement as the frequency is low enough that the DC resistance is being sampled

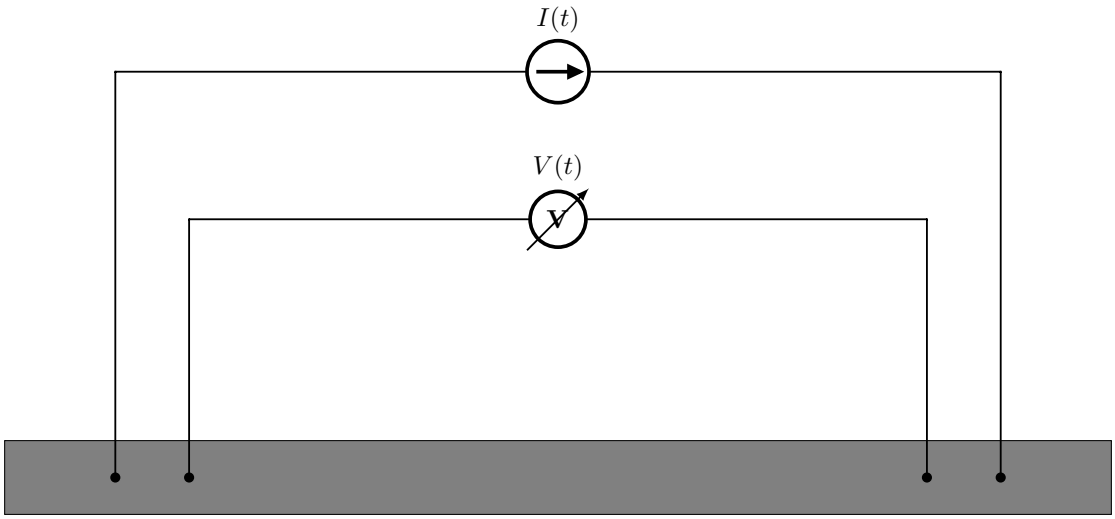


Figure 5.8: Schematic diagram of the four-wire measurement technique.

as opposed to the RF resistance.

A custom made voltage controlled bilateral current source is used to generate the current to be applied across the niobium samples. The current source supplies a maximum of 500 mA, producing a voltage difference between the voltage pick-ups of the four-wire setup of around 200 µV at room temperature. Just before the superconducting transition, the voltage reduces to as low as 500 nV.

To amplify the voltage from the sample, a two stage differential amplifier with low pass filtering characteristics provides a gain of about 5000 to the signal before being measured by an Agilent 35670A Dynamic Signal Analyzer. The Fourier transform of the voltage time series allows for the extraction of the voltage amplitude at a frequency of the current source.

The samples are cooled in a gas flow cyrostat that is primarily used for TRIUMF's µSR experimental program. The cryostat provides the fine control of the temperature required to make the measurement just before the superconducting transition. While a temperature probe is included on the sample holder, the superconducting transition provides a more consistent indication of the temperature of the sample. Figure 5.9 shows examples of the voltage time series acquired at different temperatures for a reactor grade sample.

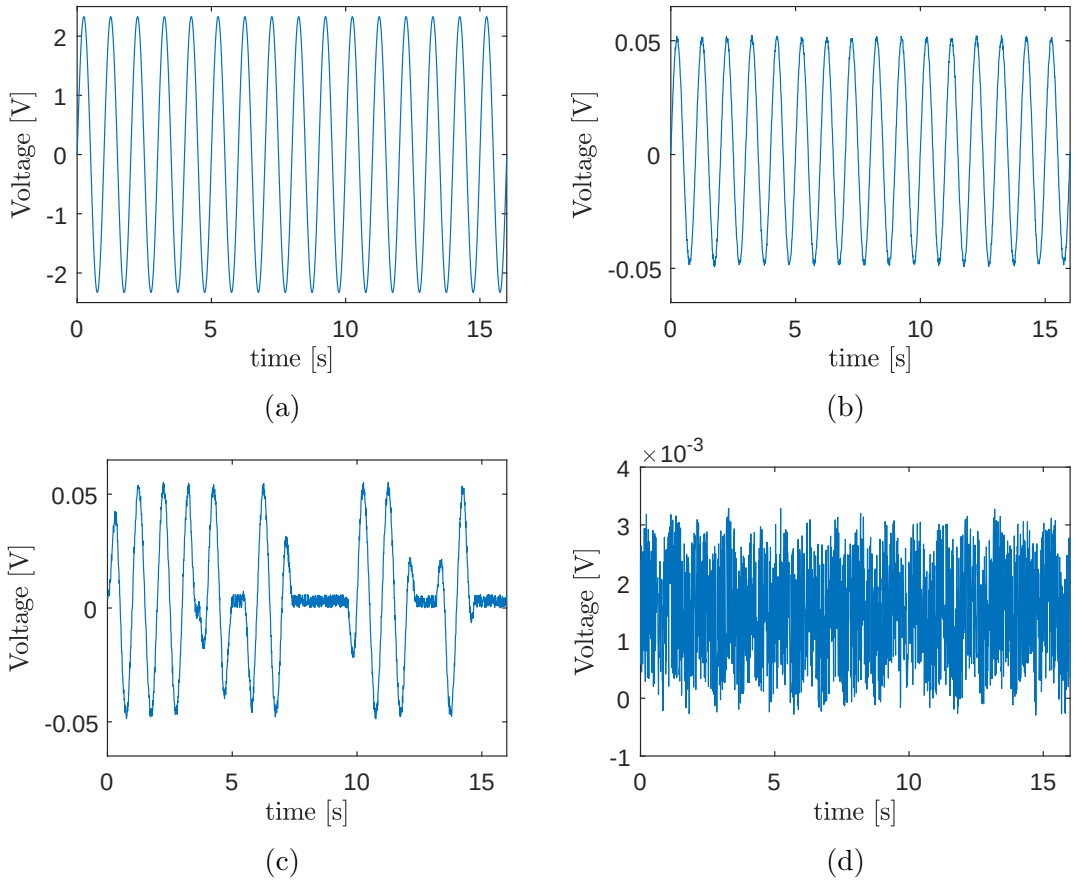


Figure 5.9: Examples of the voltage time series measured at different stages of the measurement process: a) at room temperature, b) just above the superconducting transition, c) while the sample is transitioning to the superconducting state, and d) completely superconducting. The *RRR* of the sample measured here is 48.

### 5.3.3 RRR Measurement Results

Figure 5.10 shows the voltage measured as a function of temperature across unwelded samples of RRR and reactor grade niobium. The room temperature resistivity of niobium is the same for the different grades, so would read the same voltage for samples with the same dimensions and placement of the voltage probes. The resistivity of the two grades start to diverge at temperatures below about 50 K. The non-zero voltage measurements at temperatures below 9.2 K are a result of noise and cross talk between the current leads and voltage probes.

The *RRR* measured from the unwelded materials is 283 for the RRR-grade material, and 48 for the bulk reactor grade material that the cavity has been fabricated from. Correcting for the measurement temperature, the true *RRR* of the cavity ma-

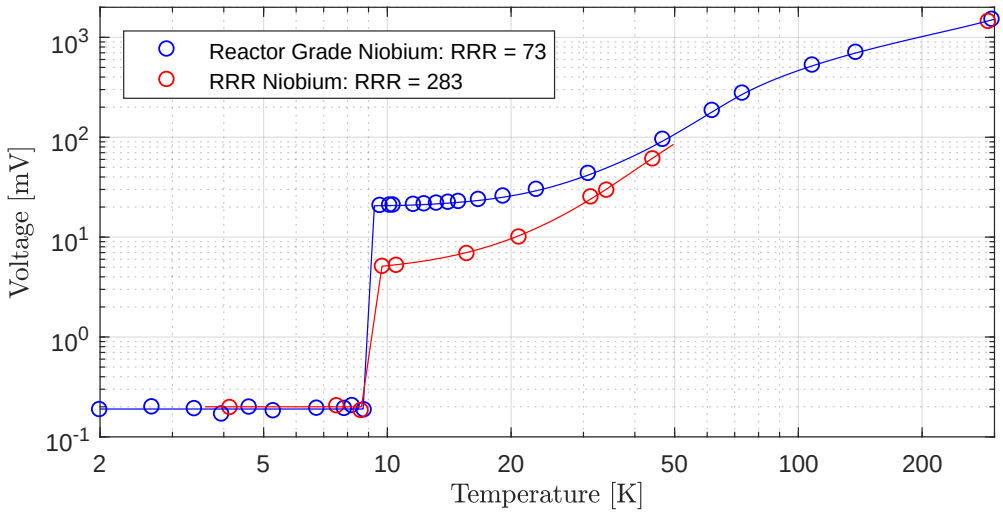


Figure 5.10: The voltage measured from unwelded samples of RRR and medium purity reactor grade niobium from room temperature to below the superconducting transition.

terial is approximately 53.

The results of the *RRR* measurements are summarized in Figure 5.11 for single pass welds performed with different oxygen concentrations in the glove box. A relative decrease in the *RRR* indicates degradation caused by the welding. The reactor grade niobium was found to be less sensitive to welding than the RRR grade niobium. For the welds performed with less than 10 ppm oxygen, the RRR niobium is degraded by about 25%, while the reactor grade samples see only a 15% reduction.

Also plotted here are the results achieved by Compton *et al.* in [77] in their previous work TIG welding niobium coupons. Note the similar trend between *RRR* and oxygen concentrations, but shifted to lower oxygen concentrations, indicating that to achieve the same amount of *RRR* degradation, their setup required approximately 100 times lower measured oxygen content.

The main difference between these studies is the configuration of the weld chamber. The glove box used in [77] was a re-purposed vacuum vessel that allowed the chamber to be pumped down to vacuum before filling with argon to reduce the volume of argon required to purge the chamber. The gas in the system was recirculated through an oxygen scrubber to filter out impurities before feeding it back into the chamber. This allows the chamber to reach very low oxygen concentration after many cycles of filtering the gas within the system, achieving below 30 ppb oxygen content. The

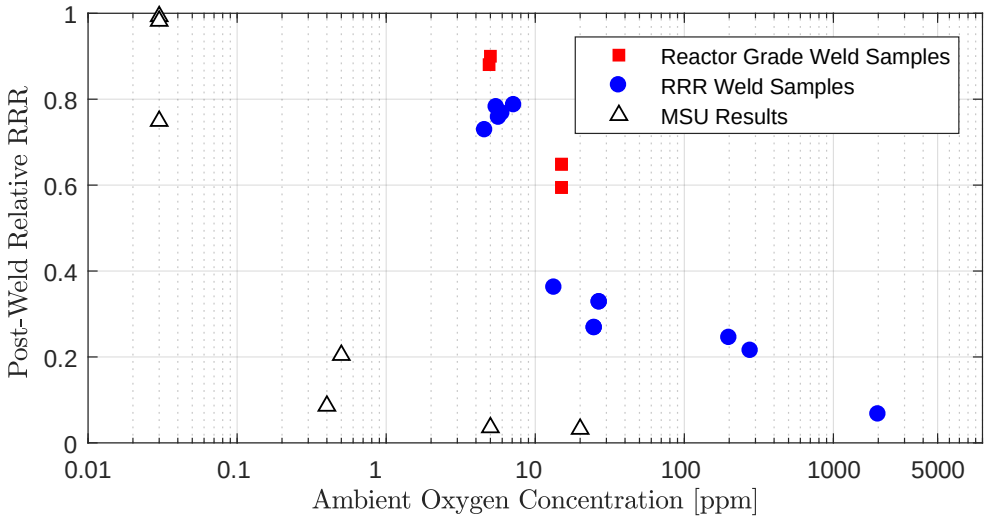


Figure 5.11: The *RRR* measured after TIG welds performed in the glove box with different ambient oxygen concentrations, relative to the pre-weld *RRR*. Results from [77] are plotted, which require much lower oxygen concentration to reach the same post weld *RRR*.

recirculated gas was also used to purge the weld joint during welding.

The glove box used at TRIUMF is a standard non-recirculating glove box where the gas flows into the chamber through a main inlet as well as being fed directly onto the weld samples, and is vented out the top. Since the inlet for the oxygen sensor is located on the top of the weld chamber, fairly far away from where the welding takes place, it is possible that the oxygen concentration at the location of the weld is in fact lower than is being measured. Since the chamber was being purged with grade 5.0UH gas, the minimum oxygen concentration is unlikely to be much lower than 2 ppm at the weld.

Other gases present in the chamber besides oxygen such as hydrogen and nitrogen can also contribute to the contamination of the welds. However, as only the oxygen concentration is measured, the differences in other impurities between the two setups is not known. The different approaches used to supply gas into the chambers could lead to different concentrations of these additional impurities. For example, the filtration system used by Compton *et al.* may not have removed these other gases as efficiently as it removed oxygen, leading to a higher concentration of other impurities than is present in bottled argon.

Further uncontrolled differences between setups could also contribute to the different results, such as the flow rate of the purging gas near the welding arc, welding

technique, or the burn-off rate from the TIG electrode. However, the large discrepancy in the required oxygen concentration achieved here compared to that reported in [77] is not fully understood. This indicates the importance of performing weld coupon studies to qualify a new welding environment, determining the oxygen concentration level required to achieve good quality welds for a particular welding setup.

Additional studies were performed to determine the effect of welding the same location twice, as is required at the end of weld, or if a section requires re-welding. These tests indicate that welding a material twice would effectively double the degradation. RRR-grade niobium coupons welded once saw a degradation of $\sim 25\%$ in measured $RRR$, and $\sim 50\%$ degradation when welded twice in the same oxygen concentration environment. Since the degradation in $RRR$ is being attributed to the introduction of impurities into the niobium during welding, as per Equation 3.24, this result is as expected since welding the same area twice will result in twice the impurities being absorbed, and therefore twice the reduction in $RRR$.

The best results achieved here show a $10 - 15\,\%$ reduction of $RRR$ for reactor grade niobium and $20 - 25\,\%$ reduction for high purity niobium, welded in $5 - 10\,$ppm oxygen concentration. Decreasing the oxygen concentration should further decrease the degradation of $RRR$, but this was not tested with this set-up due to the length of time required to purge down to less than 5 ppm oxygen content. These results indicate that the cavity can be TIG welded with sufficiently negligible degradation of the $RRR$ of welded reactor grade niobium in an argon environment with below 10 ppm of oxygen, with the present apparatus.

To further these studies, a number of changes to the apparatus are proposed. A smaller volume glove box would require less gas to purge down the chamber while an airlock would allow parts to be easily transferred in and out of the chamber without the need to vent the entire space. To reach lower oxygen concentrations, a recirculated gas system with an oxygen scrubber could be used once the first purge of the chamber is complete to more economically rid the chamber of trace amounts of oxygen. Additionally, if the assumption about the local oxygen concentration at the weld location being different from the measured oxygen concentration is correct, using a higher purity of argon such as grade 5.5 or 6.0, for purging the welded regions during welding could result in less degradation of $RRR$.

### 5.3.4 Weld Parameters

Two different types of welds were performed on the cavity based on the weld locations and their accessibility. Welds between the cavity end caps and the RF ports and beam pipes were performed from the inner surface, allowing for better access to the weld joints and eliminating the need for full penetration welds at these locations. For the final two welds on the cavity, joining the end caps to the centre body piece, fully penetrating welds were required to achieve a welded seam on the inner RF surface of the cavity. The different welds each have different weld preparations, as summarized in Figure 5.12, and require slightly different welding parameters.

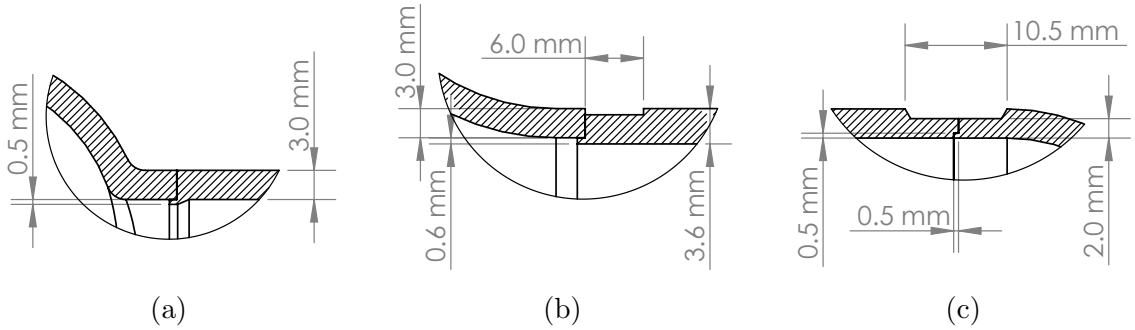


Figure 5.12: The weld preps on the a) RF ports, b) beam pipes, and c) full penetration welds on the cavity body. The surface welds performed on the RF ports and beam pipe require only a small step to aid in alignment of the parts and the TIG torch. For the full penetrations welds, the material is thinned to 2 mm to limit the heat required to weld through the thickness.

The welds joining the RF ports and beam pipes to the end caps were performed by hand and on the inner surface of the cavity. A small step on the weld prep ensured the correct positioning of the components relative to each other and aided the positioning of the TIG welding torch during the weld. These weld preps were mostly consumed by the weld, leaving behind only a small deviation from the ideal surface. In test pieces, the penetration of these welds were found to be 50 – 80% of the way through the 3 mm wall thickness. Stitch welds were performed on the outside of the cavity to ensure the strength of these joints. Since the fields at the locations of these joints are all very low, less than 1 mT, the welds between the end cap and tubes were performed with between 10 – 20 ppm oxygen in the chamber.

The final two welds performed on the cavity join the completed end cap assemblies to the cavity body. These welds are the most critical in terms of their location and their relative inaccessibility after welding. The joint between these parts must be

welded from the outside of the cavity and requires the weld to fully penetrate through the material to avoid leaving a gap on the RF surface.

Significant development went into determining the optimal parameters for this weld. Tests were performed on offcuts of the reactor grade material machined into tubes of 60 – 70 mm diameter. The test pieces were pressed together with copper cylinders that acted as heat sinks to more closely represent the thermal mass of the cavity.

The material is thinned to 2 mm in thickness at the location of the weld to limit the amount of heat required to fully penetrate the material. Again, an interlocking feature is included to ensure the correct positioning of the components. The 0.5 mm overlap is smaller than the width of the weld bead and therefore is fully melted during welding.

Test welds were performed at different peak welding currents to determine the lower limit of the current required for full penetration and the upper limit that would not cause a *blow through*, where the material at the weld location is melted away, leaving a hole behind. It was determined that although this range is sufficiently large, it varied between the different test pieces. This result indicated the need to test the weld parameters on the cavity itself to ensure full penetration before committing to the full circumferential weld.

Therefore, a ∼50 mm section of the weld was performed on the cavity and inspected using a boroscope camera inserted into the cavity to image the inner surface of the resulting weld. The cavity remained sealed in the glove box throughout this procedure to decrease the risk of contaminating the weld area. The test weld was found to be fully penetrating, as shown in Figure 5.13, with a width of the under-bead of ∼ 8 mm, indicating acceptable weld parameters.

The settings used to weld both the surface and full penetration welds are summarized in Table 5.4. Lanthanated tungsten electrodes are used as they are rated to carry the highest current and exhibit the lowest burn loss rate of currently available TIG electrodes. The burn loss rate is an important parameter to avoid the contamination of the weld with material from the electrode. Additionally, the electrode tip is blunted to avoid its over-heating and the loss of material.

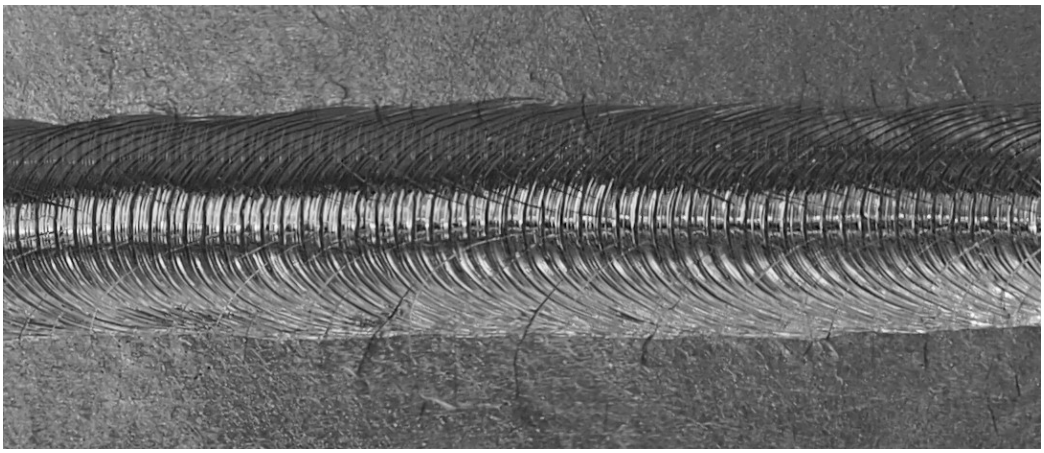

Figure 5.13: Boroscope image of the inner weld seam from the test weld section of the full penetration welds on the cavity.

Table 5.4: TIG welding parameters for surface and full penetration welds.

| Parameter | Surface Weld | Full Penetration Weld | Unit |
|---|---|---|---|
| Peak amperage | 230 | 240 | A |
| Pulses per second | 4.8 | 6.2 | $s^{-1}$ |
| Time at peak amperage | 60 | 60 | % |
| Amperage at background | 50 | 50 | % |
| Starting amperage | 10 | 10 | A |
| Time at starting amperage | 200 | 200 | ms |
| Time to peak amperage | 250 | 250 | ms |
| Speed | *varied* | 2.4 | mm/s |

## 5.4 Niobium to Titanium Welds

The cavity also requires welds between niobium and the Grade 5 titanium of the cavity flanges. Due to their size and cylindrical symmetry, these welds were all performed by EBW, in a small electron beam welder on site. The welding of dissimilar metals is complicated by many factors, including the different melting temperatures, thermal expansion, and thermal conductivities of the two materials. Tests were performed of the different weld geometries required to achieve welds with good quality and mechanical strength.

In EBW, an electron beam is accelerated though a DC potential difference and focused onto the weld joint. When the beam strikes the material, the electrons stop within a short distance of the surface and deposit their kinetic energy into the surrounding material, and melt the material to form the joint. The amount of power

deposited can be controlled by both the accelerating voltage and the beam current, as well as the rate that the part is moved relative to the beam.

The size of the beam spot determines the power density on the material. If this is too high, the melted material can be vapourized and splatter, resulting in a rough surface and a weak joint. The power density can be further controlled by changing the path of the beam on the material. Rather than simply following the path of the weld joint, the beam can be rastered to make a curricular motion over the weld joint, leading to sophisticated heat patterns on the material and can greatly affect the width and depth of the weld. And finally, for welding dissimilar materials, the beam can be focused more on one of the materials to account for their different thermal properties. In this case, the melting temperature of niobium is 2477°C, while Grade 5 titanium melts at near 1600°C.

The welds on the RF ports are particularly challenging due to their proximity to the knife edge on a 2-1/8 inch Conflat flange. The inner diameter of the ports require that the weld joint be located less than 1 mm from the knife edge, as shown in Figure 5.14. During welding, the knife edge was protected by a machined copper shield that shielded it from stray beam, as well as acting as a heat sink in contact with the knife edge. The weld at this joint has low penetration and acts primarily as a vacuum seal, with additional stitch welding performed on the back side of the flange to add mechanical strength.

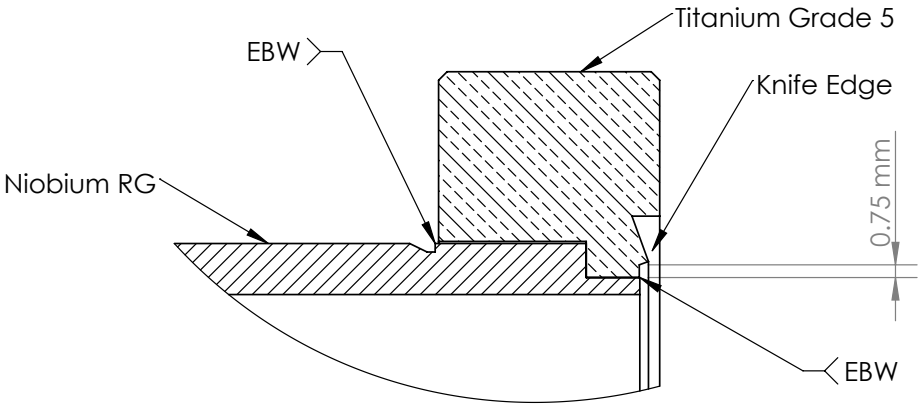


Figure 5.14: Geometry of the RF port weld showing the proximity of the weld to the knife edge. A low penetration weld is performed near the knife edge and stitch welds on the outer surface at the back of the flange.

The RF ports were welded using a 60 kV accelerating voltage and 6.2 mA beam current. The beam was slightly defocussed and a circular rastering on the order of 0.5 mm was used to achieve a smooth weld joint. The beam was aligned such that it was roughly 80% on the niobium so that it would receive the majority of the heat load. The parts were rotated such that the weld joint was moving at a speed of 8 mm/s. The welds were all found to be leak tight and achieved excellent quality. An image of the RF port weld is shown in Figure 5.15.

Figure 5.15: The welded joint between niobium and the titanium RF port flange.

The welds between the beam pipe and flanges were significantly easier welds to perform. Due to the larger flange size, the tube is located far from the sealing surface and extends past the end of the flange, allowing the weld to be performed on the outside of the beam pipe. These were welded with a 60 kV, 13 mA beam with twice the rastering diameter as the RF port welds, but at the same speed, resulting in a thicker weld with more penetration.

## 5.5 Inspection of the Cavity

The completed cavity is shown in Figure 5.16. All welds were successfully completed with no major issues during fabrication. Visual inspections of all of the welds were completed, in addition to leak checking after each weld.

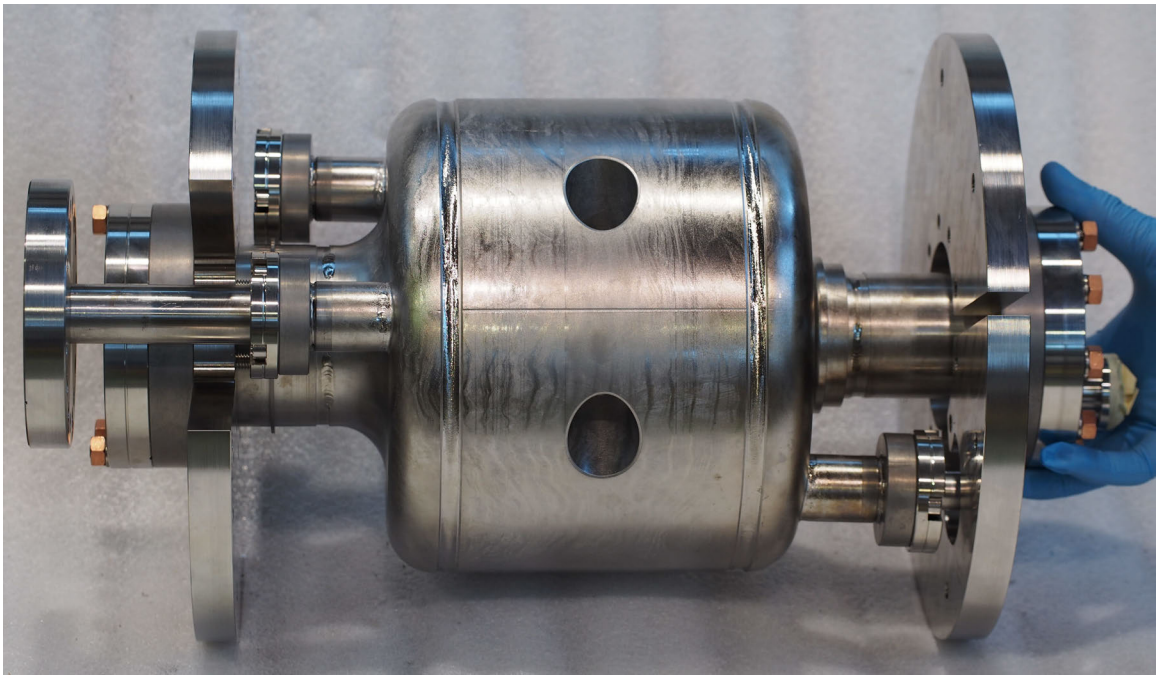

Figure 5.16: The completed niobium cavity. The cold test auxiliary components are partially installed in this picture, including the flange covers and stainless steel reinforcing plates.

The welds on the end cap assemblies were inspected before welding onto the cavity body. These welds, performed from the inner surface, resulted in very smooth weld seams. Images of the end cap weld seams are shown in Figure 5.17. The overlapped sections of the weld, which occur at the location where the welding is stopped over top of the starting location, all show very smooth transitions, resulting in an almost imperceptible boundary.

It was found that the end caps had deformed slightly after welding. This may partially be due to internal stresses being released as the material was heated, or from how the ports were supported during welding. The deformation resulted in a $\sim 0.5\,\text{mm}$ gap between the upstream end cap and body during the subsequent RF stack-up. This deformation was easily removed during the trimming of the end caps to their design lengths.

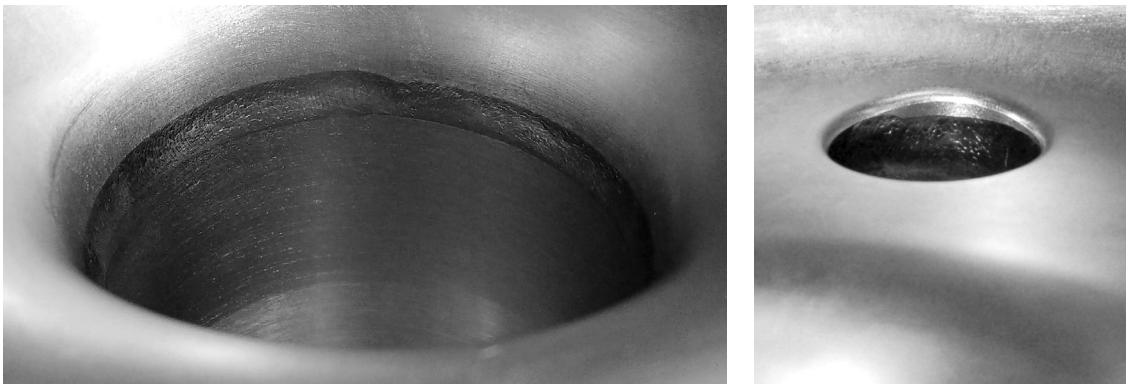

(a) (b)

Figure 5.17: The downstream end cap welds, a) on the beam pipe, and b) on the RF port. Both images show the overlapped section of weld.

Images of the inner seams of the full penetration welds between the end caps and body were acquired using a camera outside of the cavity by viewing through a mirror positioned at 45° inserted inside the cavity. Images of the overlapped section of the upstream and downstream welds are shown in Figure 5.18. The full penetration welds resulted in very satisfactory inner weld seams. The welds are smooth, and protrude less than 0.1 mm above the surface. The rippled appearance to the weld seam is mostly an optical effect as a result of the pulsed power delivered to the TIG torch.

After fabrication was completed, the cavity frequency was measured to be about 0.2 MHz high, as is summarized in Table 5.3. The shrinkage of the final weld was larger than expected and resulted in the overshooting of the goal frequency. To decrease the resonant frequency, the cavity was stretched longitudinally by about 0.5 mm.

Low power RF tests were performed on the cavity to characterize the fundamental and higher order mode frequencies and field profiles. These are described in the following chapter.

## 5.6 Preparation for Cryogenic Testing

After fabrication, the cavity underwent a series of processes in preparation for cryogenic RF testing. A pristine and clean niobium surface is required to minimize RF losses on the cavity surface and to operate at high fields. A diagram summarizing all the steps in this workflow is shown in Figure 5.19, starting from the completion of the cavity fabrication, to the cavity being ready for the cold test.

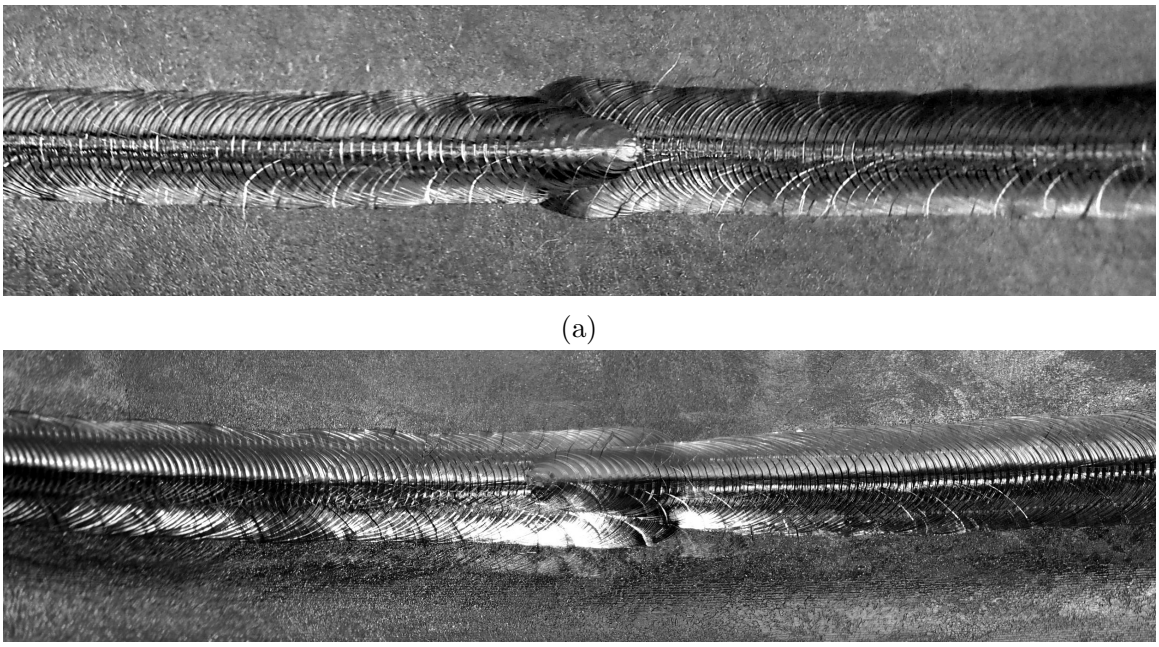

(a)

(b)

Figure 5.18: Images of the full penetration weld seams, on the inner side of the cavity, on the a) downstream and b) upstream ends of the cavities.

### 5.6.1 Surface Preparation

After the low power tests and dry run assembly were completed, the cavity was etched by Buffered Chemical Polish (BCP) to remove a layer from the surface that becomes damaged during fabrication. BCP uses a mixture of acids to remove niobium from the surface, generally Hydroflouric (HF), Nitric ($HNO_3$), and Phosphoric ($H_3PO_4$) acids in a ratio of 1:1:1 or 1:1:2. The HF reacts with the niobium oxide layer on the surface to remove it, while the nitric acid undergoes an oxidation reaction with the freshly revealed pure niobium to regrow the oxide layer. The phosphoric acid is included in the mixture to slow down, or buffer, the rate of the reaction.

The BCP etching process is exothermic and the rate of removal increases with temperature. Additionally, the etching process can allow hydrogen to be absorbed into the niobium once the oxide layer has been removed. To limit the absorption of hydrogen, the acid and cavity are cooled during etching, aiming to keep the temperature below 18°C [81]. The acid is pumped through the cavity to continually refresh with chilled acid and the cavity body was cooled by water cooling lines strapped around the cavity body.

The rate of removal can be affected by the flow of the BCP mixture near a surface

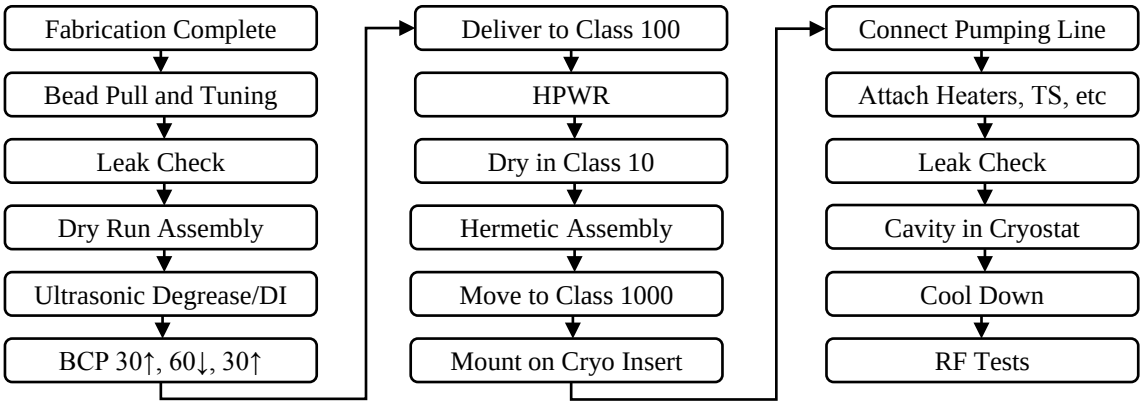


Figure 5.19: The steps performed to prepare the cavity for cryogenic testing.

and the accumulation of niobium precipitate. A high flow rate or turbulence from rising gas bubbles near a surface can lead to more removal and material thinning that can reduce the mechanical strength of the wall or cause a vacuum leak. Too little removal can result in a higher residual resistance if the damaged layer is not fully removed. Non-uniform etching of different areas of the cavity can also result in unexpected shifts to the cavity's resonant frequency.

If the entire removal was done in a single step, the downward facing surfaces would receive more removal than the upward facing surfaces. Cavities of complicated geometry can require many steps to sufficiently etch all surfaces [82]. In other cases, nonuniform etching has been used as a technique to shift the frequency of a cavity in a predicable manner in process referred to as differential etching, first employed at TRIUMF on the QWR cavities [83].

The separator cavity was etched in three steps, flipping the orientation after each one to minimize the differential etching due to orientation. The cavity was etched 30 µm with the upstream end of the cavity up, 60 µm with the cavity reversed, and finally 30 µm with the upstream end upwards again. The cavity set up for etching is shown in Figure 5.20. Acid is continuously pumped into the bottom of the cavity through a Teflon manifold bolted to the beam pipe flange and is allowed to flow out of an overflow valve located in the top manifold to continually refresh the acid within the cavity with chilled acid. Throughout etching, the acid temperature within the cavity remained below 11.5°C. The RF ports are connected to the top and bottom manifolds of the etching fixture to allow the acid to contact the entire RF surface and to avoid trapping gases in any enclosed spaces.

The frequency was measured after each step of etching, showing much larger shifts

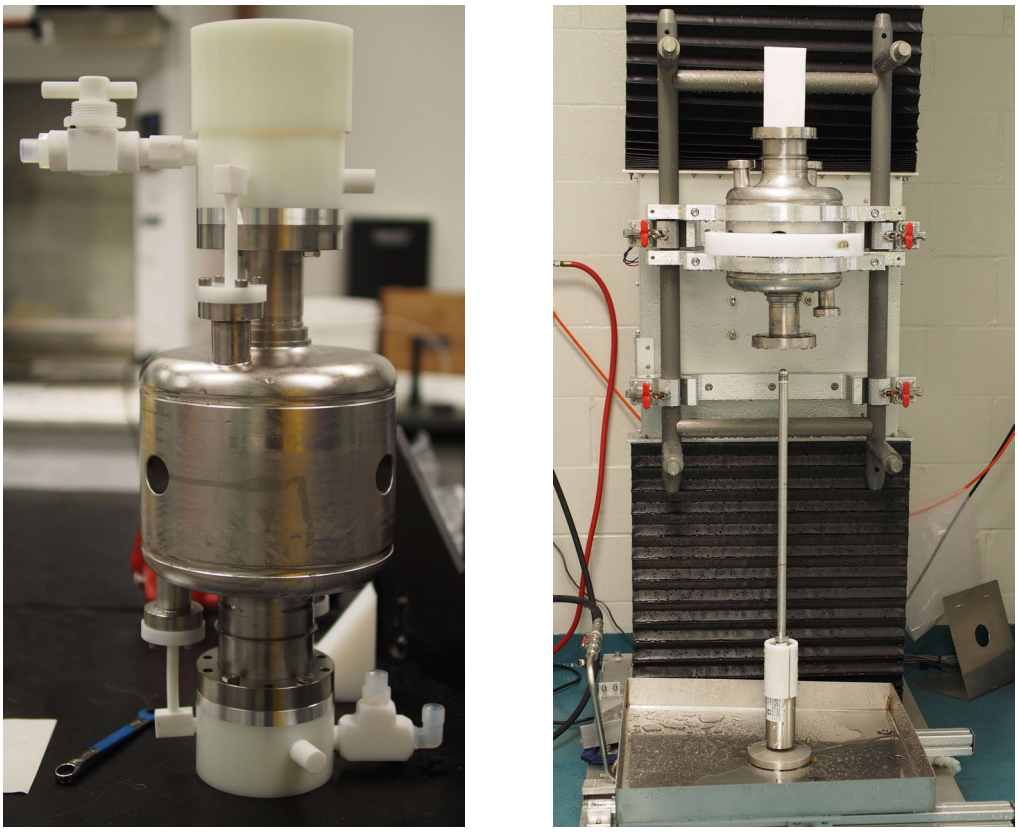

(a) (b)

Figure 5.20: The setups used for a) etching, and b) HPWR of the cavity. The etching fixture is shown without the water cooling loops installed.

in frequency than were simulated assuming uniform surface removal, as summarized in Table 5.5. The large frequency change can be partially explained by differential etching occurring. A positive frequency shift indicates increased etching has occurred on the electric field areas. For this cavity, the high electric field occurs on the ridge faces. Due to their orientation in the cavity, the ridges are exposed to a higher rate of flow of acid and gas bubbles past their surfaces. The increased spacing between the ridges due the etching reduces the electrical capacity and increases the RF frequency. In comparison, the primary magnetic field regions are located behind the ridges, and would likely see less fluid flow, and thus a lower etching rate.

However, since the frequency shifts vary significantly between each step, a firm conclusion cannot be made regarding the etching rates. It should be noted that the initial frequency measurement was performed before the cavity was cleaned in the ultrasonic bath, and the final frequency was measured after the cavity was rinsed by

Table 5.5: Comparison of the measured frequency shifts measured during etching, compared to the expected shifts assuming uniform surface removal.

| Step | Measured Frequency (MHz) | Shift (kHz) | Expected (kHz) |
|---|---|---|---|
| Starting Frequency | 649.07 | | |
| 30 µm, upstream up | 649.134 | 64 | 2.5 |
| 60 µm, downstream up | 649.178 | 44 | 5 |
| 30 µm, upstream up | 649.294 | 116 | 2.5 |

the HPWR and completely assembled in the cleanroom. These processes should not have changed the cavity frequency, however, any deformation of the cavity occurring in these steps would also contribute to the initial and final frequency shifts.

The cavity surface quality is very poor after etching, as is seen in Figure 5.21. The surface is very rough, and under magnification, the pattern of light and dark areas can be seen to be a result of varying grain structure across the surface. The orientation of the crystalline structure affects the etching rate, resulting in the different grains becoming etched by different amounts. The darker areas seen on the cavity surface contain larger grain sizes that have etched relatively flat over a single grain. The specular reflection of light off of these areas causes them to appear dark, unless looking directly at the reflection angle with respect to the source of the light. The areas that appear lighter contain much smaller grains and reflect the light more diffusely, resulting in light being reflected at any viewing angle.

In addition to the local grain pattern, a series of relatively deep lines can be seen on all surfaces inside the cavity after etching, as shown on the end of the ridge in Figure 5.22. On closer inspection, these lines can be seen to be made up of a series of pits forming narrow channels across the surface of the material.

During the production of niobium for cavity fabrication, an ingot is formed through the process of electron beam melting. As an ingot cools, long columnar grains are formed throughout the ingot. To produce fine grain material, the ingot is forged to break up these relatively large grains, resulting in a more uniform material. In discussions with the material vendor, it was suggested that due to the size of the niobium cylinders used to fabricate this cavity, insufficient forging of the ingot could result in the nonuniform grain structure seen on the cavity surface.

Other cavities that have been fabricated from low purity material have also been found to suffer from pits forming on their surface after BCP [75]. The presence of these

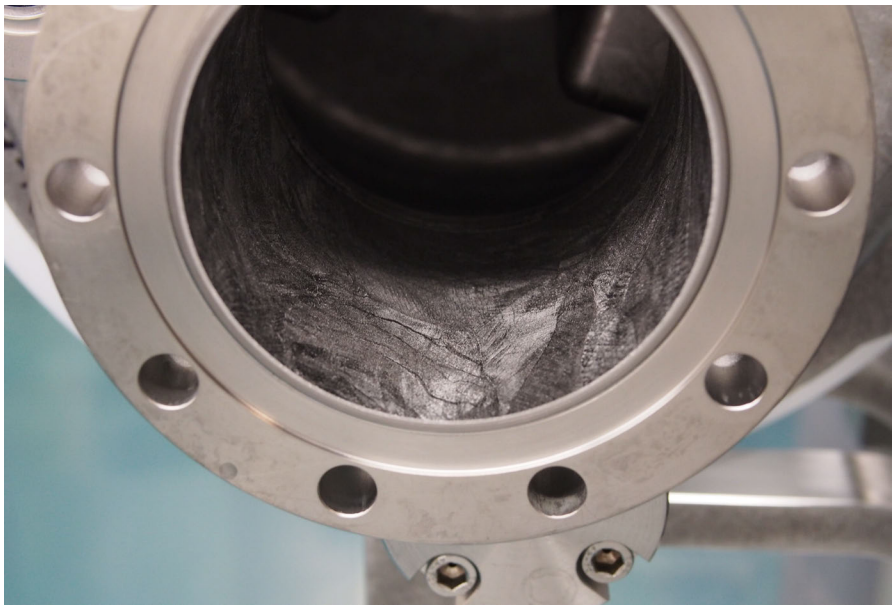

Figure 5.21: The surface appearance of the upstream beam pipe after the 120 µm etch.

Figure 5.22: The surface appearance of the ridge after the 120 µm etch.

pits were observed to induce early quenches, and a higher concentration of oxygen and hydrogen were found in the pitted areas of the cavities. Since impurities can be concentrated at grain boundaries, the pitting seen in the separator cavity material could be a result of the original grain boundaries existing in the ingot material.

In spite of the poor surface roughness, it was decided to proceed with the preparations for RF testing to acquire a baseline measurement of the cavity performance. Simply reprocessing the cavity is not excepted to result in a smoother surface, and in fact would likely only worsen the effect. Possible treatments of the cavity that could help include a recrystallization of the cavity through a high temperature bake, or electropolishing (EP) the cavity surface. Recrystallization could act to redistribute impurities and grain boundaries, which may limit pitting during subsequent BCP. EP preferentially etches higher points on the surface and would result in significantly less pitting and enhancement of grain boundaries. However, as these processes can take significant time to develop, the cavity was prepared for testing to determine if any further processing of the cavity surface is required.

After the final etch, the cavity was transferred to the Class 100 clean room for the high pressure water rinse (HPWR). In this step, the inner cavity surfaces are sprayed with jets of high pressure water from a nozzle inserted into the cavity to remove any remaining particulates. The HPWR system at TRIUMF consists of a rotating wand and linear motion system to lift and lower the cavity (Figure 5.20).

To cover the entire surface of the cavity, the nozzle was inserted through the beam pipe in both orientations as well as through all three RF ports. Passing the wand through the input and HOM coupler ports allows the upper and lower surfaces of the ridges to be rinsed, since these are not reached by rinsing through the beam pipe alone. The coverage achieved by rinsing through the different ports is depicted in the Figure 5.23. Due to the relatively small diameter of the RF ports, a Teflon collar was installed on the port flanges to centre the rinse wand in the port and to ensure it did not touch the cavity surface.

The final rinse of the cavity was performed through the beam pipe, in both orientations. The cavity was rinsed for a total of 6.5 hours, resulting in an average rinsing of 10 seconds per $cm^2$ of surface area, with a water pressure of 700 to 850 psi. After rinsing, the cavity was transferred to the Class 10 clean room to dry in the cleanest air possible, away from any work being performed. The cavity was allowed to dry overnight for about 16 hours before assembly.

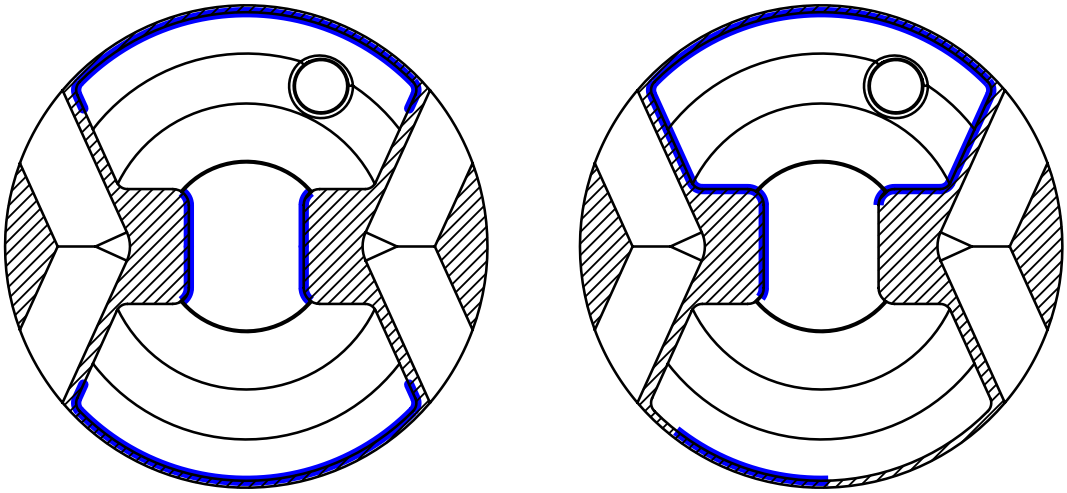

(a) (b)

Figure 5.23: The blue surfaces indicate areas that are rinsed by inserting the rinse wand into a) the beam pipe, and b) the HOM coupler port. The lower surfaces of the ridge are rinsed through the pick up port.

### 5.6.2 Assembly for Cryogenic Tests

Once completely dried after HPWR, assembly of the cavity took place in the Class 10 clean room to minimize the risk of particulates contaminating the RF surface of the cavity. The cavity was hermetically sealed, with a valve on the pumping line sealing the cavity space. Since this valve becomes submerged by liquid helium during testing, it is referred to as the *cold valve*. The completed hermetic assembly is shown in Figure 5.24.

During the bath test, the beam pipes were covered with blank flanges to seal the cavity. These blanks are stainless steel and can result in significant dissipated power on the upstream end of the cavity due to the enlarged beam pipe allowing magnetic fields to propagate to the flange face. The upstream stainless steel flange would contribute a $Q$ of about $3 \times 10^9$, resulting in an error of about 10% to the cavity $Q_0$. The blank flange on the upstream end of the cavity was therefore lined with a niobium plate on the inner side to decrease this power loss to an insignificant level. The niobium plate was fastened to the flange with two small stainless steel screws located in the field minimum locations to limit power dissipation on the screw heads. The inclusion of the niobium plate would increase the $Q$ of the flange to greater than

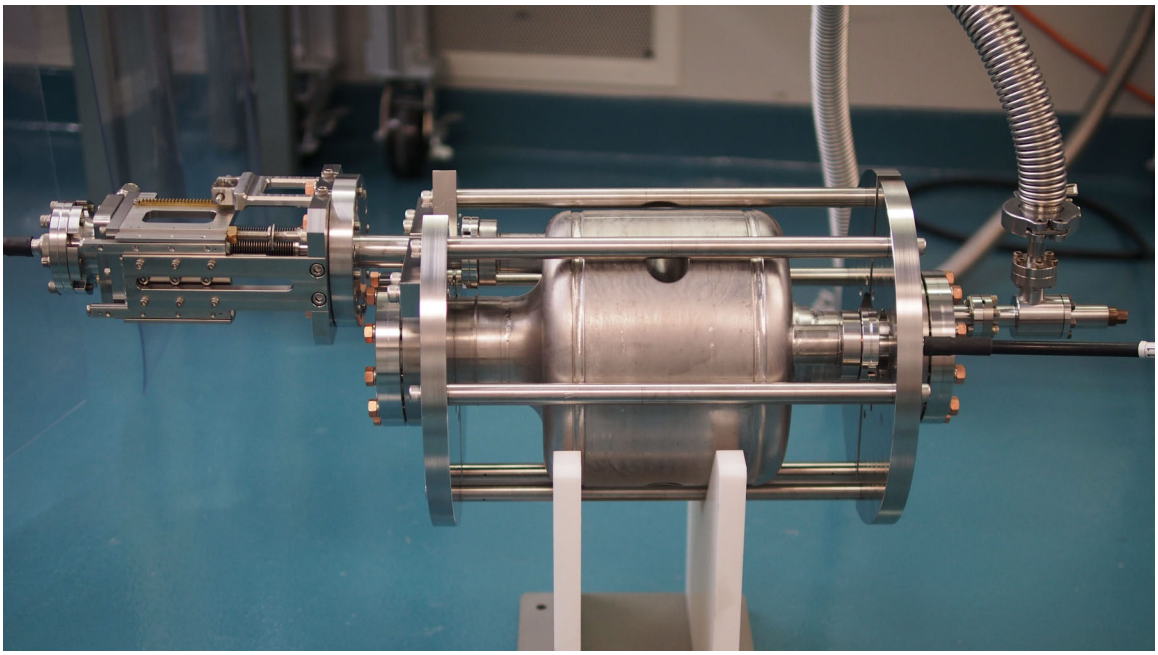

Figure 5.24: The hermetically sealed cavity with the support frame installed. The variable input coupler is on the left and pick up feedthrough on the right. The cavity is being pumped down through the cold valve, also on the right.

$10^{14}$, contributing an insignificant source of error. The downstream flange was left uncovered as the magnetic field on its surface is much lower.

The HOM port was also covered with a blank flange since a HOM coupler was not installed for the bath tests. A variable input coupler was used for the cold tests, allowing the cavity to be measured in the matched condition, where the cavity $Q_0$ is equal to the coupler $Q_{ext}$, over a range of cavity conditions. To use a variable coupler that was on hand, an adaptor was made to match the flange size of the coupler to the input coupler port on the cavity, and to avoid spatial interference of coupler and beam pipe. The full travel of the coupler allowed critical coupling over the range of $Q_{ext} = 10^4$ to $10^{11}$.

After the cavity was hermetically sealed and pumped down to below 30 mTorr, the cold valve was closed and the cavity moved out of the Class 10 area to be assembled onto the cryostat insert. The cavity is shown hanging from the insert in Figure 5.25. The cavity was hung a few cm from the bottom of the cryostat and about 3 m below the top lid. The large diameter cryostat allowed the cavity to be mounted horizontally, eliminating the chance of trapping helium gas in the cooling channels that would reduce the cooling efficiency of the cavity leading to higher surface temperature or

early quench.

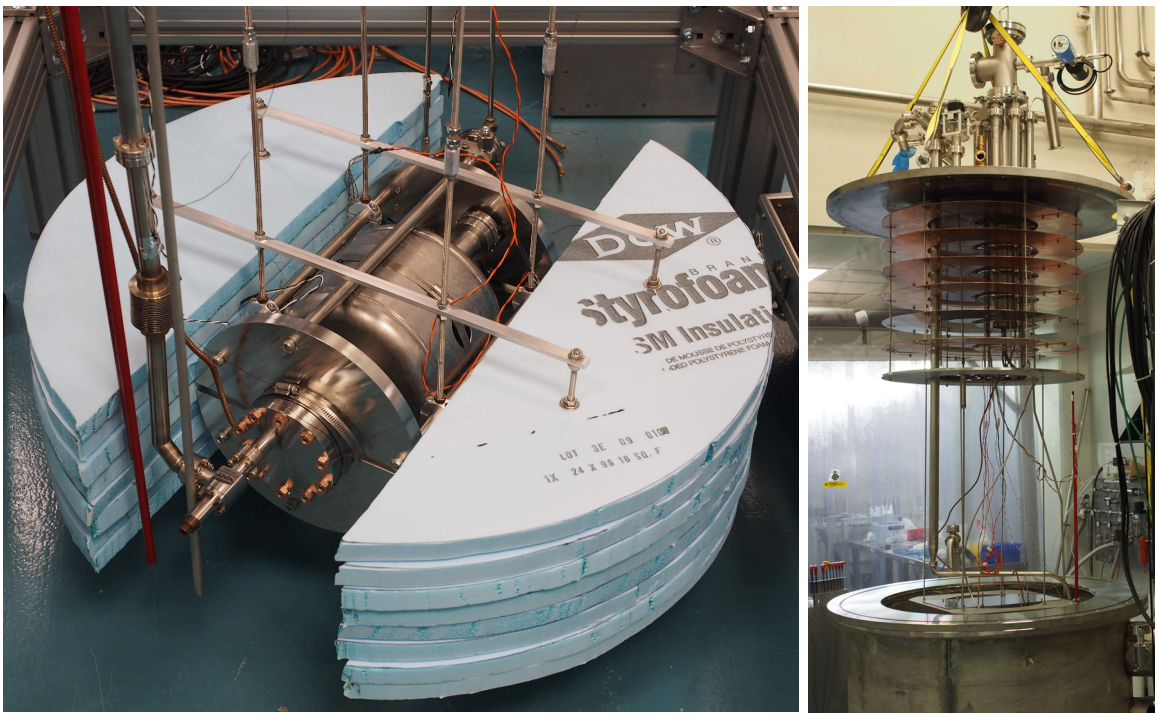


(a) (b)

Figure 5.25: a) The cavity installed on the cryostat insert with styrofoam ballast, and b) the insert being lowered into the cryostat.

After the vacuum pumping line was connected to the cold valve, the pumping line was also pumped below 30 mTorr, roughly the same pressure as the cavity space, before opening the cold valve and closing the *warm valve* on the lid of the cryostat insert. This careful process of ensuring minimal pressure differences on either side of a valve before opening is required to minimize the risk of particulates being carried into the cavity where they can contaminate the RF surface.

Several temperature sensors were installed on the cavity and coupler, as well as a pair of 40 W heaters on the cavity body to aid in boiling off the liquid helium and heating the cavity for the low temperature bake. To reduce the volume of helium required to submerge the cavity, a ballast of closed cell styrofoam was fixed around the cavity to displace a volume of approximately 60 L. The ballast was only included in the first cool down of the cavity, to ensure sufficient liquid helium was available to submerge the cavity with enough depth for several hours of testing, including a pump down to a bath temperature of 2 K. The ballast was removed after the initial test to allow the low temperature bake of the cavity. The bake would heat the cavity to a

temperature greater than 100°C, high enough to melt the styrofoam.

Before filling the cryostat with liquid helium, the helium space is pumped down to $< 200$ mTorr and purged with helium gas three times to rid the system of most of the remaining gases that could contaminate the helium system. The purging is particularly important in this configuration, as the use of ballast in the cryostat increases outgassing and the amount of trapped gas in the cryostat.

The cool down of the cryostat was relatively slow as a result of the large cryostat size. The average rate of cool down in the range from 200 K to 50 K was about 1.4 K/min. Typically, cavities containing large amounts of dissolved hydrogen are recommended to be cooled at a rate higher than 1 K/min to reduce the risk of developing Q disease [84]. The temperatures read by sensors on the cavity and cryostat during the cool down are plotted in Figure 5.26.

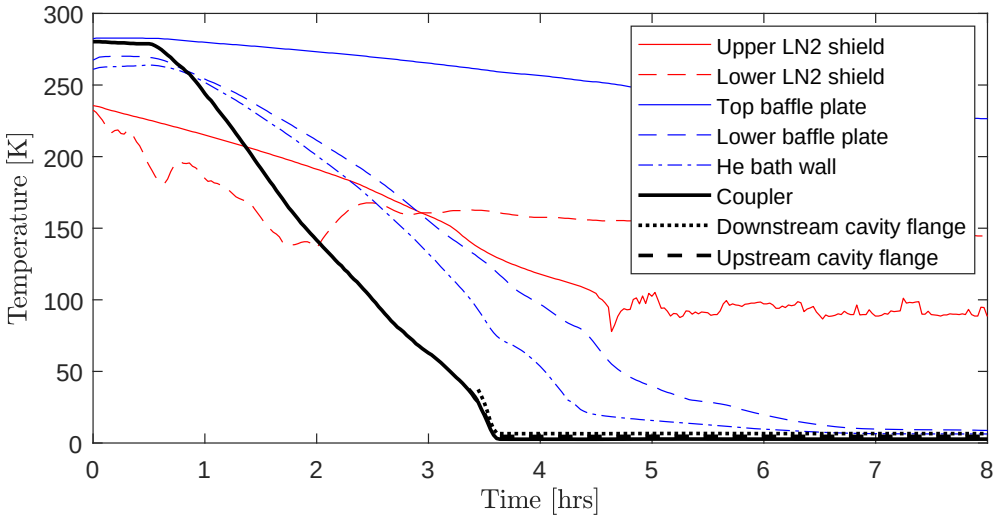


Figure 5.26: The cool down of the cavity and cryostat during the first cavity test. The cryostat started at temperatures up to 50 K below room temperature as the cryostat had been partially cooled by the liquid nitrogen shield the previous day. Liquid helium level started building up just before 4 hours after the cool down started, with RF testing beginning about 30 minutes later.

As soon as the cavity was completely submerged, RF power was fed into the cavity and testing commenced.

# Chapter 6

# RF Tests

Both low power and high power cryogenic RF tests were performed to characterize the performance of the RF separator cavity. At room temperature, bead pull measurements of the fundamental and HOMs were performed to extract the frequency and on axis field profiles.

After the surface preparations were completed and the cavity rinsed by HPWR, it was assembled for installation into the cryostat for high power testing at temperatures down to 2 K. These tests provided the measurements of the quality factor as a function of the deflecting field, the maximum cavity voltage achieved, and the surface resistance along with other properties of the cavity behaviour.

The methods and results of both low power and high power RF tests are described here.

## 6.1 Bead Pull Measurements

The bead pull technique was used to determine the on axis electric field profile of the cavity's resonant modes up to frequencies of 3 GHz. This method uses a small dielectric or metallic bead inserted inside the cavity that perturbs the fields, resulting in a shift of the resonant frequency. The frequency shift, $\Delta f$, can be measured and is related to the change in stored energy in the electric and magnetic fields through Slater's Theorem [85]

$$\frac{\Delta f}{f_0} = \frac{\Delta U_E - \Delta U_M}{2U} \tag{6.1}$$

where $f_0$ and $U$ are the unperturbed resonant frequency and stored energy within the

cavity, and $\Delta U_E$ and $\Delta U_M$ are the change in stored energy due to the presence of the bead.

A dielectric bead generally has relative permittivity, $\epsilon_r > 1$ and relative permeability, $\mu_r \simeq 1$. Therefore, a small dielectric bead placed inside the cavity will change only the electric field energy and therefore yields the electric field magnitude at the location of the bead. The field profile can be extracted by measuring the frequency shift with the bead placed at different locations through the cavity.

The bead pull measurement set-up is sketched in Figure 6.1. The bead is fixed to thin nylon fishing line that passes through the cavity on its axis. One end of the line is held taught by a weight, while the other is tied to a stepper motor that moves the bead through the cavity at a controlled rate. A network analyzer is connected to the RF ports of the cavity to provide the low power RF measurement.

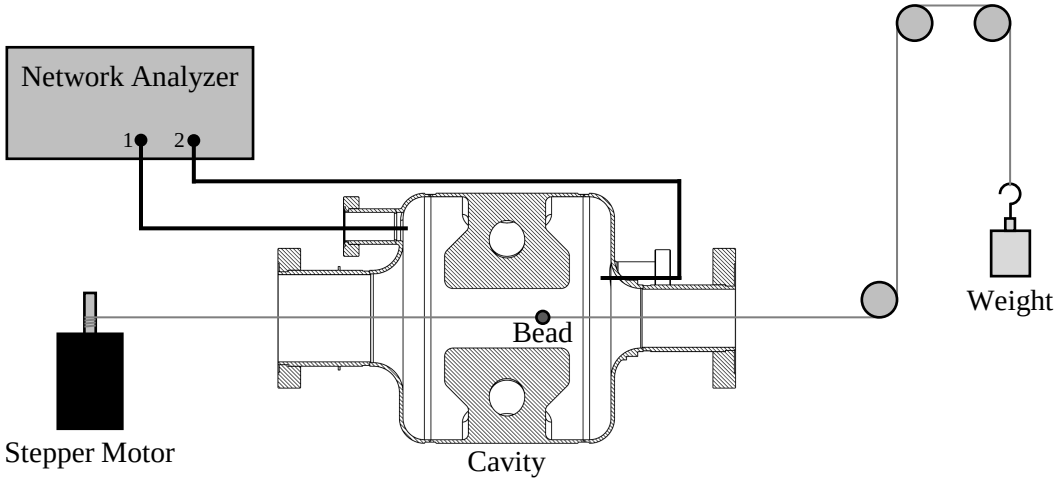


Figure 6.1: Schematic of the bead pull measurement setup. The NWA and stepper motors are connected to the PC that controls the motion of the bead and acquisition of the phase measurement.

The change in resonant frequency is relatively small, on the order of $10^{-3}\,\%$, so a more accurate measurement is usually used to determine the field profile. If the cavity is driven at the unperturbed resonant frequency through one port, a shift in the resonant frequency of the cavity will cause a phase shift, $\phi$ in the signal transmitted to the second port, by an amount

$$\tan(\phi) = 2Q_L \frac{\Delta f}{f_0}. \tag{6.2}$$

By combining Equations (6.1) and (6.2), the relative electric field magnitude at the location of the bead, assuming the bead is small compared to the variation in electric field, is given by

$$E \propto \sqrt{tan(\phi)}. \tag{6.3}$$

Repeatedly taking phase measurements as the bead moves through the cavity provides the relative electric field as a function of distance through the cavity. With a little more information, such as the bead size, permittivity, and loaded $Q$ of the system, the absolute electric field can be determined. And with a second measurement with a bead with $\mu_r \neq 1$, the magnetic field may also be deduced.

The bead pull measurement of the operating mode was performed on the cavity with a 3 mm ceramic bead, and the antennas positioned in the input and pickup RF ports. The measured electric field profile of the niobium cavity is plotted in Figure 6.2, showing good agreement to the simulated electric field magnitude along the beam axis.

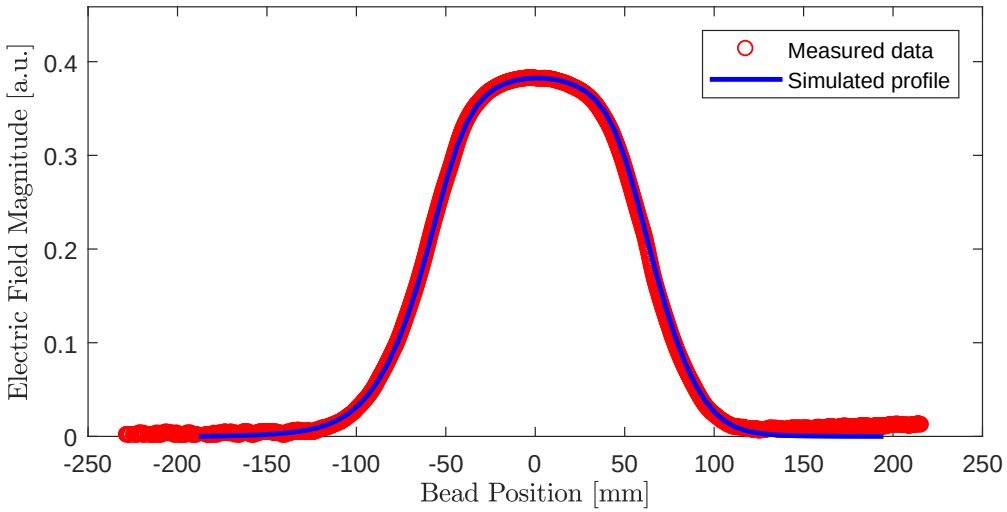


Figure 6.2: Comparison of the measured relative electric field along the beam axis between the bead pull measurement and simulation results.

The HOM field profiles were also measured, for almost every mode up to 3 GHz. The input and pickup antennas had to be moved around to different ports for some modes to be able to couple to the electric field and acquire a strong enough signal to be able to extract a field measurement. Only a few modes were unable to be measured with the available ports, or had a very small on axis electric field magnitude.

Almost all of the measured modes showed good agreement to the simulated field profiles. A few modes had small deviations from the simulated profiles, mostly in the higher frequency modes which have smaller wavelength and are therefore more susceptible to simulation errors or geometrical differences in the fabricated cavity. A summary of the comparison of the measured and simulated field profiles for the HOMs is provided in Appendix A.

Most importantly, the field profiles of the HOMs that had the highest shunt impedances were all found to compare very closely to the simulated fields, and had measured resonant frequencies within less than 1% of the simulated room temperature frequencies. The accuracy of the RF simulations suggests that the HOM damping studies are representative of the fields present in the cavity, and the resultant design should result in sufficient damping of the cavity's HOMs.

## 6.2 Cavity Testing Theory

The basic premise of the test procedure is that RF power is driven into the cavity through the input coupler, at the resonant frequency of the mode being tested. Some of this power is reflected back, while the remainder enters the cavity to build up the fields and either dissipates on the cavity walls or is transmitted through the pick up antenna. After calibration, by measuring three powers – the power sent to the cavity, $P_f$, the reflected power, $P_r$, and the transmitted power, $P_{pu}$, the field amplitude and power dissipated on the cavity walls may be determined.

A schematic of this measurement setup is shown in Figure 6.3. An RF power amplifier supplies power to the cavity after first passing through a circulator that protects the amplifier from reflected power. A directional coupler on this coaxial line measures the forward and reverse powers. The pick up signal from the cavity is split, with part being measured by a power meter, and the remainder passing into the Low Level RF (LLRF) control system, which in turn completes the feedback loop and drives the RF power amplifier.

The LLRF system is required to control the amplitude and phase within the cavity by providing the drive signal to the RF amplifier. The LLRF system used in the cold tests was based on the ISAC II LLRF systems, operating at an intermediate frequency of 140 MHz. The 650 MHz signal from the cavity was downconverted to 140 MHz to take advantage of this existing infrastructure. This system operates in either self excited loop – a feedback loop that drives the cavity at its resonant frequency [86], or

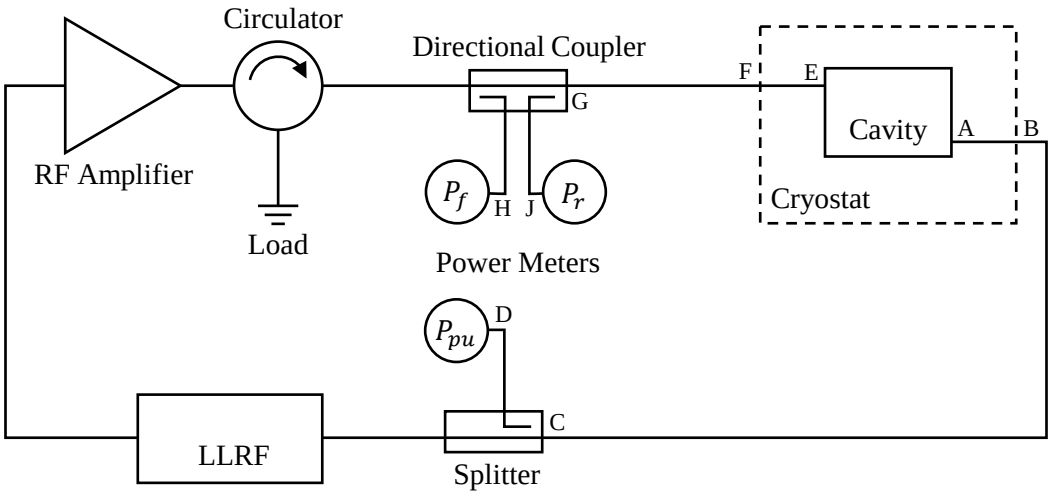


Figure 6.3: A simplified schematic of the cold test measurement setup.

generator driven mode, which drives the cavity at a fixed frequency from an external source.

A number of calibrations are required to properly interpret the measurements. Power loss in the cables requires that cable calibrations be completed to determine the power that would be measured at the cavity, rather than at the power meters that can be located up to meters away. During testing, the pickup probe is calibrated so that the cavity's field amplitude and $Q_0$ may be determined from the three power measurements alone.

### 6.2.1 Cable Calibrations

The power loss in the cables between the cavity and the power meters, from sources including directional couplers, cable connections, and line losses, are critical to accurately determine the power that is truly important – the power at the cavity. Cables can contribute several dB of attenuation, while the directional couplers used in these tests redirect only a small fraction of the signal for measurement adding roughly 40 dB attenuation. The calibration measurements were made at the expected resonant frequency of the cavity, or averaged over a range of 1 MHz in cases where the resonant frequency was not accessible. Since the ends of the input and pick up cables are inside the cryostat, limiting their access, the attenuation in each cable was measured in segments as labelled in Figure 6.3.

The losses in the cold sections of the cables, sections A-B and E-F inside the cryostat, were measured using a network analyzer. Since the opposite end of the cable is inaccessible, the $S_{11}$ scattering parameter is used to determine the losses in these cables. When the signal is reflected, $S_{11}$ represents twice the cable loss of the cable connected to port 1 of the NWA. This measurement relies on the full reflection of the signal from the cavity, so the measurement cannot be made at the cavity's resonant frequency. Rather, the $S_{11}$ was measured on either side of the narrow resonance bandwidth and averaged. This provides a reasonably accurate measurement of the loss at the operating frequency since the cavity bandwidth is very narrow when cold, on the order of Hz or kHz, depending on the coupling. The warm cables, sections B-C and F-G were also measured using the NWA, this time using the $S_{21}$ parameter with the ends of the cables connected to ports 1 and 2.

The power meters were calibrated with a signal generator driving at the cavity's resonant frequency. Each power meter was initially driven directly by the source at a fixed power level, then again through the cables and directional couplers to determine their losses. The attenuation is then the difference between these two measurements.

The attenuations of each segment added together give the total attenuation of each power measurement. These are summarized as follows

$$Att_f = S_{11_{E-F}}/2 + S_{21_{F-G}} + \left(P_{P_f} - P_{G-H}\right) \tag{6.4}$$

$$Att_r = S_{11_{E-F}}/2 + S_{21_{F-G}} + \left(P_{P_r} - P_{G-J}\right) \tag{6.5}$$

$$Att_{pu} = S_{11_{A-B}}/2 + S_{21_{B-C}} + \left(P_{P_{pu}} - P_{C-D}\right), \tag{6.6}$$

where $S_{11_{E-F}}$ is the $S_{11}$ parameter measured on the network analyzer with connected to the cable at positions $E$ and $F$, $P_f$ is the power measured with a signal generator connected directly to the forward power meter, and $P_{G-H}$ is the power measured with the same signal generator connected to the forward power meter through the line $G$ to $H$, and so on.

### 6.2.2 Pick Up Calibration

The initial data point measured can be used to determine the external quality factor of the pick up antenna. Once this is known, subsequent measurements can be made much more quickly, by only relying on the three power measurements that can be

obtained in CW.

When the cavity is being driven in steady state, the measured forward, reverse, and pick up powers, corrected by the attenuations measured above, provide the power loss on the cavity walls, $P_c$, through the energy balance

$$P_c = P_f - P_r - P_{pu}. \tag{6.7}$$

The cavity has a characteristic loaded quality factor, $Q_L$, that takes into account the power loss on the cavity walls and through the input and pick up ports, as described in Section 3.3. When the input power supplied to the cavity is turned off, power is drained from the cavity system and the field amplitude within the cavity decays exponentially with a characteristic decay time

$$\tau = \frac{Q_L}{\pi f}. \tag{6.8}$$

Determining the decay time provides the means for making the initial measurement. After measuring the steady state power levels, the input power to the cavity is cut off and the pickup signal is captured on an oscilloscope as the cavity field decreases. $\tau$ is extracted by analyzing the time series and fitting an exponential curve to the initial few ms of the decay envelope, as shown in Figure 6.4. Only the initial part of the decay is used since the $Q_0$ of the cavity can change at different field levels, resulting in a time varying decay time constant as the field decreases. From $\tau$ and the measured frequency, $Q_L$ can be determined from Equation (6.8).

To calculate the cavity $Q_0$, the various coupling factors need to be accounted for. The pick up is weakly coupled to the cavity, and the coupling factor can be simply determined from the measured pick up power and the determined cavity power,

$$\beta_{pu} = \frac{P_{pu}}{P_c} = \frac{Q_0}{Q_{pu}}. \tag{6.9}$$

With a variable input coupler being used, the input coupler may be moved such that it is critically coupled to the cavity, so the power lost to the cavity walls is equal to the power supplied through the input coupler. In the test setup however, the coupler is actually matched to the cavity plus pick up port since the power leaks out of the system through both. $Q_L$ can then be defined in this system as

$$\frac{1}{Q_L} = \frac{1}{Q_{0+pu}} + \frac{1}{Q_{ext}}, \tag{6.10}$$

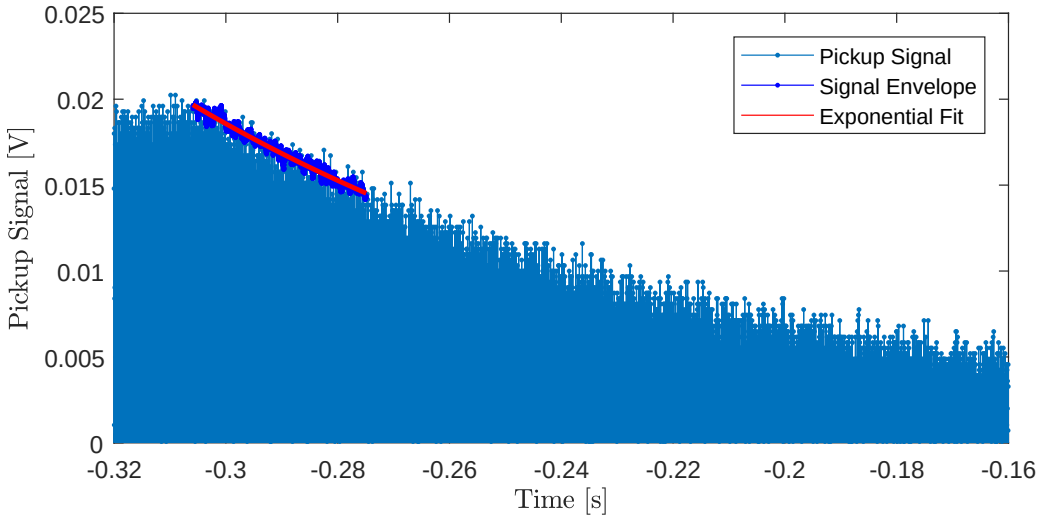


Figure 6.4: An example of a calibration measurement. A decay constant of 0.0985 s was extracted here, corresponding to $Q_L = 2.0 \times 10^8$.

where $Q_{0+pu}$ is the combined $Q$ of both the cavity and pick up. After some rearranging, this can be solved for $Q_0$ using the definition of $\beta_{pu}$, and defining $\beta^* = P_f/(P_c + P_{pu})$, as

$$Q_0 = (1 + \beta_{pu})\,(1 + \beta^*)\,Q_L, \tag{6.11}$$

where $\beta^*$ is assumed to be unity for a matched input coupler. After $Q_0$ is determined, it can be used to calculate the pick up $Q$ from Equation (6.9).

The cavity voltage is determined from the pick up power measurement and the simulated value of the geometric shunt impedance, $R_\perp/Q$. From the definition of the geometric shunt impedance, Equation (3.14), $V_\perp$ is given by

$$V_\perp = \sqrt{Q_{pu} P_{pu} \frac{R_\perp}{Q}}. \tag{6.12}$$

### 6.2.3 Subsequent Measurements

After the initial calibration measurement is completed, further measurements need only the three powers to be measured to yield both $Q_0$ and $V_\perp$. Since the pick up $Q$ is known and will not change between measurements, Equation (6.12) can be used to determine $V_\perp$ from the pickup power alone.

The cavity $Q$ is determined by rearranging Equation (6.9) for $Q_0$, to get

$$Q_0 = Q_{pu}\frac{P_{pu}}{P_f - P_r - P_{pu}}. \tag{6.13}$$

The requisite $Q_0$ versus $V_\perp$ curve may then be realized by repeatedly aquiring the set of power measurements at increasing drive power, ensuring the input coupler is matched at each point.

The main source of error in these calculations is the assumption that the input coupler is perfectly matched during the calibration measurement. The Standing Wave Ratio (SWR) can give an estimate of this error. The $SWR$ can be calculated from the forward and reverse powers as

$$SWR = \frac{\sqrt{P_f} + \sqrt{P_r}}{\sqrt{P_f} - \sqrt{P_r}}. \tag{6.14}$$

If the input coupler was overcoupled, $\beta^* = SWR$, while if undercoupled, $\beta^* = 1/SWR$. The SWR for the reported measurements was on the order of 1.10 to 1.15. Therefore the uncertainty in $\beta^*$, taken as $SWR - 1$, is on the order of 10 - 15%.

Other significant sources of error include the uncertainty in the power measurements and the measurement error in the decay time. Taking all these factors into account results in typically 5% uncertainty on $V_\perp$ and 10–15% on $Q_0$.

## 6.3 Overview of Cold Test Results

The cavity underwent a series of three cold test measurements, to test the response of the cavity to various cavity treatments. The initial test was performed on the cavity prepared as described above. The $Q_0$ of the cavity was measured up to the maximum achievable deflecting field and at temperatures down to 2 K.

The cavity was first tested at 4 K. After an initial calibration measurement, subsequent measurements were taken as the drive power sent to the cavity was steadily increased. Several multipacting barriers were encountered, occurring over the voltage ranges of roughly 0.1 to 0.3 MV, 0.4 MV, and 0.7 to 0.8 MV. These were generally processed within a few minutes, or in some cases up to 10's of minutes, by increasing the coupling strength and driving several Watts of power into the cavity. After processing through these barriers once, multipacting was not observed again at the same voltage.

The low field $Q_0$ was measured to be just over $4\times10^8$, with a value of $3.8\times10^8$ at the

operating voltage of 0.3 MV. This surpasses the goal $Q_0$ of $1.4 \times 10^8$, corresponding to 1 W of dissipated power. The $Q_0$ showed a moderate $Q$-slope, with the quality factor decreasing by about half, to $2 \times 10^8$ at the maximum voltage achieved.

The cavity experienced a hard quench at a voltage of 0.82 MV, corresponding to a peak magnetic field of 33 mT and peak electric field of 26 MV/m. Pulse conditioning was performed to attempt to push the maximum deflecting voltage to higher field without achieving any significant gain in voltage. The performance curve for this first test at both 4 K and 2 K is shown in Figure 6.5.

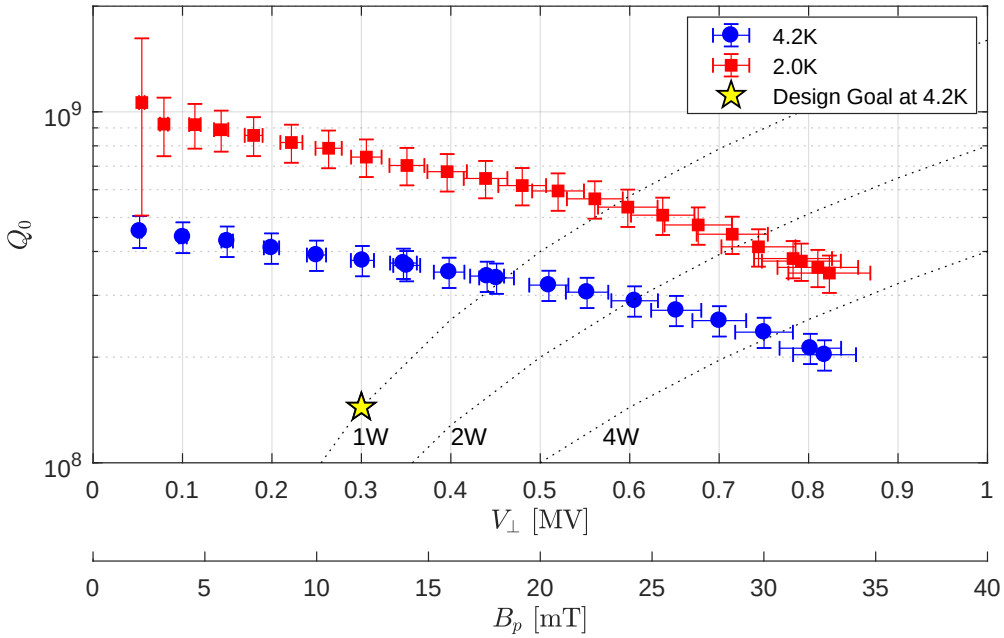


Figure 6.5: The performance of the deflecting mode cavity in the initial cold test. The cavity surpassed the design goal, operating with less than 1 W power dissipation at a voltage of 0.3 MV.

After 4 K testing was completed, the cavity was cooled to 2 K for further testing. At atmospheric pressure, liquid helium has an equilibrium temperature of 4.2 K. Cooling the cavity to 2 K requires pumping the helium space down to a pressure of 30 mbar. The quality factor was measured at 6 voltages between 0.3 to 0.7 MV during the cool down process, allowing for the extraction of the BCS and residual components of the surface resistance. This will be discussed in Section 6.3.3.

At 2 K, the cavity reached a low field quality factor of about $9 \times 10^8$, dropping to $3.2 \times 10^8$ at the maximum voltage. Multipacting did not occur again in the voltages measured at 4 K, but did occur at the highest fields, above what was reached in pre-

vious measurements. The cavity reached slightly higher deflecting voltage, quenching at a voltage of about 0.83 MV.

### 6.3.1 Thermal Effects

Due to this cavity's fabrication method, it behaves differently than the thin walled cavities that are typically built. In all cavities, the surface temperature is slightly higher than that of the bath temperature due to the thermal resistance of the cavity wall and the *Kapitza resistance* at the thermal boundary between the outer cavity wall and the liquid helium. Typically the temperature difference between the RF surface and helium bath is small, but as discussed earlier, the solid ridges on this cavity mean that some surfaces are 10's of mm from the outside surface of the cavity. Additionally, the use of reactor grade niobium means that the effective thermal resistance in the thickest parts of the cavity is up to 100 times greater than for a thin walled RRR cavity.

The result of this is a higher surface temperature and lower thermal stability, leading to decreased $Q_0$ and early quench of the cavity. As the cavity surface warms up, the surface resistance increases and the quality factor decreases, meaning that the steady state $Q$ curve will be lower at the higher fields than if measured immediately after turning the RF on.

The cavity showed signs of increased surface temperature at points tested above 0.7 MV, which is close to what was expected from the thermal feedback model developed in Section 4.9.3. Taking a rapid series of measurements as the cavity voltage was suddenly increased from very low field to a higher field value showed the quality factor decreasing over about a minute, by up to about 1.5% before settling down to a stable steady state value. This is on the order expected from thermal feedback simulations at 2 K. However, since this is a relatively fast process, there is a large uncertainty in the initial, *unheated* $Q_0$ as by the time of the first measurement the surface was likely to have heated up for several seconds. This trend can be seen in Figure 6.6, which shows the range of $Q_0$ measured after suddenly stepping up the voltage, at several field levels.

The reverse was also observed, when the cavity field was suddenly decreased from the maximum voltage, down to 0.2 MV where no significant surface heating was expected. In this case the quality factor was found to increase by about 4% as the surface temperature decreased before stabilizing.

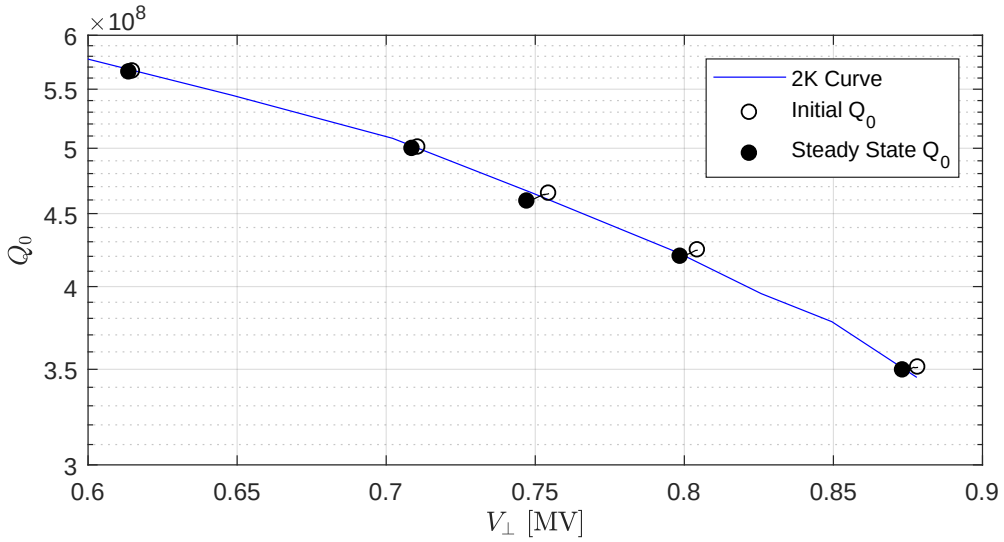


Figure 6.6: The effect of the thermal response on the measured $Q_0$ curve at 2 K, as the surface temperature reaches steady state over approximately 1 minute.

The observed slope in $Q_0$ may also be related to other thermal effects, unrelated to those discussed above. One possible explanation [87] for high field $Q$-slope in cavities is that the protruding edges of roughness features can see increased fields due to local field enhancement. The higher fields on the protruding edges can increase the heating on these small features, leading to increased resistance and even tiny normal conducting areas spread over the surface of the cavity. These may not dissipate enough power to cause a thermal breakdown and quench the cavity, but will still lead to increased power dissipation and decreased $Q_0$. Although the onset of the $Q$-slope is not at particularly high fields, the fact that this cavity has a very rough surface after BCP, and due to the low thermal conductivity material, this effect could contribute to the observed $Q$-slope.

### 6.3.2 Mechanical Stability

The pressure sensitivity of the cavity was determined by measuring the resonant frequency at a constant cavity voltage during the pump down of the cavity from atmospheric pressure during the 2 K cool down. This is shown in Figure 6.7. The measured sensitivity was 9.7 Hz/mbar, compared to 13 Hz/mbar modelled with the reinforcing frame supporting the cavity. This is within the goal of less than 10 Hz/mbar, although in the cryomodule, the cavity will be supported by the tuner rather than the support frame.

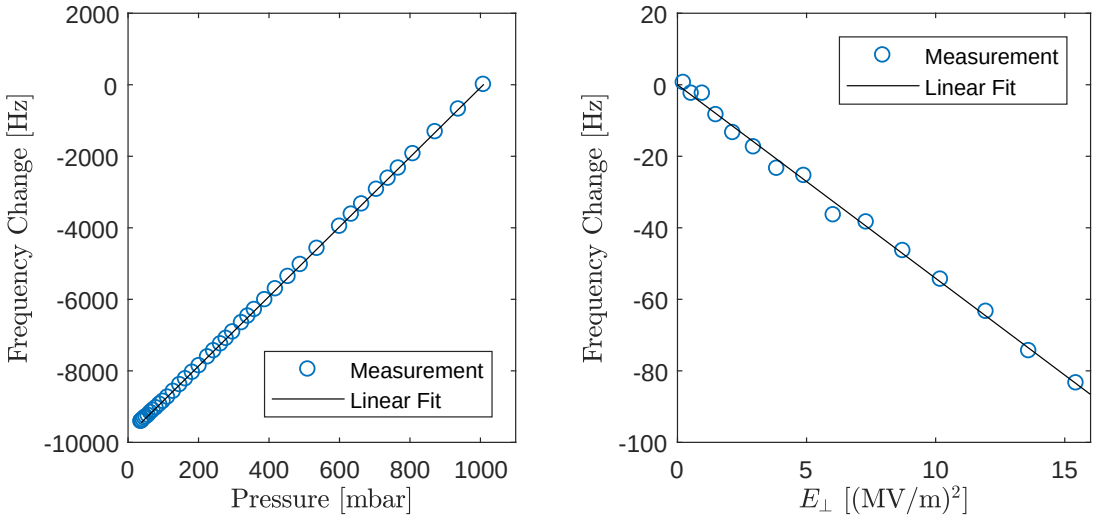


Figure 6.7: The sensitivity of the resonant frequency to a) pressure and b) the deflecting field gradient, $E_\perp$.

The Lorentz detuning coefficient was determined by measuring the frequency shift of the cavity as the voltage was increased. This measurement was performed at 2 K since the pressure stability is much better than at 4 K. The results of this measurement are also shown in Figure 6.7, and resulted in a measured Lorentz detuning coefficient of $-5.4\,\mathrm{Hz/(MV/m)^2}$.

### 6.3.3 Surface Resistance Analysis

The $Q_0$ measured in cavity tests can be converted to the total surface resistance averaged over the cavity surface through the geometry factor that was determined from simulations by the relation $R_s = G/Q_0$. Using BCS theory, this total surface resistance can be broken into a temperature dependant BCS component, and constant residual component, as discussed in Section 3.4.2. The total surface resistance as a function of the temperature is approximated by the equation

$$R_s(T) = R_{res} + \frac{A}{T} e^{-\Delta/(k_B T)}, \tag{6.15}$$

where $R_{res}$ is the residual resistance, $k_B$ the Boltzmann constant, and $A$ and $\Delta$ are two material dependant properties that may be used to fit to the data. A typical value for $\Delta$, the energy gap of niobium, presented as $\Delta/(k_B T_c)$, is 1.86 [34].

Figure 6.8 shows the fit results of Equation (6.15) to the surface resistance measured at 0.3 MV during the cool down from 4.5 K to 2 K. At this field, the residual resistance was found to be $131 \pm 12\,\mathrm{n\Omega}$, a number that is at least an order of magnitude greater than for a typical cavity with a good quality and well prepared surface. As discussed earlier, the high residual resistance could be a result of the roughness of the surface, or could be in part due to the presence of a high ambient magnetic field within the cryostat, on the order of 30 µT. However, since the cavity is fabricated from material with relatively low $RRR$, it should be less susceptible to the ambient magnetic field than a typical high purity cavity. This cavity was the first to be tested in the new cryostat and the insufficient shielding of the magnetic field was only discovered after testing of the cavity had been completed.

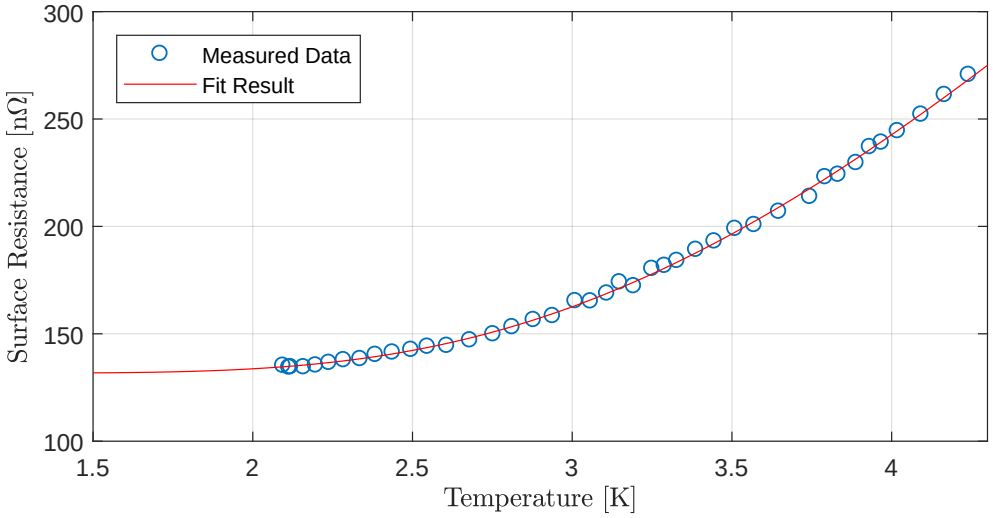


Figure 6.8: The total surface resistance measured as a function of temperature, fit using BCS theory for data measured at 0.3 MV.

Data was collected at voltages up to 0.7 MV, showing a strong field dependence to the surface resistance. In Figure 6.9, the residual resistance can be seen to increase to $220 \pm 20\,\mathrm{n\Omega}$ at a deflecting field of about 0.7 MV. The strong field dependence could indicate a contribution from the surface roughness to the surface resistance through the same mechanism that is thought to give rise to high field Q-slope [87], or from thermal heating due to the solid ridge structure. The BCS resistance at a bath temperature of 4.2 K also increases with the field, although with a relatively large fit error. The results after the low temperature bake will be discussed in the following section.

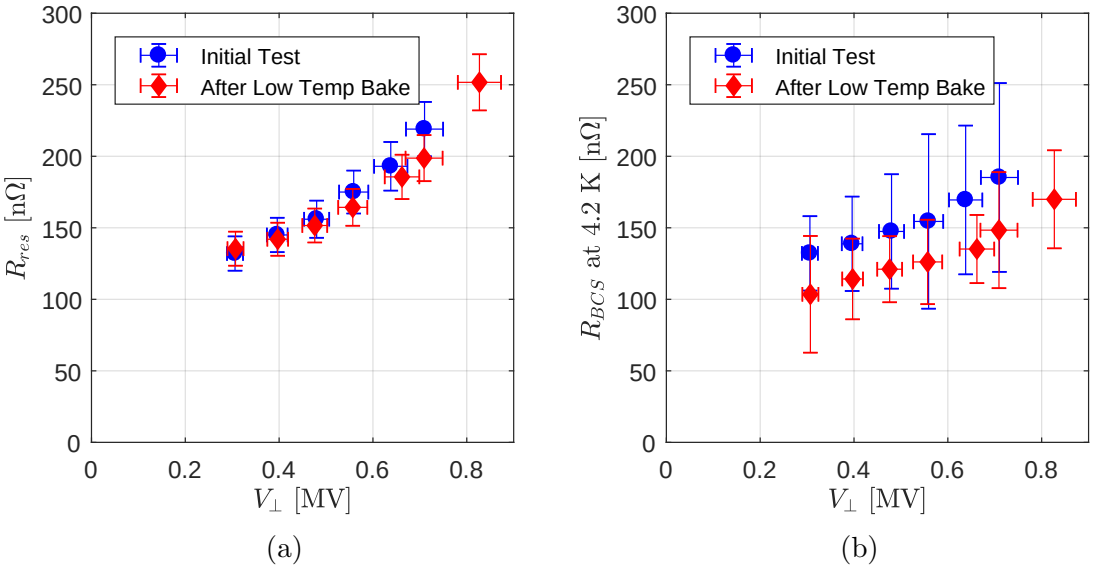


Figure 6.9: The field dependence of the a) residual resistance and b) BCS resistance at 4.2 K, extracted from the surface resistance data.

Figure 6.10 shows the fitted energy gap with a much weaker dependence on the field within the cavity. The energy gap extracted through this fit is about 10% higher than expected, however this falls within the limitations of fitting to Equation (6.15). By applying this fit to the thermal feedback model, a similar energy gap value and field dependence was determined.

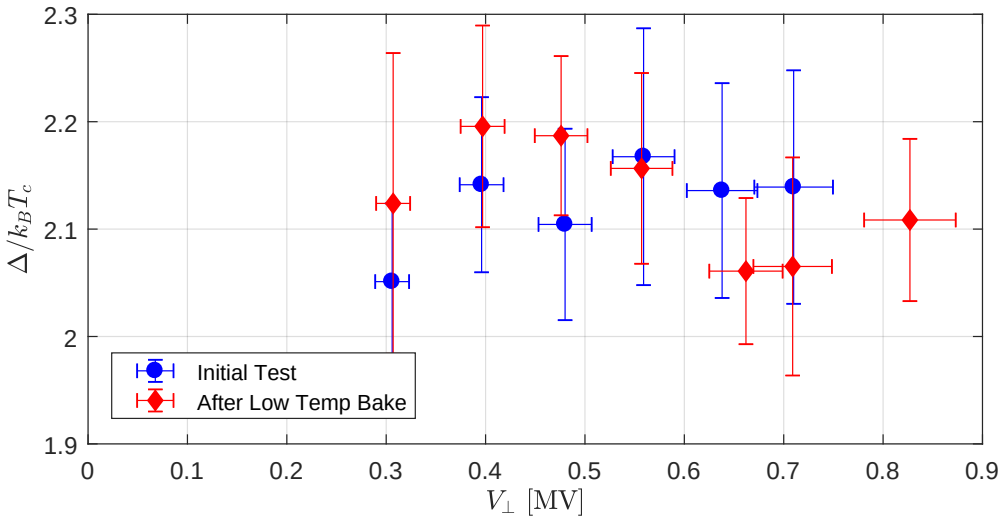


Figure 6.10: The field dependence of the energy gap extracted from the surface resistance data.

### 6.3.4 Results After a Low Temperature Bake

After the initial cold test was complete, the cavity was warmed up to room temperature, the ballast removed, and the cavity reinserted into the cryostat without spoiling the cavity vacuum. The cavity was then baked at $> 100°C$ for a period of 51 hours. The cavity was then cooled down again, and tested at 4 K and 2 K. The results of these tests are shown in Figure 6.11, overlaid on top of the previous test results.

The low temperature bake can seen to have only a small effect on the performance at both 4 K and 2 K. The small variation in the curves could be due to systematic effects and not a significant change in the cavity's performance.

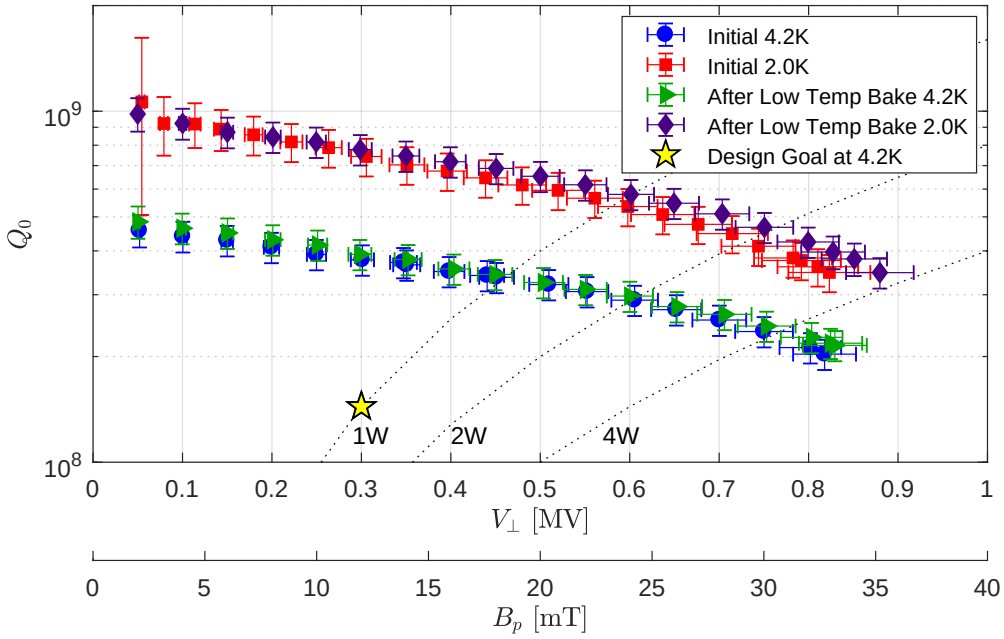


Figure 6.11: The performance of the deflecting mode cavity after the low temperature bake.

The fit results of the residual and BCS resistances and the energy gap from the cool down to 2 K are plotted in Figures 6.9 and 6.10. The residual resistance did not change significantly after the low temperature bake, while the BCS resistance decreased by about 20%, although the change is still within the fitting error. The energy gap was also not affected by the bake.

The relative insensitivity of the cavity to the low temperature bake can be explained by the theory proposed in [88] to describe the mechanism responsible for the improvement in performance after a low temperature bake. This theory describes

that the reduced surface resistance after baking can be attributed to the diffusion of oxygen from the surface niobium oxide layer into the bulk of the niobium, which decreases the mean free path within a thin surface layer. The reduced mean free path can reduce the BCS resistance of the niobium at the surface to more optimized values, resulting in an increased $Q_0$ accordingly. In [89], a cavity with initial RRR of 255 had the RRR at the surface reduced to 209 after a 105°C bake. Additionally, this dissolved oxygen can trap hydrogen and prevent its formation into niobium hydrides. However, since the separator cavity is fabricated from low $RRR$ material, it is not expected to see any improvement by this process.

### 6.3.5 Test for Q Disease

An initial theory to explain the high surface resistance and Q slope seen in the cavity tests was that the cavity may have been suffering from the effects of Q disease due to the relatively slow cool down speed. To test this, the cavity was warmed up to a temperature of 100 K, and held there for a period of 3 hours before cooling down to 4 K again. Upon retesting, no significant change in the 4 K $Q$ curve was observed, as shown in Figure 6.12.

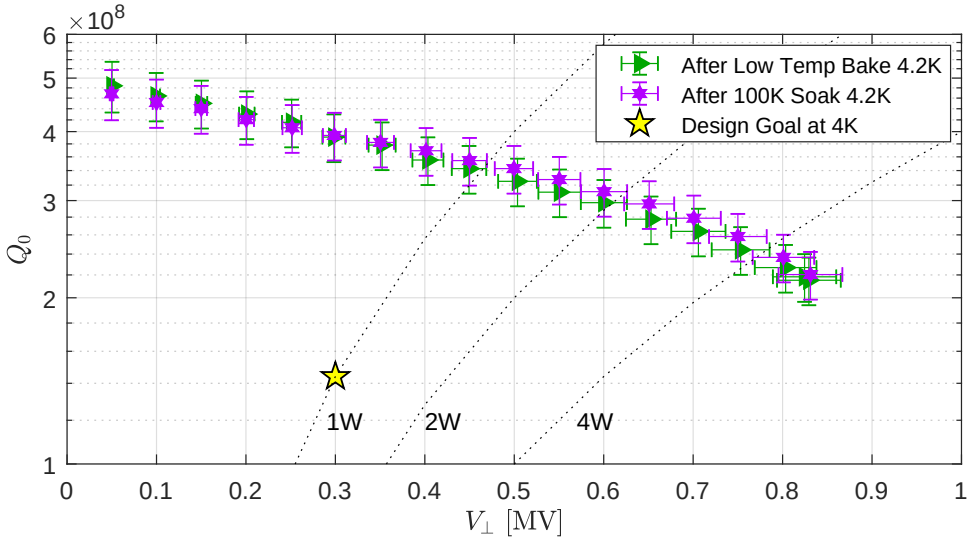


Figure 6.12: The performance of the deflecting mode cavity after being held at 100 K for 3 hours.

Similar to the low temperature baking result, this is the standard behaviour for reactor grade cavities. Q disease is caused by the formation of lossy niobium hydrides.

Their formation can be impeded by oxygen dissolved into the niobium that traps the hydrogen, reducing its mobility and capacity to form hydrides [90]. Reactor grade cavities typically have high oxygen content, in this cavity reportedly 140 ppm, and are generally found to not be susceptible to Q disease. It is stated in [34] that cavities with $> 100$ ppm oxygen content will not be susceptible to Q disease.

## 6.4 Summary and Further Measurements

The SRF deflecting cavity meets the goal of reaching the operating gradient, 0.3 MV, with less than 1 W of dissipated power. The achieved maximum deflecting voltage is 0.82 MV at the operating temperature of 4.2 K, with a peak magnetic field of 33 mT and peak electric field of 26 MV/m. Low temperature baking of the cavity is not required as it was found to have no significant impact in the cavity performance, and the cavity is not susceptible to Q disease.

The residual surface resistance is quite high, likely due to the poor surface quality achieved with this material after BCP, although retesting the cavity with better magnetic shielding would confirm whether the ambient magnetic field is also a contributing factor. Since the surface roughness seems to be related to the grain structure, a further study would be to perform a high temperature bake of the cavity to recrystallize the niobium, followed by a deep etch of the cavity surface to attempt to reset the roughness. A small sample of the material the cavity was fabricated from was used to test this procedure.

Figure 6.13 shows the grain structure after etching for samples with and without receiving the high temperature heat treatment. The recrystallized sample has larger grain size and a much smoother surface than the untreated sample, suggesting that the cavity surface could be improved through a high temperature heat treatment.

Due to the poor surface resistance of the cavity, a conclusive statement regarding the performance of the TIG welds under RF tests unfortunately cannot be made. From a qualitative view, the welds meet the physical requirements with a smooth weld seam, limited RRR degradation, and good mechanical properties. If the cavity is found to exhibit improved performance upon further processing, a more substantial statement on the TIG weld performance can be made. In terms of this application, since the cavity surpassed the goal performance metrics, the use of reactor grade and TIG welds can be deemed an overall success.

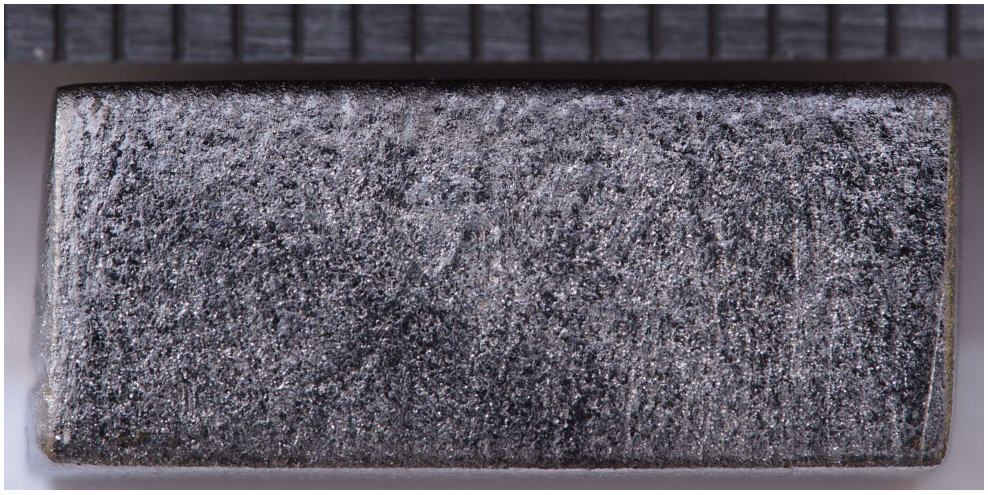

(a)

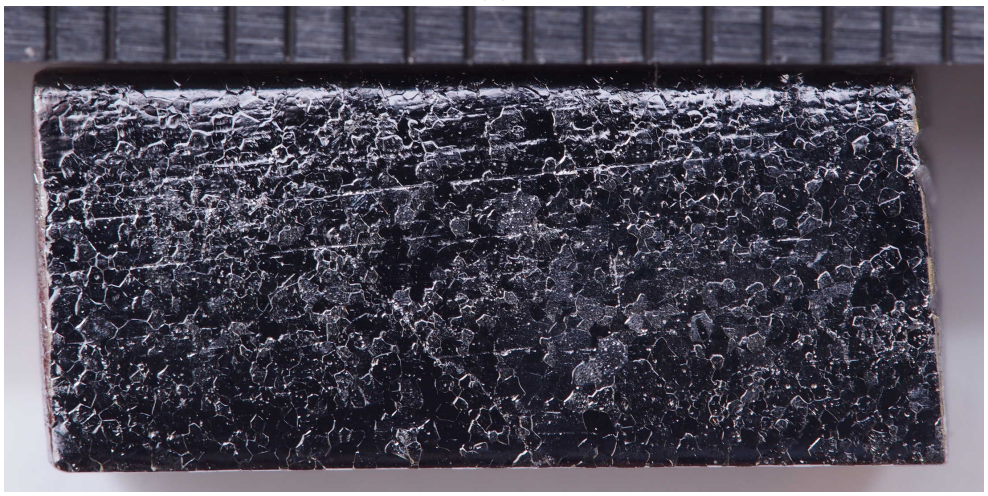

(b)

Figure 6.13: a) A sample of the cavity niobium, etched 100 µm by BCP. b) Another sample that was etched 100 µm, then baked at 1400°C for 5 hours, then etched another 100 µm. A scale with mm spacings is included for reference.

# Chapter 7

# Conclusions

The design and test results of a 650 MHz SRF deflecting mode cavity have been presented, which will be employed as an RF beam separator for the ARIEL e-Linac. An upgrade to the e-Linac will add a recirculation arc to the beam line, allowing the beam to make a second pass through the accelerator cavities and operate as an energy recovery linac. The SRF separator cavity will allow simultaneous beam delivery to both ARIEL and an advanced light source driven by a second beam by accelerating both beams concurrently and separating the interleaved beams as they exit the accelerating cavities.

The geometry of the separator cavity was achieved through the use of simulation tools used to analyze the RF performance of the cavity, optimizing for high shunt impedance with minimal longitudinal footprint. The cavity operates in a TE-like mode, with the deflecting voltage imparted mainly by an electric field between the ridges on either side of the beam axis. By employing a post and ridge type geometry, the cavity obtains 50% higher shunt impedance and 50% less relative length than comparable non-TM mode deflecting mode cavity geometries, at the cost of increased peak electric and magnetic fields.

In addition to its RF performance, the design of the cavity takes into account considerations for damping higher order modes, multipacting susceptibility, and how it will be fabricated. The HOM damping scheme suppresses the peak power dissipated from HOMs to less than 1 W and mitigates the risk of multipass beam breakup from destroying the beam quality. Simulations have shown that while multipacting is possible within the cavity, it is not expected to cause operational issues. The fabrication of the cavity with solid ridges provides the rigidity required to minimize frequency fluctuations in response to changes in helium bath pressure. Thermal simulations of

the temperature response of the cavity due to the thickness of the material on the ridges shows only minimal temperature rise of the inner RF surface at the operating field.

The resulting cavity design provides the required deflecting voltage within a compact structure with high shunt impedance and low RF power dissipation. The cavity will operate at 4.2 K, simplifying the cryomodule design and making use of the liquid helium services supplying the e-Linac accelerating cavities. Due to the low RF fields on the cavity walls, non-standard fabrication techniques were developed in the manufacturing of this cavity to keep costs low. This includes machining the parts from bulk reactor grade niobium and developing a method for applying TIG welding to the fabrication of SRF cavities.

TIG welding niobium requires welding inside of an inert environment, achieved through the use of a glove box purged with high purity argon gas. A method for achieving high quality welds with minimal degradation of $RRR$, and hence purity of the weld joint, was developed, requiring only standard, widely available fabrication equipment. This technology provides a low cost manufacturing option for SRF cavities with moderate operating requirements or for components of cavities that see relatively low power dissipation.

Cryogenic tests of the separator cavity quantified its performance at temperatures down to 2 K. At the operating temperature of 4.2 K, the cavity achieved a quality factor of $3.8 \times 10^8$ at the design deflecting voltage, representing a heat load of well below 1 W to the liquid helium cooling system. The cavity reached a maximum deflecting voltage of 0.82 MV at 4.2 K, with peak surface fields of 26 MV/m and 33 mT. Multipacting barriers were encountered as the cavity voltage was increased, but these were relatively easily processed and did not reoccur.

The cavity was determined to be insensitive to either a 120°C bake or Q disease. Its performance however was found to be limited by the poor surface roughness obtained after etching by BCP. Even so, the cavity surpassed the design goals laid out for its performance, reaching higher fields than required for beam separation in the e-Linac with a moderate quality factor, showing the successful application of alternative fabrication methods used in its construction.

Analysis of the RF surface after etching showed pitting along grain boundaries and a non-uniform grain structure. A possible explanation for this is insufficient processing of the niobium ingot during its production. Further surface treatments such as electropolishing or recrystallization is suggested to improve the surface roughness.

However, in its present form the cavity was found to exceed design specifications and requires no further processing.

For its installation on the e-Linac beamline, the cavity requires the development of a cryomodule to support its operation at 4.2 K. The conceptual design of ancillaries such as the tuner, liquid helium jacket, and the input and HOM couplers have been developed, but require finalization and integration into the full design of a cryomodule.

The SRF separator cavity will serve as a necessary component to the ERL upgrade of the ARIEL e-Linac. The cavity will allow the simultaneous acceleration of beams bound to either ARIEL to drive the production of RIBs, or to drive an FEL while operating as an ERL. Development of the cavity allowed for the study and proof of concept of TIG welding of an SRF cavity, making this the first SRF cavity to be fabricated at TRIUMF.

# Appendix A

# Higher Order Mode Field Profiles

The on-axis electric field profiles of the SRF separator cavity were measured using the bead pull technique for almost every mode with frequency below 3 GHz. Capturing these modes required changing the location of the input and pick up antennas between the input coupler, HOM, and pick up ports to best couple to each mode.

The following pages list the measured frequencies and show the field profiles for all the modes measured, comparing them to the simulated field profiles from the HFSS simulation. Of particular interest are the modes with highest shunt impedance that pose the highest risk of causing multipass beam break up or high power dissipation. These modes, such as the traverse deflecting mode at 1210 MHz and longitudinal modes at 940 MHz and 2730 MHz all show good agreement to the simulated modes. The accuracy of the electromagnetic model provides confidence in the proposed HOM damping scheme.

Several of the simulated modes were seen on the network analyzer but were not able to have their field profiles measured with the available coupling locations as they did not provide an adequate signal. Another mode with frequency of 2880 MHz modelled in the electromagnetic model was not seen in the cavity due to its very low electric field magnitude at all possible antenna locations. These modes are plotted, but without bead pull data overlaid. Two modes, at 2424 MHz and 2524 MHz were measured in the cavity, but no corresponding mode in the HFSS simulation was found.

Of the remaining modes, only a few show deviations from the simulated profiles, mostly in the higher frequency modes that have smaller wavelength and are therefore more susceptible to the alignment of the bead, simulation errors, or geometrical differences in the fabricated cavity. In some cases, the field profile was seen to be distorted by the presence of the bead, particularly if another mode was close by.

Table A.1: Measured and simulated frequencies of HOMs and their polarization.

| HOM | Polarization | Measured Frequency [MHz] | Simulated Frequency [MHz] | $\Delta f$ [%] |
|---|---|---|---|---|
| 1 | z | 939.7 | 935.9 | 0.4 |
| 2 | z | 1013.5 | 1008.3 | 0.5 |
| 3 | x | 1208.4 | 1200.8 | 0.6 |
| 4 | y | 1370.2 | 1374.0 | 0.3 |
| 5 | x | 1593.5 | 1588.3 | 0.3 |
| 6 | z | 1591.4 | 1589.8 | 0.1 |
| 7 | y | 1682.2 | 1684.5 | 0.1 |
| 8 | x | 1771.1 | 1771.7 | 0.03 |
| 9 | x | 1835.3 | 1836.3 | 0.1 |
| 10 | y | 1922.0 | 1916.5 | 0.3 |
| 11 | z | 2106.2 | 2104.1 | 0.1 |
| 12 | y | 2123.7 | 2120.4 | 0.2 |
| 13 | y | 2123.7 | 2125.1 | 0.1 |
| 14 | y | | 2143.6 | |
| 15 | z | 2226.8 | 2228.3 | 0.1 |
| 16 | x | 2242.9 | 2244.8 | 0.1 |
| 17 | x | | 2344.4 | |
| 18 | z | 2350.7 | 2350.4 | 0.01 |
| 19 | y | 2414.5 | 2407.4 | 0.3 |
| 20 | | 2423.6 | | |
| 21 | y | 2423.6 | 2430.7 | 0.3 |
| 22 | y | 2523.6 | 2519.3 | 0.2 |
| 23 | | 2523.6 | | |
| 24 | x | 2537.0 | 2537.4 | 0.02 |
| 25 | z | 2549.9 | 2555.8 | 0.2 |
| 26 | y | 2567.7 | 2566.6 | 0.04 |
| 27 | x | 2588.6 | 2589.6 | 0.04 |
| 28 | x | 2663.9 | 2654.6 | 0.4 |
| 29 | y | 2673.9 | 2672.5 | 0.02 |
| 30 | z | 2718.5 | 2721.6 | 0.1 |
| 31 | z | 2731.9 | 2725.1 | 0.2 |
| 32 | z | 2731.9 | 2723.5 | 0.3 |
| 33 | z | 2763.5 | 2766.4 | 0.1 |
| 34 | z | 2875.8 | 2874.2 | 0.1 |
| 35 | y | | 2880.5 | |
| 36 | y | 2889.0 | 2892.0 | 0.1 |
| 37 | x | 2903.4 | 2903.2 | 0.007 |
| 38 | x | 2907.6 | 2905.3 | 0.1 |
| 39 | z | 2906.7 | 2910.1 | 0.1 |
| 40 | x | 2943.4 | 2947.4 | 0.1 |

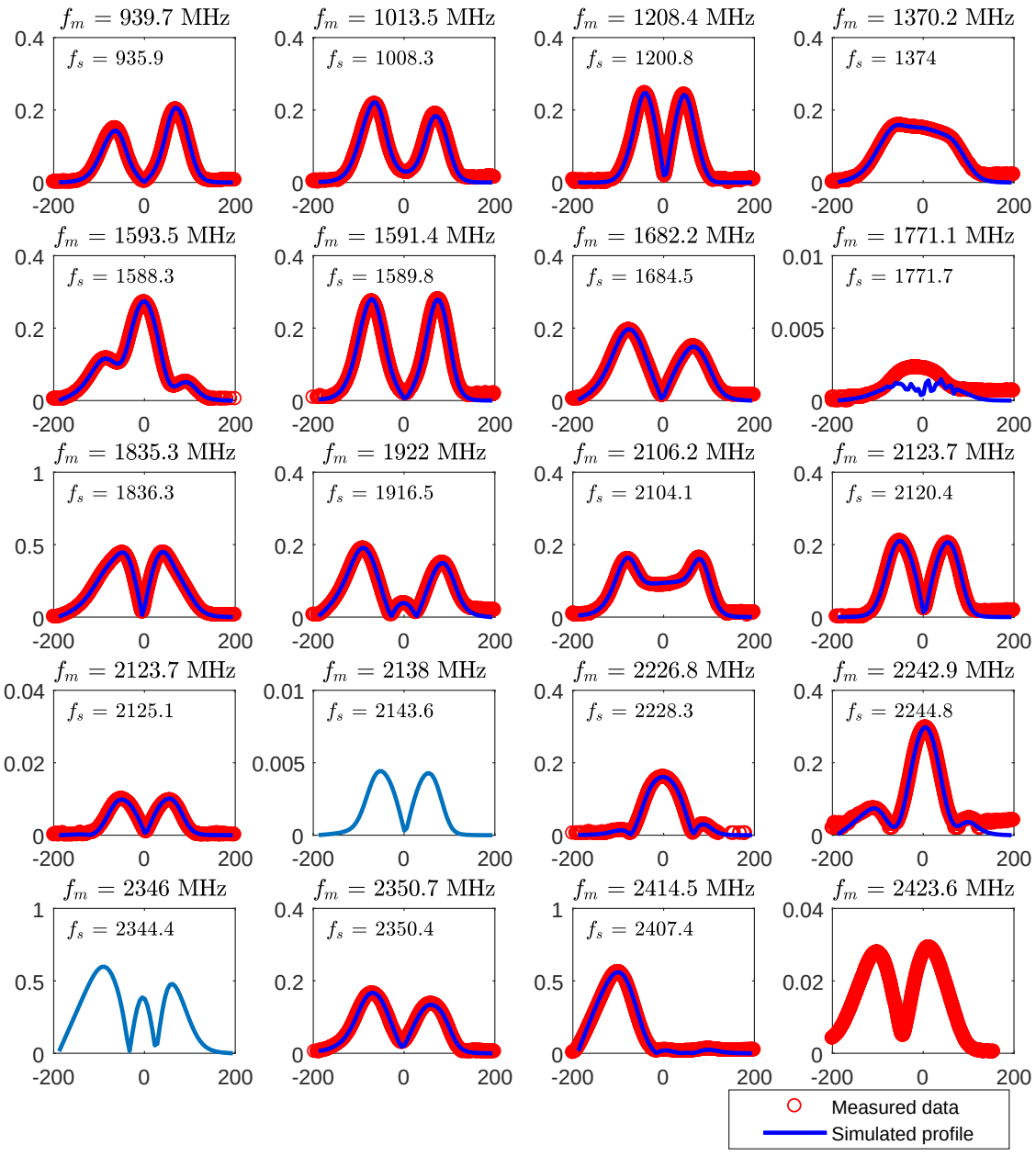


Figure A.1: The field profiles of the HOMs up to 2.4 GHz. The measured frequency, $f_m$ is printed above each plot and the simulated frequency, $f_s$, within the plot. The horizontal axis indicates the bead location in mm.

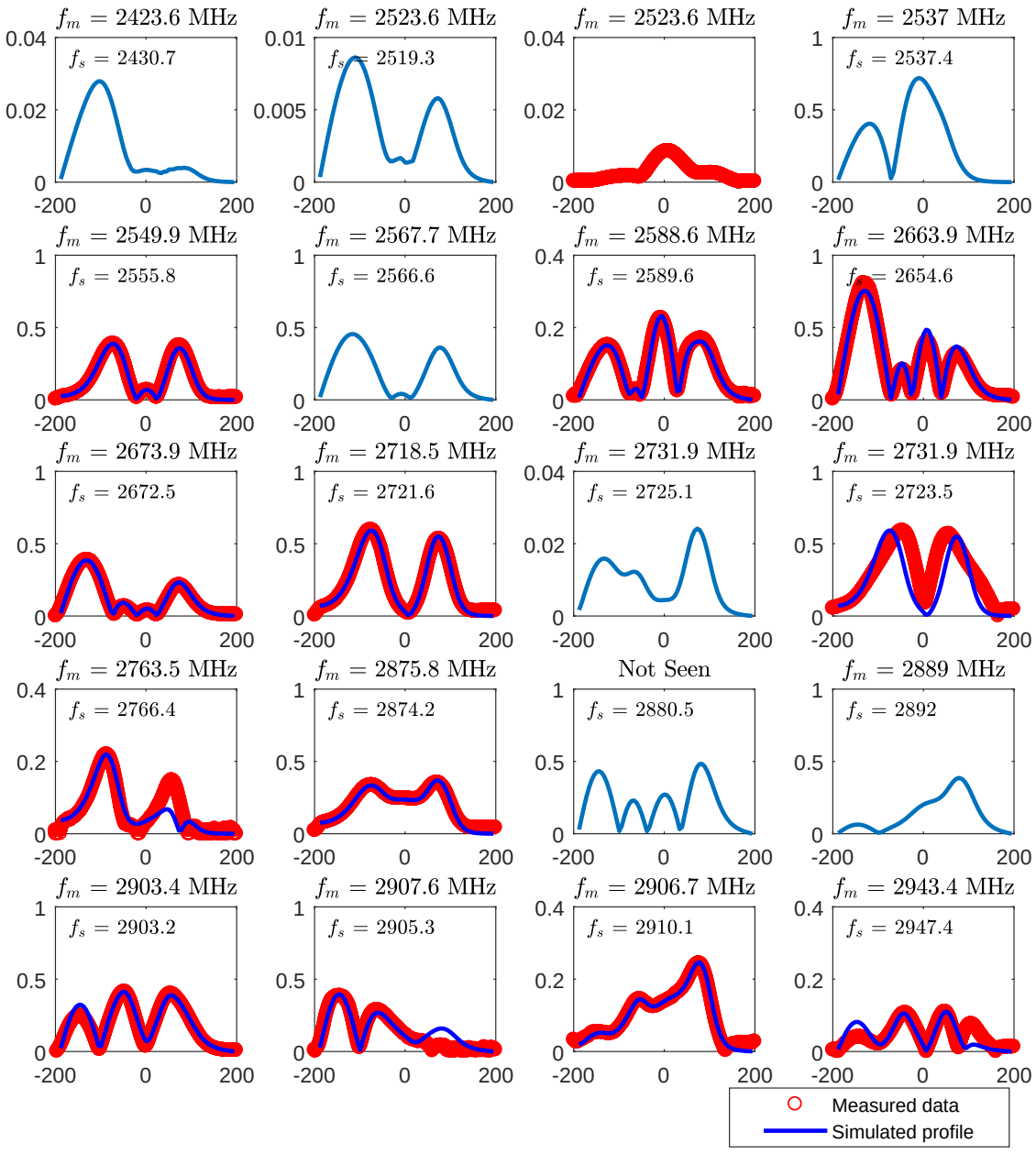


Figure A.2: The field profiles of the remaining HOMs up to 3 GHz. The measured frequency, $f_m$ is printed above each plot and the simulated frequency, $f_s$, within the plot. The horizontal axis indicates the bead location in mm.

# Bibliography

[1] C. Leemann and G. Yao. A highly effective deflecting structure. In *Proceedings of 1990 Linear Accelerator Conference, Albuquerque, New Mexico*, MO465, 1990.

[2] P. Baudrenghien, K. Brodzinski, R. Calaga, O. Capatina, E. Jensen, A. Macpherson, E. Montesinos, and V. Parma. Functional Specifications of the LHC Prototype Crab Cavity System, CERN-ACC-NOTE-2013-003, 2013.

[3] S.U. De Silva. *Investigation and optimization of a new compact superconducting cavity for deflecting and crabbing applications*. Ph.D. Dissertation, Old Dominion University, 2014.

[4] P. Bricault, M. Dombsky, A. Dowling, and M. Lane. High power target developments at ISAC. *Nuclear Instruments and Methods in Physics Research Section B: Beam Interactions with Materials and Atoms*, 204(C):319–324, 2003.

[5] R.E. Laxdal, R.A. Baartman, P. Bricault, G. Dutto, R. Poirier, P. Schmor, and G. Stanford. RNB post-accelerator for ISAC at TRIUMF – present and future. *Nuclear Physics A*, 701:647–650, April 2002.

[6] R.E. Laxdal. Commissioning and Early Experiments with ISAC-II. In *Particle accelerator. Proceedings, 22nd Conference, PAC'07, Albuquerque, USA*, THXAB01, 2007.

[7] J. Dilling, R. Krücken, and L. Merminga, editors. *ISAC and ARIEL: The TRIUMF radioactive beam facilities and the scientific program*. Springer, 2014.

[8] W.T. Diamond. A radioactive ion beam facility using photofission. *Nuclear Instruments and Methods in Physics Research Section A: Accelerators, Spectrometers, Detectors and Associated Equipment*, 432(2):471–482, 1999.

[9] L. Merminga, F. Ames, R. Baartman, P. Bricault, Y. Bylinski, Y-C. Chao, R. Dawson, D. Kaltchev, S. Koscielniak, R. Laxdal, F. Mammarella, M. Marchetto, G. Minor, A. Mitra, Y.-N. Rao, M. Trinczek, A. Trudel, V. Verzilov, and V. Zvyagintsev. ARIEL: TRIUMFs Advanced Rare IsotopE Laboratory. In *Proceedings of IPAC2011, San Sebastin, Spain*, WEOBA01, 2011.

[10] J. Sekutowicz. TESLA superconducting accelerating structures. *Measurement Science and Technology*, 18(8):2285, 2007.

[11] P. Kolb. *The TRIUMF nine-cell SRF cavity for ARIEL*. Ph.D. Dissertation, University of British Columbia, 2016.

[12] R.E. Laxdal and V. Zvyagintsev. ARIEL e-LINAC: Commissioning and Development. *Journal of Physics: Conference Series*, 747:012089, 2016.

[13] Y. Chao, C. Gong, and S.R. Koscielniak. RF separator and septum layout concepts for simultaneous beams to RIB and FEL users at ARIEL. In *Proceedings of IPAC2011, San Sebastian, Spain*, WEPC002, 2011.

[14] Y. Chao. Private communication, 2013.

[15] P. Piot, C.L. Bohn, D.R. Douglas, G.A. Krafft, R. Li, and B.C. Yunn. Emittance and Energy Spread Studies in the Jefferson Lab Free-electron Laser. In *Proceedings of EPAC2000, Vienna, Austria*, MOP4B14, 2000.

[16] G.R. Neil, C.L. Bohn, S.V. Benson, G. Biallas, D. Douglas, H.F. Dylla, R. Evans, J. Fugitt, A. Grippo, J. Gubeli, R. Hill, K. Jordan, R. Li, L. Merminga, P. Piot, J. Preble, M. Shinn, T. Siggins, R. Walker, and B. Yunn. Sustained Kilowatt Lasing in a Free-Electron Laser with Same-Cell Energy Recovery. *Phys. Rev. Lett.*, 84:662–665, 2000.

[17] HFSS, ANSYS Inc., Canonsburg, PA, USA.

[18] ACE3P, SLAC Advanced Computations Department, Menlo Park, CA, USA.

[19] Ansys-APDL, ANSYS Inc., Canonsburg, PA, USA.

[20] R.E. Laxdal. Acceleration of radioactive ions. *Nuclear Instruments and Methods in Physics Research Section B: Beam Interactions with Materials and Atoms*, 204(C):400–409, 2003.

[21] D.H. Whittum and Y. Kolomensky. Analysis of an asymmetric resonant cavity as a beam monitor. *Review of Scientific Instruments*, 70(5):2300–2313, 1999.

[22] I. Ben-Zvi. Superconducting storage cavity for RHIC, Brookhaven National Laboratory Internal Report, BNL-81965-2009-IR, 2009.

[23] H.A. Schwettman, P.B. Wilson, J.P. Pierce, and W.M. Fairbank. The application of superconductivity to electron linear accelerators. *Advances in Cryogenic Engineering*, 10:88–92, 1965.

[24] S. Posen and D.L. Hall. $Nb_3Sn$ superconducting radiofrequency cavities: fabrication, results, properties, and prospects. *Superconductor Science and Technology*, 30(3):033004, 2017.

[25] E.W. Collings, M.D. Sumption, and T. Tajima. Magnesium diboride superconducting RF resonant cavities for high energy particle acceleration. *Superconductor Science and Technology*, 17(9):S595, 2004.

[26] A. Gurevich. Enhancement of RF breakdown field of superconductors by multilayer coating. *Applied Physics Letters*, 88(1):012511, 2006.

[27] A. Grassellino, A. Romanenko, D. Sergatskov, O. Melnychuk, Y. Trenikhina, A. Crawford, A. Rowe, M. Wong, T. Khabiboulline, and F. Barkov. Nitrogen and argon doping of niobium for superconducting radio frequency cavities: a pathway to highly efficient accelerating structures. *Superconductor Science and Technology*, 26(10):102001, 2013.

[28] W.K.H. Panofsky and W.A. Wenzel. Some Considerations Concerning the Transverse Deflection of Charged Particles in Radio-Frequency Fields. *Review of Scientific Instruments*, 27(11):967–967, 1956.

[29] H.K. Onnes. The resistance of pure mercury at helium temperatures. *Communications from the Laboratory of Physics at the University of Leiden*, 12, 1911.

[30] A.P. Drozdov, M.I. Eremets, I.A. Troyan, V. Ksenofontov, and S.I. Shylin. Conventional superconductivity at 203 kelvin at high pressures in the sulfur hydride system. *Nature*, 525:73, 2015.

[31] J. Bardeen, L.N. Cooper, and J.R. Schrieffer. Microscopic Theory of Superconductivity. *Physical Review*, 106:162–164, 1957.

[32] D.C. Mattis and J. Bardeen. Theory of the Anomalous Skin Effect in Normal and Superconducting Metals. *Physical Review*, 111:412–417, 1958.

[33] J. Halbritter. Comparison between measured and calculated RF losses in the superconducting state. *Zeitschrift fur Physik*, 238:466–476, 1970.

[34] H. Padamsee, J. Knobloch, and T. Hays. *RF superconductivity for accelerators*. Wiley-VCH, 2008.

[35] H. Swan. Cornell SRIMP code. `https://www.classe.cornell.edu/~liepe/webpage/researchsrimp.html`. Accessed 2017.

[36] K.K. Schulze. Preparation and characterization of ultra-high-purity niobium. *Journal of Metals*, 33:33–41S, 1981.

[37] ASTM Standard B393. Standard Specification for Niobium and Niobium Alloy Strip, Sheet, and Plate, ASTM International, West Conshohocken, PA, 2009.

[38] C. Benvenuti, N. Circelli, and M. Hauer. Niobium films for superconducting accelerating cavities. *Applied Physics Letters*, 45(5):583–584, 1984.

[39] T.P. Wangler. *RF Linear Accelerators*. Wiley-VCH Verlag GmbH & Co. KGaA, 2010.

[40] P.R. Phillips. Microwave separator for high energy particle beams. *Review of Scientific Instruments*, 32(1):13–16, 1961.

[41] M. Bell, P. Bramham, R.D. Fortune, E. Keil, and B.W. Montague. RF Particle Separators. In *Proceedings of the International Conference on High Energy Accelerators, Dubna*, page 1038, 1963.

[42] G.A. Loew and O. H. Altenmueller. Design and applications of RF separator structures at SLAC. In *Proceedings of the International Conference on High Energy Accelerators, Frascati, Italy*, pages 551–5, 1965.

[43] H. Hahn and H.J. Halama. Design of the deflector for the RF beam separator at the Brookhaven AGS. *Review of Scientific Instruments*, 36(12):1788–1796, 1965.

[44] A. Citron, G. Dammertz, M. Grundner, L. Husson, R. Lehm, and H. Lengeler. The Karlsruhe - CERN superconducting RF separator. *Nuclear Instruments and Methods*, 164(1):31–55, 1979.

[45] P. Krejcik, E. Bong, M. Boyes, S. Condamoor, J.P. Eichner, G. Gassner, A. Haase, B. Hong, B. Morris, J. Olsen, D. Sprehn, and J. Wang. Engineering design of the new LCLS X-band transverse deflecting cavity. In *Proceedings of IBIC2013, Oxford, UK*, MOPC41, 2013.

[46] K. Hosoyama, S. Mitsunobu, and T. Furuya. Design and performance of KEKB superconducting cavities and its cryogenic system. *Advances in Cryogenic Engineering*, 43:123–130.

[47] K. Hosoyama, K. Hara, A. Honma, A. Kabe, Y. Kojima, Y. Morita, H. Nakai, K. Nakanishi, K. Akai, K. Ebihara, T. Furuya, S. Mitsunobu, M. Ono, Y. Yamamoto, K. Okubo, K. Sennyu, H. Hara, and T. Yanagisawa. Development of the KEK-B superconducting crab cavity. In *Proceedings of EPAC08, Genoa, Italy*, THXM02, 2008.

[48] C. Hovater, G. Arnold, J. Fugitt, L. Harwood, R. Kazimia, G. Lahti, J. Mammosser, R. Nelson, C. Piller, and L. Turlington. The CEBAF RF separator system. In *Proceedings of 1996 Linear Accelerator Conference, Geneva, Switzerland*, MOP12, 1996.

[49] S. Belomestnykh, I. Bazarov, V. Shemelin, J. Sikora, K. Smolenski, and V. Veshcherevich. Deflecting cavity for beam diagnostics at Cornell ERL injector. *Nuclear Instruments and Methods in Physics Research Section A: Accelerators, Spectrometers, Detectors and Associated Equipment*, 614(2):179–183, 2010.

[50] A. Vrielink, Y.C. Chao, C. Gong, R.E. Laxdal, and V. Zvyagintsev. Longitudinal emittance measurement system for the ARIEL electron linac. In *Proceedings of NAPAC2013, Pasadena, CA, USA*, THPAC01, 2013.

[51] L. Rossi and O. Brüning. High Luminosity Large Hardon Collider - A description for the European Strategy Preparatory Group, CERN-ATS-2012-236, 2012.

[52] S.U. De Silva and J.R. Delayen. Cryogenic test of a proof-of-principle superconducting rf-dipole deflecting and crabbing cavity. *Physical Review Special Topics – Accelerators and Beams*, 16:082001, 2013.

[53] B. Xiao, L. Alberty, S. Belomestnykh, I. Ben-Zvi, R. Calaga, C. Cullen, O. Capatina, L. Hammons, Z. Li, C. Marques, J. Skaritka, S. Verdú-André, and Q. Wu. Design, prototyping, and testing of a compact superconducting double quarter

wave crab cavity. *Physical Review Special Topics – Accelerators and Beams*, 18:041004, 2015.

[54] B. Hall, G. Burt, R. Apsimon, C.J. Lingwood, A. Tutte, A. Grudiev, A. Macpherson, M. Navarro-Tapia, R. Calaga, K.G. Hernández-Chahín, R.B. Appleby, and P. Goudket. Design and testing of a four rod crab cavity for High Luminosity LHC. *Physical Review Accelerators and Beams*, 20:012001, 2017.

[55] S.U. De Silva and J.R. Delayen. Design evolution and properties of superconducting parallel-bar RF-dipole deflecting and crabbing cavities. *Physical Review Special Topics – Accelerators and Beams*, 16:012004, 2013.

[56] B. Hall. *Designing the Four Rod Crab Cavity for the High-Luminosity LHC upgrade*. Ph.d. dissertation, cockcroft institute uk, 2014.

[57] S.U. De Silva, H. Park, J.R. Delayen, Z. Li, and T.H. Nicol. Design and prototyping of a 400 MHz RF-Dipole crabbing cavity for the LHC high-luminosity upgrade. In *Proceedings of IPAC2015, Richmond, VA, USA*, WEPWI036, 2015.

[58] S. Verdú-André, J. Skaritka, Q. Wu, B.P. Xiao, S. Belomestnykh, I. Ben-Zvi, L. Alberty, K. Artoos, R. Calaga, O. Capatina, T. Capelli, F. Carra, R. Leuxe, N. Kuder, C. Zanoni, and Z. Li. Design and prototyping of HL-LHC double quarter wave crab cavities for SPS test. In *Proceedings of IPAC2015, Richmond, VA, USA*, MOBD2, 2015.

[59] M. McAshan and M. Tigner. *Practical Heat Transfer and Fluid Flow*. World Scientific, 1st edition, 1999.

[60] National Energy Research Scientific Computing Center. A DOE Office of Science User Facility supported by the Office of Science of the U.S. Department of Energy under Contract No. DE-AC02-05CH11231.

[61] S.U. De Silva, J.R. Delayen, R.G. Olave, L. Doolittle, M. Placidi, A. Ratti, and P. Emma. A compact beam spreader using RF deflecting cavities for the LCLS-II. In *Proceedings of IPAC2014, Dresden, Germany*, WEPRI075, 2014.

[62] U. Ratzinger. H-Type linac structures. In *CERN Accelerator School Course on RF Engineering, Seeheim, Germany*, pages 351–380, 2000.

[63] General Particle Tracer for Windows, Pulsar Physics, Eindhoven, Netherlands.

[64] V. Shemelin and S. Belomestnykh. Using a resistive material for HOM damping. In *Proceedings of the IPAC'10*, WEPEC063, 2010.

[65] P. Kolb, R.E. Laxdal, V. Zvyagintsev, Y.C. Chao, and B. Amini. Cold tests of HOM absorber material for the ARIEL eLINAC at TRIUMF. *Nuclear Instruments and Methods in Physics Research Section A: Accelerators, Spectrometers, Detectors and Associated Equipment*, 734:60–64, 2014.

[66] F. Gerigk. *Design of Higher-Order Mode Dampers for the 400 MHz LHC Superconducting Cavities*. Ph.D. Dissertation, Technishe Universität Berlin, 1997.

[67] W. Xu, I. Ben-Zvi, S. Belomestnykh, H. Hahn, and E.C. Johnson. New HOM coupler design for high current SRF cavity. In *Proceedings of the 2011 Particle Accelerator Conference, New York, NY, USA*, TUP060, 2011.

[68] LTspice, Linear Technology, Milpitas, CA, USA.

[69] L. Ge, C. Adolphsen, L.K. Ko, Z.L. Lee, C. Ng, G. Schussman, F. Wang, and B. Rusnak. Multipacting simulations of TTF-III power coupler components. In *Proceedings of PAC07, Albuquerque, New Mexico, USA*, WEPMS041, 2007.

[70] A. Castilla. *Crabbing system for an electron-ion collider*. Ph.D. Dissertation, Old Dominion University, 2017.

[71] R.E. Laxdal. Initial commissioning results from the ISAC-II SC linac. In *Proceedings of LINAC 2006, Knoxville, Tennessee USA*, TH1003, 2006.

[72] G. Myneni and H. Umezawa. Variation of mechanical properties of high RRR and reactor grade niobium with heat treatments. *Matériaux & Techniques*, 91(7-8-9):19–22, 2003.

[73] V. Nguyen, J.R. Delayen, L. Doolittle, E. Feldl, and W. Sachleben. Frequency tuning of the CEBAF upgrade cavities. In *Proceedings of the 1999 Particle Accelerator Conference, New York USA*, pages 928–930, 1999.

[74] C.A. Cooper, A. Wu, P. Bauer, and C. Antoine. Effect of different cutting techniques on the surface morphology and composition of niobium. *IEEE Transactions on Applied Superconductivity*, 19(3):1399–1403, 2009.

[75] G. Ciovati, P. Dhakal, and G.R. Myneni. Superconducting radio-frequency cavities made from medium and low-purity niobium ingots. *Superconductor Science and Technology*, 29(064002), 2016.

[76] T. Goodsell. Private communication, 2018.

[77] C. Compton, D. Baars, T. Bieler, J. Bierwagen, S. Bricker, W. Hartung, D. Pendell, R. York, L. Cooley, H. Jiang, and B. Kephart. Studies of alternative techniques for niobium cavity fabrication. In *Proceedings of SRF2007, Peking University, Beijing, China*, WEP01, 2007.

[78] W. Singer, X. Singer, J. Tiessen, H. M. Wen, and F. Schölz. RRR degradation and gas absorption in the electron beam welding area of high purity niobium. *AIP Conference Proceedings*, 671(1):162–175, 2003.

[79] GE Infrastructure Sensing. *Model O2X1 Oxygen Transmitter User's Manual*, 2004.

[80] W. Singer, A. Ermakov, and X. Singer. RRR-measurement techniques on high purity niobium, TTC-Report 2010-02, DESY, 2010.

[81] D. Proch, B. Dwersteg, G. Kreps, A. Matheisen, W.-D. Möller, D. Renken, J. Sekutowicz, and W. Singer. Laboratory Report, DESY. In *Proceedings of the Sixth Workshop on RF Superconductivity, CEBAF, Newport News, Virginia, USA*, SRF93A08, 1993.

[82] T. Jones, S. Pattalwar, G. Burt, J. Mitchell, L. Marques Antunes Ferreira, R. Calaga, O. Capatina, R. Leuxe, S. Verdú-André, and B. Xiao. Determining BCP etch rate and uniformity in high luminosity LHC crab cavities. In *Proceedings of SRF2017, Lanzhou, China*, TUPB100, 2017.

[83] D. Longuevergne, C. Beard, P. Kolb, R.E. Laxdal, A. Grassellino, and V. Zvyagintsev. RF cavity performance in the ISAC-II superconducting heavy ion linac. In *Proceedings of Linear Accelerator Conference LINAC2010, Tsukuba, Japan*, THP044, 2010.

[84] B. Bonin and R.W. Röth. Q degradation of niobium cavities due to hydrogen contamination. In *Fifth Workshop on RF Superconductivity, DESY, Hamburg, Germany*, SRF91D01, 1991.

[85] J.C. Simons and J.C. Slater. Electromagnetic resonant behavior of a confocal spheroidal cavity system in the microwave region. *Journal of Applied Physics*, 23(1):29–30, 1952.

[86] J.R. Delayen. *Phase and amplitude stabilization of superconducting resonators*. PhD Dissertation, California Institute of Technology, 1978.

[87] J. Knobloch, R.L. Geng, M. Liepe, and H. Padamsee. High-field Q-slope in superconducting cavities due to magnetic field enhancement at grain boundaries. In *Proceedings of 9th Workshop on RF Superconductivity, Santa Fe, USA*, 1999.

[88] G. Ciovati. Improved oxygen diffusion model to explain the effect of low-temperature baking on high field losses in niobium superconducting cavities. *Applied Physics Letters*, 89:022507, 2006.

[89] G. Ciovati. Effect of low-temperature baking on the radio-frequency properties of niobium superconducting cavities for particle accelerators. *Journal of Applied Physics*, 96(3):1591–1600, 2004.

[90] K. Saito and P. Kneisel. Q degradation in high purity niobium cavities: Dependence on temperature and RRR value. In *Proceedings of the 3rd European Particle Accelerator Conference, Berlin, Germany*, pages 1231–1233, 1992.